DESIGN OF A DECOUPLING NETWORK TO IMPROVE ISOLATION BETWEEN TWO PORTS OF MULTI-FUNCTIONAL ANTENNA

A THESIS SUBMITTED TO
THE GRADUATE SCHOOL OF NATURAL AND APPLIED SCIENCES
OF
MIDDLE EAST TECHNICAL UNIVERSITY

BY

MUHAMMED TONGA

IN PARTIAL FULFILLMENT OF THE REQUIREMENTS
FOR
THE DEGREE OF MASTER OF SCIENCE
IN
ELECTRICAL AND ELECTRONIC ENGINEERING

JUNE 2022

Approval of the thesis:

DESIGN OF A DECOUPLING NETWORK TO IMPROVE ISOLATION BETWEEN TWO PORTS OF MULTI-FUNCTIONAL ANTENNA

submitted by **Muhammed Tonga** in partial fulfillment of the requirements for the degree of **Master of Science** i**n Electrical and Electronic Engineering, Middle East Technical University** by,

Prof. Dr. Halil Kalıpçılar
Dean, Graduate School of **Natural and Applied Sciences** _____

Prof. Dr. İlkay Ulusoy
Head of the Department, **Electrical and Electronic Engineering** _____

Prof. Dr. Özlem Aydın Çivi
Supervisor, **Electrical and Electronic Engineering, METU** _____

Assoc. Prof. Dr. Lale Alatan
Co-Supervisor, **Electrical and Electronic Engineering, METU** _____

Examining Committee Members:

Prof. Dr. Sencer Koç
Electrical and Electronic Engineering, METU _____

Prof. Dr. Özlem Aydın Çivi
Electrical and Electronic Engineering, METU _____

Assoc. Prof. Dr. Lale Alatan
Electrical and Electronic Engineering, METU _____

Assist. Prof. Dr. Ahmet Cemal Durgun
Electrical and Electronic Engineering, METU _____

Prof. Dr. Birsen Saka
Electrical and Electronic Engineering, Hacettepe University _____

Date: 23.06.2022

I hereby declare that all information in this document has been obtained and presented in accordance with academic rules and ethical conduct. I also declare that, as required by these rules and conduct, I have fully cited and referenced all material and results that are not original to this work.

Name, Last Name: Muhammed Tonga

Signature:

ABSTRACT

DESIGN OF A DECOUPLING NETWORK TO IMPROVE ISOLATION BETWEEN TWO PORTS OF MULTI-FUNCTIONAL ANTENNA

Tonga, Muhammed
Master of Science, Electrical and Electronic Engineering
Supervisor: Prof. Dr. Özlem Aydın Çivi
Co-Supervisor: Assoc. Prof. Dr. Lale Alatan

June 2022, 101 pages

A multi-functional antenna considered in this thesis has different pattern shapes and ability to steer the beam by changing phase difference between its two ports. Coupling between these two ports is high, since two ports are excited coherently to establish a single mode in the antenna for the corresponding phase difference. Therefore, the antenna suffers from low and even negative gain value because of the coupling. In this thesis, a decoupling network is designed and implemented to the antenna to improve isolation between the ports. Thus, the ports are decoupled, and gain values are increased. Decoupling network theory is studied in detail and the antenna is redesigned to be able to apply the theory to the antenna. Decoupling network involves a reactive element. Different designs with an inductor and a capacitor are performed and their performances are compared with both simulation and measurement results. It is shown that 2-3 dB improvement in the gain of the antenna can be achieved through the use of decoupling network.

Keywords: Decoupling Network, Multi-Functional Antenna, Isolation Improvement, Gain Enhancement

ÖZ

ÇOK FONKSİYONLU ANTENİN İKİ GİRİŞİ ARASINDAKİ YALITIMI İYİLEŞTİRMEK İÇİN AYRIKLAŞTIRMA DEVRESİ TASARIMI

Tonga, Muhammed
Yüksek Lisans, Elektrik ve Elektronik Mühendisliği
Tez Yöneticisi: Prof. Dr. Özlem Aydın Çivi
Ortak Tez Yöneticisi: Doç. Dr. Lale Alatan

Haziran 2022, 101 sayfa

Bu tezde ele alınan çok fonksiyonlu antenin iki girişi arasındaki faz farkı değiştirilerek farklı örüntü şekilleri elde edilebilmekte ve ışıma yönü değiştirilebilmektedir. İlgili faz farkına karşılık gelen modu oluşturabilmek için bu iki giriş uygun bir şekilde beslendiğinden, antenin bu iki girişi arasındaki bağlaşım yüksek olmaktadır. Bu bağlaşımdan dolayı antenin kazancı düşük, hatta negatif çıkmaktadır. Bu tezde girişler arasındaki yalıtımı iyileştirmek için bir ayrıklaştırma devresi tasarlanıp antene uygulanmıştır. Böylece girişler birbirinden ayrıştırılıp antenin kazancı yükseltilmiştir. Ayrıklaştırma devresi teorisi detaylı bir şekilde irdelenmiş ve bu teoriyi antene uygulayabilmek için anten yeniden tasarlanmıştır. Ayrıklaştırma devresi reaktif bir elemandan oluşmaktadır. Bobin ve sığaçla iki farklı tasarım yapılmış; bunların performansları hem benzetim hem de ölçüm sonuçlarıyla karşılaştırılmıştır. Ayrıklaştırma devresinin kullanımıyla, anten kazancında 2-3 dB'lik bir iyileştirmenin elde edilebildiği gösterilmiştir.

Anahtar Kelimeler: Ayrıklaştırma Devresi, Çok Fonksiyonlu Anten, Yalıtım İyileştirme, Kazanç Yükseltme

À ma femme

ACKNOWLEDGMENTS

First thanks go to the first place of my whole life: my love, my wife, Tonga the 2nd, Meryem; just because of being the most important and precious piece of my life and being with me in any case.

I'd like to thank Prof. Özlem Aydın Çivi and Assoc. Prof. Lale Alatan for their guidance, helps, supports, inspiring ideas throughout the whole study of this thesis.

After the professors, the first name to be written here is Feza Turgay Çelik by expressing my gratefulness to him. Thanks for the supports from the beginning of the study till the end.

I also thank Numan Akdemir and İlkay Karataş for their valuable contributions to make my design real.

I appreciate the financial support of TUBITAK as part of 2210-A program.

Honor guests: Zafer Tanç and Enis Kobal. Thank you so much for your sincere supports and brotherhood.

At least, I can honor your name here dad, Ali Tonga. I owe you who I am now. The most special gratitude goes to my mother, Hatice Tonga who is always with me. Also, not to miss my brothers, Murat and Eyyüp Tonga, thanks for everything.

We are all different people all through our lives and that's okay, that's good you've got to keep moving so long as you remember all the people that you used to be. I will not forget one line of this, not one day, I swear. I will always remember when The Doctor was me...

TABLE OF CONTENTS

ABSTRACT v

ÖZ vi

ACKNOWLEDGMENTS viii

TABLE OF CONTENTS ix

LIST OF TABLES xi

LIST OF FIGURES xii

LIST OF ABBREVIATIONS xvii

CHAPTERS

1 INTRODUCTION 1

1.1 Ringed Circular Patch Antenna 3

1.2 Isolation Techniques 6

1.3 Outline of the Thesis 11

2 APERTURE COUPLED MULTI-FUNCTIONAL ANTENNA DESIGN 13

2.1 Back Lobe Suppression 22

3 DECOUPLING NETWORK 27

3.1 Theory of Decoupling Network 28

3.2 Modified RCPA Design to Integrate Decoupling Network 33

3.3 Design of RCPA with Inductive Decoupling Network 41

3.4 Design of RCPA with Capacitive Decoupling Network 57

4 FABRICATION AND MEASUREMENTS OF RCPA WITH&WITHOUT DECOUPLING NETWORK 69
4.1 First Version RCPA 69
4.1.1 Fabrication 69
4.1.2 Measurement 72
4.2 Second Version RCPA 74
4.2.1 Redesign and Fabrication 74
4.2.2 Measurement Results 78
4.3 Implementation of Inductive Decoupling Network to RCPA 84
4.4 Implementation of Capacitive Decoupling Network to RCPA 89
5 CONCLUSION 95
REFERENCES 97
APPENDICES
A. S Parameters in Terms of Y Parameters 99
B. Derivation of Admittance Matrix of Two-Port Network with Purely Imaginary Component 100

LIST OF TABLES

TABLES

Table 2.1: Probe-fed RCPA Dimensions 15
Table 2.2: AC RCPA Optimized Antenna Parameters 18
Table 3.1: Simulated Gain and Realized Gain Values of RCPA without Decoupling Network 40
Table 3.2: Simulated Bandwidths of Matched and Decoupled (IND) RCPA 53
Table 3.3: Simulated Gain and Realized Gain Values of RCPA with Inductive Decoupling Network 54
Table 3.4: Simulated Bandwidths of Matched and Decoupled (CAP) RCPA..... 64
Table 3.5: Simulated Gain and Realized Gain Values of RCPA with Capacitive Decoupling Network 65
Table 4.1: Redesigned (Second Version) RCPA Antenna Parameters 77
Table 4.2: Simulated Realized Gain and Measured Gain of RCPA without Decoupling Network 83
Table 4.3: Bandwidths of RCPA with Inductor 85
Table 4.4: Gain Values of RCPA with&without Inductive Decoupling Network . 86
Table 4.5: Bandwidths of RCPA with Capacitor 90
Table 4.6: Gain Values of RCPA with&without Capacitive Decoupling Network 91

LIST OF FIGURES

FIGURES

Figure 1.1: Antennas and Through Air Communication 1
Figure 1.2: Beam Steering and Beam Forming 2
Figure 1.3: Ringed Circular Patch Antenna Illustration 4
Figure 1.4: Current Distributions for Both Phase Differences [2] 5
Figure 1.5: Surface Current Distributions. (a) without meander line, (b) with meander line [4] 7
Figure 1.6: Decoupling Line Technique [8] 9
Figure 1.7: Decoupling Network Technique [9] 10
Figure 2.1: Aperture Coupled RCPA Geometry 14
Figure 2.2: AC RCPA Slots and Feed Lines 14
Figure 2.3: $|S_{11}|$, Aperture Width Sweep 16
Figure 2.4: $|S_{11}|$, Aperture Length Sweep 16
Figure 2.5: $|S_{11}|$, Aperture Center Location Sweep 17
Figure 2.6: $|S_{11}|$, Length of Feed Line Stub Sweep 17
Figure 2.7: S Parameters of Optimized RCPA 19
Figure 2.8: AC RCPA Realized Gain Pattern, Conical Beam (PD: 0°) at $\phi = 90°$ Plane 19
Figure 2.9: AC RCPA Realized Gain Pattern, Broadside Beam (PD: 180°) at $\phi = 90°$ Plane 20
Figure 2.10: Current Distribution with 0° Phase Difference 21
Figure 2.11: Current Distribution with 180° Phase Difference 21
Figure 2.12: RCPA Structure with PEC Plate 22
Figure 2.13: S Parameters with&without PEC Plate 23
Figure 2.14: Normalized Radiation Patterns with&without PEC Plate, Conical Beam at $\phi = 90°$ Plane 24
Figure 2.15: Normalized Radiation Patterns with&without PEC Plate, Broadside Beam at $\phi = 90°$ Plane 24

Figure 3.1: Network Representation of Parallel Connected Antenna and Decoupling Network 28
Figure 3.2: Antenna Ports Connection to Decoupling Network Via Transmission Lines 31
Figure 3.3: Decoupled and Matched Antenna Scheme 32
Figure 3.4: Extension of Feed Lines 33
Figure 3.5: Appropriate Configuration of Feed Lines for Decoupling Network 34
Figure 3.6: Modified AC RCPA Geometry 35
Figure 3.7: RCPA without Decoupling Network S Parameters 36
Figure 3.8: RCPA without Decoupling Network Radiation Patterns, Conical Beam (PD: 0°) at $\phi = 0°$ Plane 36
Figure 3.9: RCPA without Decoupling Network Radiation Patterns, Conical Beam (PD: 0°) $\phi = 90°$ Plane 37
Figure 3.10: RCPA without Decoupling Network Radiation Patterns, Broadside Beam (PD: 180°) at $\phi = 0°$ Plane 37
Figure 3.11: RCPA without Decoupling Network Radiation Patterns, Broadside Beam (PD: 180°) at $\phi = 90°$ Plane 38
Figure 3.12: RCPA without Decoupling Network Radiation Patterns, PD: 90° at $\phi = 90°$ Plane 38
Figure 3.13: RCPA without Decoupling Network Active S Parameters 40
Figure 3.14: Circuit Diagram of RCPA Y Parameters with Transmission Lines 41
Figure 3.15: Y_{21}^{A} at the Ports of RCPA without Decoupling Network 42
Figure 3.16: Y_{21}^{A}, 57 mm away from Ports of RCPA without Decoupling Network 43
Figure 3.17: Admittance Network of a Purely Imaginary Lumped Element 44
Figure 3.18: Circuit Diagram of RCPA with Inductive Decoupling Network 45
Figure 3.19: Comparison of Imaginary Parts of Y_{21} with Inductance 46
Figure 3.20: Comparison of Real Parts of Y_{21} with Inductance 46
Figure 3.21: Simulated S Parameters of RCPA with 2.48 nH 47

Figure 3.22: HFSS Model of RCPA with Inductor 48
Figure 3.23: Simulated S Parameters of RCPA with 2.2 nH 49
Figure 3.24: $|S_{21}|$, Inductance Sweep 50
Figure 3.25: Circuit Diagram of Matched and Decoupled RCPA with 2.2 nH 51
Figure 3.26: HFSS Model of RCPA with Inductor and Stubs 51
Figure 3.27: Simulated S Parameters of Matched and Decoupled RCPA with 2.2 nH 52
Figure 3.28: $|S_{11}|$ of Inductive Decoupled RCPA Before Matching on Smith Chart 53
Figure 3.29: Matched and Inductive Decoupled RCPA Radiation Patterns, Conical Beam (PD: 0°) at $\phi = 0°$ Plane 54
Figure 3.30: Matched and Inductive Decoupled RCPA Radiation Patterns, Conical Beam (PD: 0°) at $\phi = 90°$ Plane 55
Figure 3.31: Matched and Inductive Decoupled RCPA Radiation Patterns, Broadside Beam (PD: 180°) at $\phi = 0°$ Plane 55
Figure 3.32: Matched and Inductive Decoupled RCPA Radiation Patterns, Broadside Beam (PD: 180°) at $\phi = 90°$ Plane 56
Figure 3.33: Simulated Active S Parameters of Matched and Inductive Decoupled RCPA 56
Figure 3.34: Y_{21}^{A}, 66 mm away from Ports of RCPA without Decoupling Network 57
Figure 3.35: Comparison of Imaginary Parts of Y_{21} with Capacitance 58
Figure 3.36: Comparison of Real Parts of Y_{21} with Capacitance 59
Figure 3.37: Simulated S Parameters of RCPA with 1 pF 59
Figure 3.38: $|S_{21}|$, Capacitance Sweep 60
Figure 3.39: Simulated S Parameters of RCPA with 0.8 pF in HFSS 61
Figure 3.40: HFSS Model of RCPA with Capacitor and Stubs 62
Figure 3.41: Simulated S Parameters of Matched and Decoupled RCPA with 0.8 pF 63

Figure 3.42: $|S_{11}|$ of Capacitive Decoupled RCPA Before Matching on Smith Chart 64
Figure 3.43: Matched and Capacitive Decoupled RCPA Radiation Patterns, Conical Beam (PD: 0°) at $\phi = 0°$ Plane 65
Figure 3.44: Matched and Capacitive Decoupled RCPA Radiation Patterns, Conical Beam (PD: 0°) at $\phi = 90°$ Plane 66
Figure 3.45: Matched and Capacitive Decoupled RCPA Radiation Patterns, Broadside Beam (PD: 180°) at $\phi = 0°$ Plane 66
Figure 3.46: Matched and Capacitive Decoupled RCPA Radiation Patterns, Broadside Beam (PD: 180°) at $\phi = 90°$ Plane 67
Figure 3.47: Simulated Active S Parameters of Matched and Capacitive Decoupled RCPA 67
Figure 4.1: Rear and Front Views of Fabricated Boards 70
Figure 4.2: Bonding Boards with Screws 71
Figure 4.3: Addition of PEC Plate to RCPA Boards 72
Figure 4.4: Measured S Parameters of First Version RCPA 73
Figure 4.5: $|S_{11}|$, Air Gap Sweep 74
Figure 4.6: $|S_{11}|$, Circular Patch Radius Sweep 75
Figure 4.7: $|S_{11}|$, Sweeps of Aperture Width (Ws) and Length of Feed Line Stub (Lf) 76
Figure 4.8: Simulated S Parameters of Second Version RCPA 77
Figure 4.9: Simulated Active S Parameters of Second Version RCPA 78
Figure 4.10: S Parameters of RCPA, Simulation Measurement Comparison 79
Figure 4.11: Anechoic Chamber Setup with RCPA 80
Figure 4.12: Power Divider and Coaxial Cables 80
Figure 4.13: Measured and Simulated Normalized Radiation Patterns of RCPA without DN, PD:0° at $\phi = 0°$ Plane 81
Figure 4.14: Measured and Simulated Normalized Radiation Patterns of RCPA without DN, PD:0° at $\phi = 90°$ Plane 82

Figure 4.15: Measured and Simulated Normalized Radiation Patterns of RCPA without DN, PD:180° at $\phi = 0°$ Plane 82
Figure 4.16: Measured and Simulated Normalized Radiation Patterns of RCPA without DN, PD:180° at $\phi = 90°$ Plane 83
Figure 4.17: Fabricated RCPA with Inductive Decoupling Network 84
Figure 4.18: S Parameters of RCPA with Inductive Decoupling Network, Simulation Measurement Comparison 85
Figure 4.19: Measured and Simulated Normalized Radiation Patterns of RCPA with Inductor, PD:0° at $\phi = 0°$ Plane 87
Figure 4.20: Measured and Simulated Normalized Radiation Patterns of RCPA with Inductor, PD:0° at $\phi = 90°$ Plane 87
Figure 4.21: Measured and Simulated Normalized Radiation Patterns of RCPA with Inductor, PD:180° at $\phi = 0°$ Plane 88
Figure 4.22: Measured and Simulated Normalized Radiation Patterns of RCPA with Inductor, PD:180° at $\phi = 90°$ Plane 88
Figure 4.23: Fabricated RCPA with Capacitive Decoupling Network 89
Figure 4.24: S Parameters of RCPA with Capacitive Decoupling Network, Simulation Measurement Comparison 90
Figure 4.25: Measured and Simulated Normalized Radiation Patterns of RCPA with Capacitor, PD:0° at $\phi = 0°$ Plane 92
Figure 4.26: Measured and Simulated Normalized Radiation Patterns of RCPA with Capacitor, PD:0° at $\phi = 90°$ Plane 92
Figure 4.27: Measured and Simulated Normalized Radiation Patterns of RCPA with Capacitor, PD:180° at $\phi = 0°$ Plane 93
Figure 4.28: Measured and Simulated Normalized Radiation Patterns of RCPA with Capacitor, PD:180° at $\phi = 90°$ Plane 93
Figure B: Two-Port Network Representation of a Purely Imaginary Element ….100

LIST OF ABBREVIATIONS

ABBREVIATIONS

CSM:	Cross Structure Metasurface
DN:	Decoupling Network
LTCC:	Low Temperature Cofired Ceramic
MIMO:	Multiple-Input Multiple-Output
PD:	Phase Difference
PEC:	Perfect Electric Conductor
RCPA:	Ringed Circular Patch Antenna
SCSRR:	Slotted-Complementary Split-Ring Resonator
SSM:	Strip Structure Metasurface

CHAPTER 1

INTRODUCTION

Antennas are the structures that can enable us to communicate without any direct connection between devices. It is done by capturing radio signals from air and conveying them to receivers or vice versa as depicted in Figure 1.1. Therefore, it can be thought as antennas are matching structures of radio signals between air and communication devices. Antennas make long distant communication easier because of not requiring direct cable connection between devices. It is also evident that antennas play a vital role in outer space communication and research.

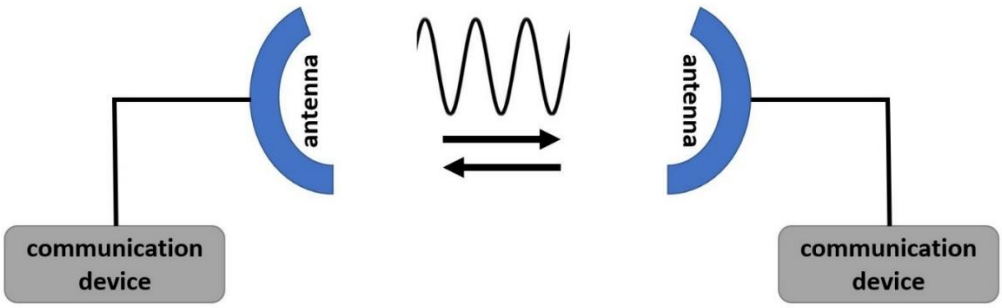

Figure 1.1: Antennas and Through Air Communication

Various types of antennas with different capabilities have been designed so far as explained in [1]. In this thesis, our study exploits a microstrip type antenna which has a metallic patch with a ground plane. Moreover, antennas are designed to serve different purposes. For instance, directive antennas are for higher gain required

systems and to focus the antenna beam to desired direction. Here, two features are related to our study: beam steering and pattern reconfigurability.

Beam steering and pattern reconfigurability of the antennas have been investigated and advanced over the years. Beam steering is changing the direction of the beam which enables switching users in different positions and pattern reconfigurability is forming the beam for different needs which provides adjusting the focus of the radiated signal. Beam steering and beam forming phenomena are roughly sketched in Figure 1.2. There are many different techniques to have beam steering and beam forming. For example, the most known one is by varying phases of antenna elements in an antenna array, overall beam can be steered to desired direction. In such arrays, it is important to steer the beam to cover desired angles with sufficient gain values. In particular, when beam is steered to wide scan angles, gain is reduced due to low radiation of element in these directions.

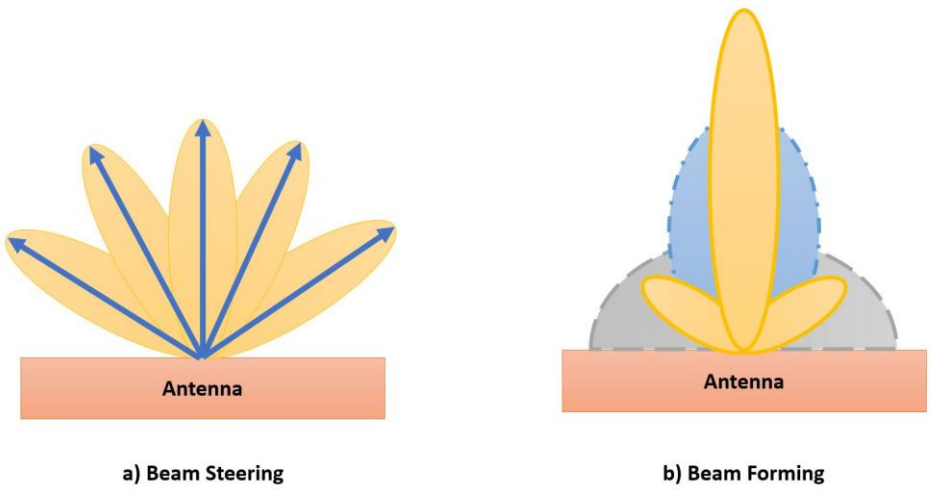

Figure 1.2: Beam Steering and Beam Forming

In the study of [2], ringed circular patch antenna is designed as a pattern reconfigurable antenna. This antenna is discussed in this thesis because of its unfavorable feature which is low gain. The gain of ringed circular patch antenna is

not only low as compared to common patch antennas but also has a negative value. The low gain arises from the coupling of the antenna ports as stated in [2]. That is explained in the next section in detail. The remarkable problem here is that RCPA (ringed circular patch antenna) ports are excited at the same time to construct a single mode in the antenna for the corresponding phase difference between the ports.

Our first aim is to increase realized gain of RCPA by eliminating the coupling of antenna ports. Thus, it can be said that the main goal in this thesis is providing isolation to the ports of the antenna.

1.1 Ringed Circular Patch Antenna

One of the pattern reconfigurable antennas discussed in [2] is ringed circular patch antenna which has a circular patch in the middle and a ring around the circular patch. The ring is separated from the circular patch by a distance as shown in Figure 1.3. The ring is fed by two probes symmetrically located in opposite sides of the circular patch and coupling between the ring and the circular patch excites the circular patch without any connection. Therefore, the gap between the ring and the circular patch is relatively narrow for a better coupling.

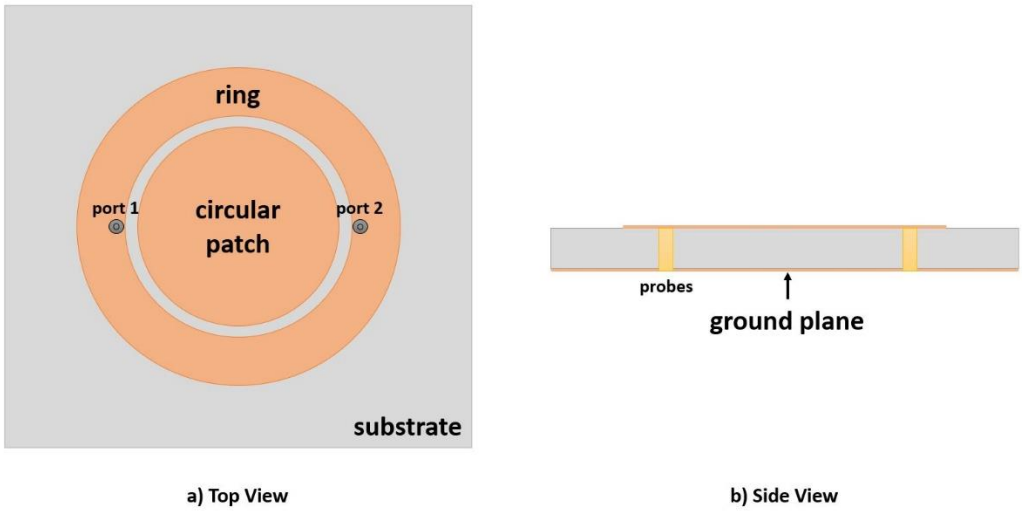

Figure 1.3: Ringed Circular Patch Antenna Illustration

RCPA can attain different patterns and beam directions with the excitation of different TM modes. For pattern diversity, it is needed to make modes of both the ring and the patch operate in same frequency band. Following modes are found to have conical beam by the ring and broadside beam by the patch around 3.6 GHz:

- TM_{11} mode for the circular patch
- TM_{21} mode for the ring

Antenna dimensions are determined by regarding the modes defined above operating at the same frequency. RCPA is also miniaturized in [2] but miniaturization is not in our scope. Hence, we stick to the original antenna dimensions.

Radiation mechanism of RCPA at 3.6 GHz is as follows:

- The ring creates conical beam with TM_{21} mode.
- When the phase difference between the ports is 0°, the ring radiates and creates conical beam.
- Conical beam has its peaks at $\theta = \pm 40°$.
- The circular patch creates broadside beam with TM_{11} mode.
- When the phase difference between the ports is 180°, the circular patch radiates and creates broadside beam.
- Broadside beam has its peak at $\theta = 0°$.

It is also possible to steer the beam to other angles and to have different patterns with applying various phase differences to the ports. It is ensured by exciting the ring and the patch with combination of TM_{11} and TM_{21} modes. For instance, by applying 90° phase difference, the beam is directed to $\theta = 21°$. Moreover, current distributions comply with TM modes and beam shapes. Currents are mainly distributed on the ring if the phase difference between the ports is 0° and on the circular patch if the phase difference is 180° as given in Figure 1.4.

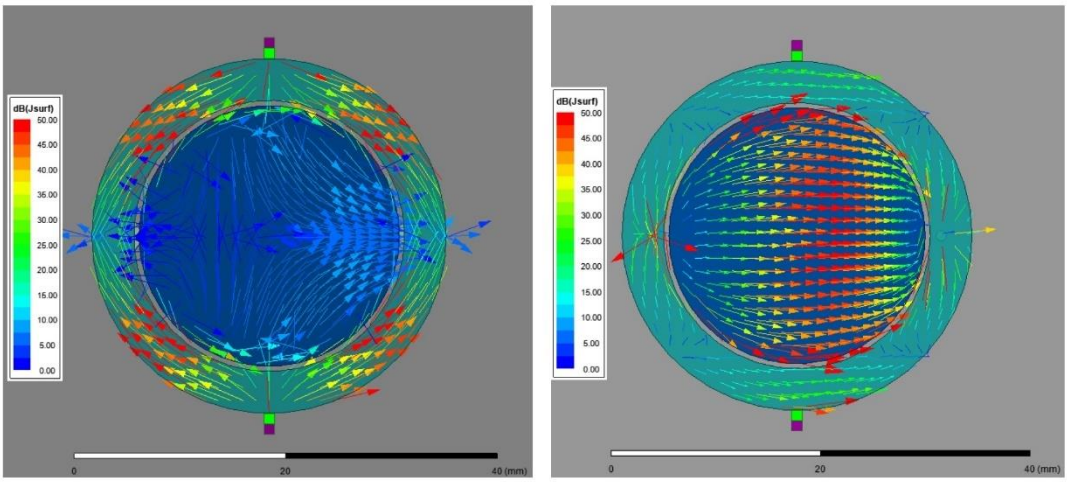

Figure 1.4: Current Distributions for Both Phase Differences [2]

Designed RCPA in [2] works well as a pattern reconfigurable antenna but it is not effective with its S parameters and gain values. $|S_{21}|$ is nearly -0.6 dB at 3.6 GHz. That means strong coupling occurs between the ports. This results in reduction of realized gain of the antenna which is observed and tried to be avoided in [2] by different techniques. To decrease the coupling between the ports, following methods are proposed:

- The ring is shorted to the ground plane at null current positions.
- Slits are etched on the ring at null current positions.

- The ring is divided into two arcs at null current positions.

The maximum improvement is achieved by dividing the ring into two arcs which reduces $|S_{21}|$ to -3.0 dB at 3.6 GHz. It is definitely not a desired decoupling of the ports. It can be seen in values of measured and simulated gains of RCPA. Given gain values in [2] are as follows:

- Conical beam pattern has -3.0 dB simulated realized gain and -3.2 dB measured gain although simulated directivity is 5.1 dB.
- Broadside beam pattern has -2.8 dB simulated realized gain and -2.9 dB measured gain although simulated directivity is 8.1 dB.

By decoupling the ports, $|S_{21}|$ and realized gains can be improved. Thus, it is required to enhance the isolation of the ports to have an efficient pattern reconfigurable antenna.

1.2 Isolation Techniques

Ever since operating multi antennas together in a single system, coupling between the antennas became an issue to be overcome since efficiency and functionality of the antennas are affected by the coupling. To suppress the coupling, various methods have been proposed over the last decade. Even though their goals are generally the same, focus of decoupling varies in studies. Most of the isolation studies are applied to MIMO (multiple-input multiple-output) antennas as they consist of multi antennas.

[3] presents decoupling ground stubs for isolation of planar monopoles. Decoupling is ensured by intercepting currents coupling to the other antenna with the addition of stubs to the ground planes of planar monopoles. In this study, coupling between the planar monopoles without ground stubs is already less than -15 dB and adding ground stubs improves it 5-10 dB in a wide frequency range. That is improving the isolation of already decoupled antennas. This method can not be applied to RCPA

since there is only one antenna element and one ground plane. Besides, coupling of RCPA ports is far worse than planar monopoles without ground stubs.

In [4], closely coupled microstrip patch antennas are decoupled by inserting a meander line resonator in-between. Coupling occurs in a direct path between patch antennas as shown with surface current distributions in Figure 1.5. By offering a resonator, indirect coupling path is created to oppose the direct coupling path without disturbing radiation pattern. Meander line resonator is used for this purpose which fits the gap between patch antennas. Furthermore, antennas, couplings and the resonator are modeled with circuit diagram, and it is consistent with 3D simulations. 8-10 dB improvement is observed in $|S_{21}|$ at operating frequencies. Meander line resonator can be inserted into separated antenna elements but it is not possible in our case. Same situation is also valid for [5]. Instead of meander line resonator, SCSRR (slotted-complementary split-ring resonator) is utilized in [5]. 10 dB decrease in coupling is obtained by adding SCSRR between patch antennas.

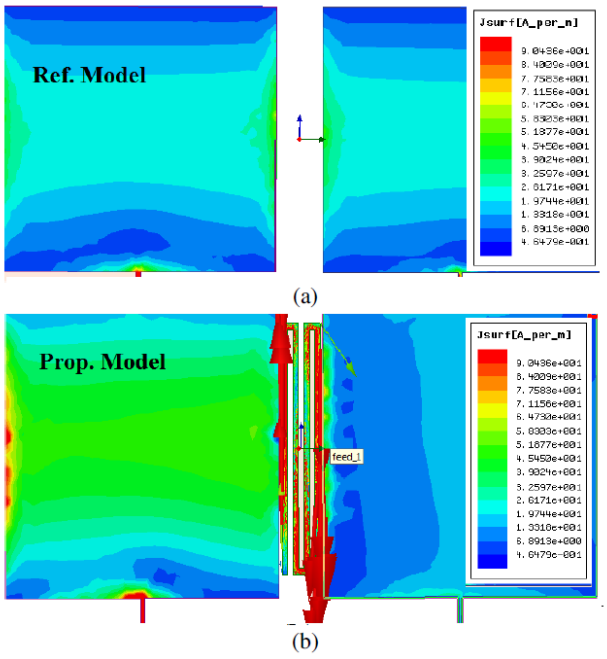

Figure 1.5: Surface Current Distributions. (a) without meander line, (b) with meander line [4]

Metasurfaces can also be used for isolation purposes. SSM (strip structure metasurface) consisting of strips with square slots and CSM (cross structure metasurface) consisting of crossed SSMs are presented in [6] to reduce coupling between two antennas and four antennas, respectively. The metasurfaces behaves like an epsilon-negative and a mu-negative material in desired bands. Less than -30 dB coupling can be achieved with this metasurfaces. CSM is effective considering separated antennas with less than -30 dB coupling but in this study, coupling is already less than -15 dB without CSM so the technique is applied to relatively easier case. This structure is not a good candidate for RCPA.

Another type of metasurfaces is exploited in [7] to depress the coupling between nearby antenna elements. SRR elements are placed around the antennas so that they can distort the coupling energy occurred between the antenna elements. Coupling is reduced from -8 dB to -25 dB with this method. Although this technique looks easier to implement, RCPA does not have any second antenna element.

Decoupling line technique in [8] is different from above techniques by considering its implementation. It focuses on the feed lines rather than the antenna elements. A decoupling line is designed and placed between the feed lines of coupled antennas as shown in Figure 1.6. To achieve decoupling, even and odd mode analysis is conducted for 4-port network constituted by the antennas and the decoupling line. Transmission coefficient is obtained with the analysis and tried to be vanished by deciding values of θ_1, θ_d and Z_d. With the optimization of these three parameters, decoupling line is fully designed. Finally, matching networks are added after the decoupling line to match the ports. Here, the coupling reduces to a value of less than -20 dB with addition of a simple line and matching networks. However, better decoupling techniques based on mathematical calculations are found instead of doing optimization to calculate parameters, θ_1, θ_d and Z_d.

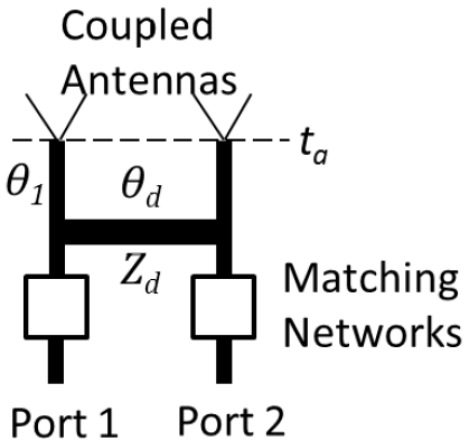

Figure 1.6: Decoupling Line Technique [8]

For example, [9] offers a decoupling network that can be applied between feed lines like [8]. As shown in Figure 1.7, a reactive element (inductive or capacitive) is exploited instead of decoupling line given in Figure 1.6. Here, decoupling network consists of transmission lines extending from the antennas and a reactive element. In this study, the goal is to vanish S_{21} by making Y_{21} zero since S_{21} and Y_{21} are directly proportional to each other as seen in conversion matrix from Y parameters to S parameters in Appendix A. To make Y_{21} zero, an appropriate point on the transmission line, which is electrical length θ away from the antennas, is found. At this point, real part of Y_{21} is equal to zero. Imaginary part of Y_{21} is canceled out by inserting a reactive element with jB susceptance. Thus, overall Y_{21} becomes zero. However, it is not enough to complete the design. Matching networks are added just after the decoupling network to match the ports. It is a better method than the previous one since value of the reactive element and electrical length θ can be found with mathematical formulations. Also, it gives us two options as a lumped element: inductor or capacitor. [10] and [11] contain similar procedures with different decoupling networks. In fact, formulations in [10] are more rigorous and easier to follow. Their decoupling networks include low temperature cofired ceramic (LTCC)

devices which make the design more expensive and complicated. Likewise, two studies [12], [13], which utilize coupled resonators as decoupling network in a similar manner are worth to mention. Their design is more complex compared to decoupling network with a lumped element.

Hence, in this thesis, decoupling network technique in [9] is implemented to RCPA to improve isolation between its ports. In the literature, the decoupling network is used to decouple two antenna elements. In our study, different from the literature, the decoupling network is applied to decrease the coupling between two ports of the same antenna element. Details of the technique will be examined in Chapter 3.

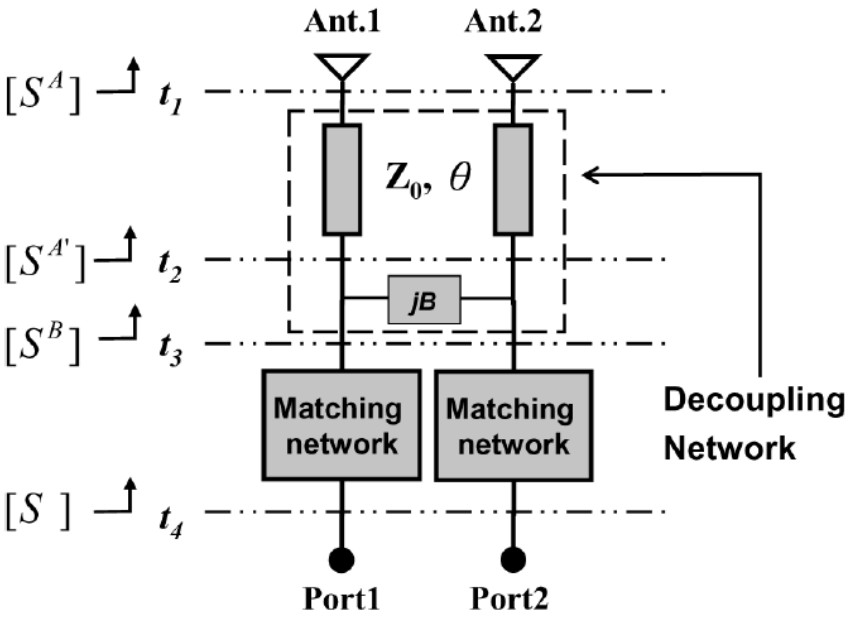

Figure 1.7: Decoupling Network Technique [9]

1.3 Outline of the Thesis

This thesis introduces a decoupling network and its implementation to a multi-functional antenna to improve the isolation between its strongly coupled ports. Decoupling network will be applied to the ports of RCPA proposed in [2]. However, it is applicable between two feed lines and the antenna in [2] is a probe-fed antenna. Therefore, first, aperture coupled RCPA design will be presented in Chapter 2 to obtain an antenna with microstrip line ports.

Chapter 3 consists of theory of decoupling network and design of inductive and capacitive decoupling networks for RCPA. The main theory and the designs are detailed with derivations, calculations and simulations.

In Chapter 4, first, designed RCPA is fabricated. Fabrication related problems are discussed. Antenna is slightly modified to take account fabrication imperfections. Decoupling network is implemented to fabricated antenna. S parameters of RCPA with and without decoupling network are measured and compared with simulations. Moreover, anechoic chamber measurements are carried out. Radiation patterns and gain values are compared with simulations. To sum up, decoupling network design is verified.

Chapter 5 concludes the thesis with review and evaluation. Feasible future works are also mentioned in this chapter.

CHAPTER 2

APERTURE COUPLED MULTI-FUNCTIONAL ANTENNA DESIGN

Decoupling network with a lumped component is a good candidate to improve the isolation between two ports of the ringed circular patched antenna proposed in [2], but probe feeding is not suitable to integrate the lumped element. Thus, aperture coupled feeding approach [14] is applied to this antenna.

Aperture-coupled RCPA is designed by preserving the dielectric substrate and the operating frequency same as in [2]. The antenna is placed onto RO4003C ($\varepsilon_r = 3.55$, $\tan \delta = 0.0027$) substrate with 1.524 mm thickness. Top side of the substrate is etched to have a circular patch and a ring around it. For aperture coupling, there are two slots located at the bottom side of the substrate. Moreover, another RO4003C substrate with 0.508 mm thickness is prepared for microstrip lines feeding the antenna ports. On this substrate, the width of the microstrip lines with 50 **Ω** characteristic impedance is found to be 1 mm. The size of the substrates for both layers is 75 mm x 75 mm. Isometric view of aperture coupled RCPA is shown in Figure 2.1 and feeding slots are shown in Figure 2.2.

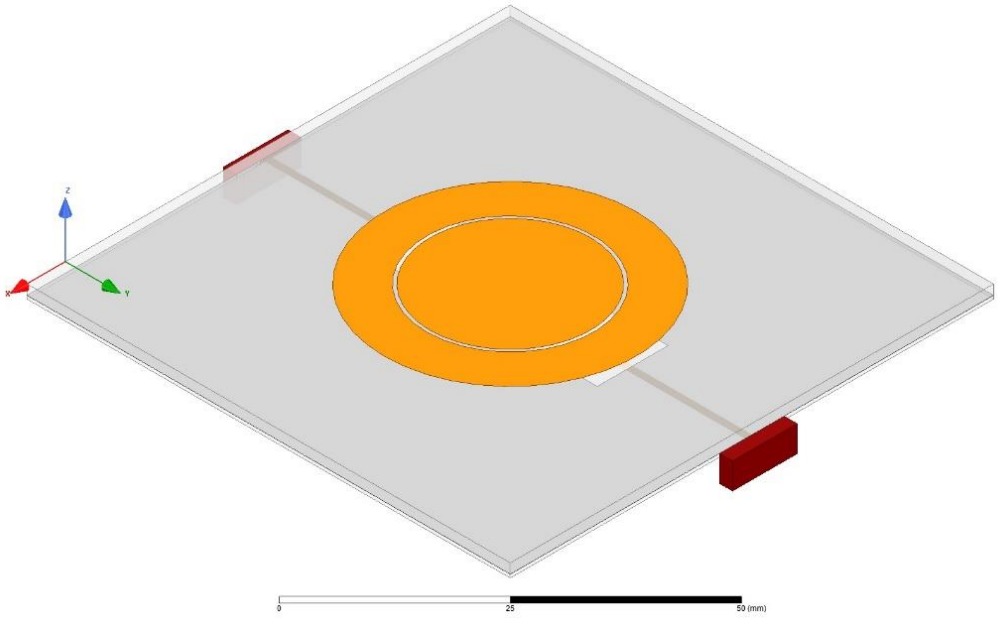

Figure 2.1: Aperture Coupled RCPA Geometry

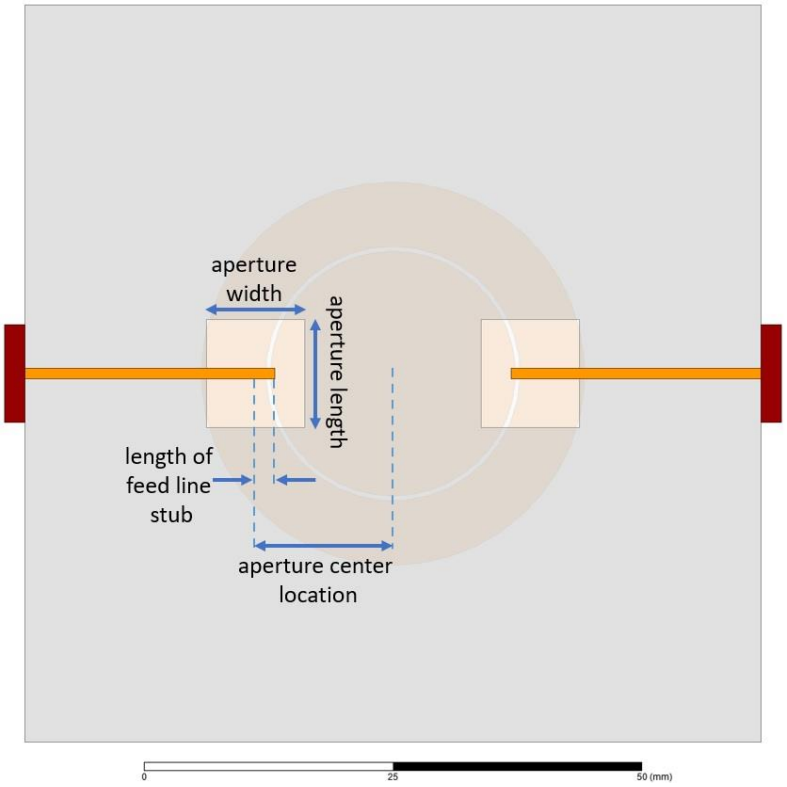

Figure 2.2: AC RCPA Slots and Feed Lines

Since the feeding method is changed, some parametric sweeps are carried out to optimize antenna parameters, especially aperture parameters. Antenna dimensions in [2] are preserved as given in Table 2.1. For full-wave electromagnetic simulations, finite element based HFSS software developed by ANSYS is used. Here, the most effective parameter is aperture width. Keeping aperture length constant, 11 mm, aperture width is swept from 2 mm to 12 mm. As seen in Figure 2.3, the best resonance at 3.6 GHz is observed with 10 mm aperture width. In conventional aperture coupled microstrip antenna structures, aperture width is generally much shorter than aperture length as in [14] but in our case, better coupling between the microstrip line and the antenna is achieved by enlarging the aperture width. Moreover, aperture width has a crucial role on resonant frequency. Hence, by varying the aperture width, resonant frequency of the antenna can be tuned as can be observed in Figure 2.3.

Table 2.1: Probe-fed RCPA Dimensions

Parameter	**Dimension**
Circular patch radius	12.45 mm
Ring inner radius	12.95 mm
Ring outer radius	19.5 mm

Furthermore, after setting aperture width to 10 mm, sweeps of other aperture parameters depicted in Figure 2.2 are shown in following figures: aperture length in Figure 2.4, aperture center location from the origin in Figure 2.5 and length of feed line stub in Figure 2.6. Figure 2.4 and Figure 2.5 show that aperture length and aperture center location slightly change the resonant frequency while depth of the resonance is affected considerably by these two parameters. As seen in Figure 2.6, length of feed line stub is the most crucial parameter to match the input impedance of the antenna. Optimized antenna parameters are tabulated in Table 2.2.

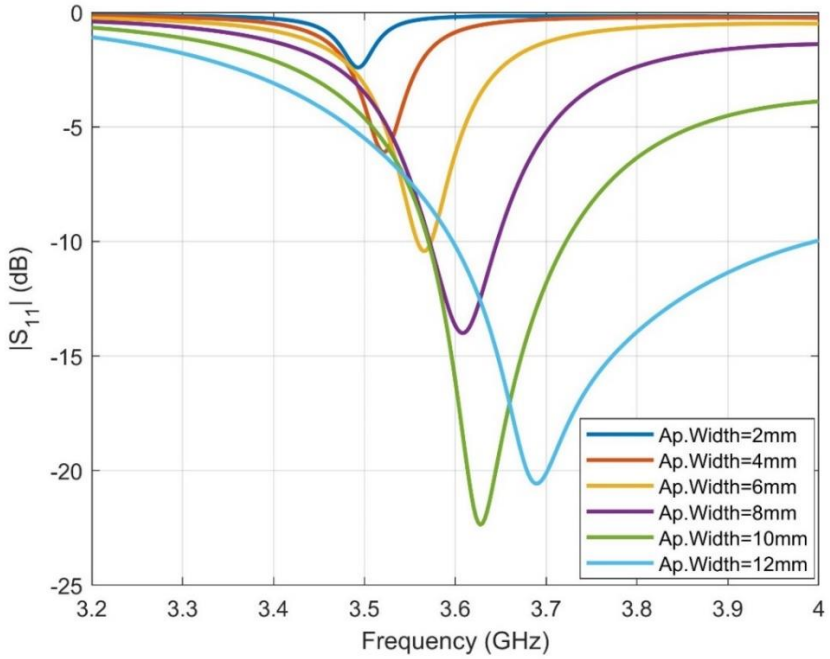

Figure 2.3: $|S_{11}|$, Aperture Width Sweep

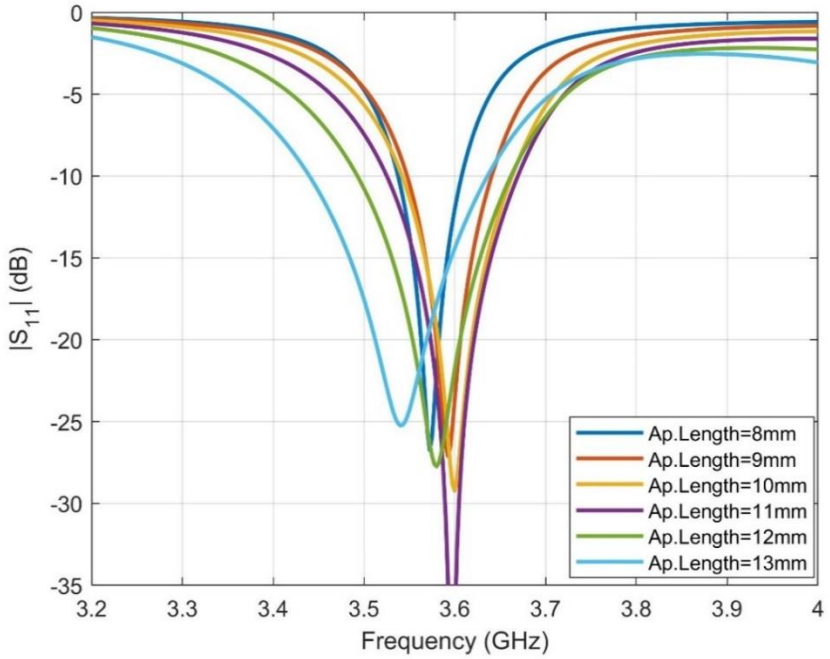

Figure 2.4: $|S_{11}|$, Aperture Length Sweep

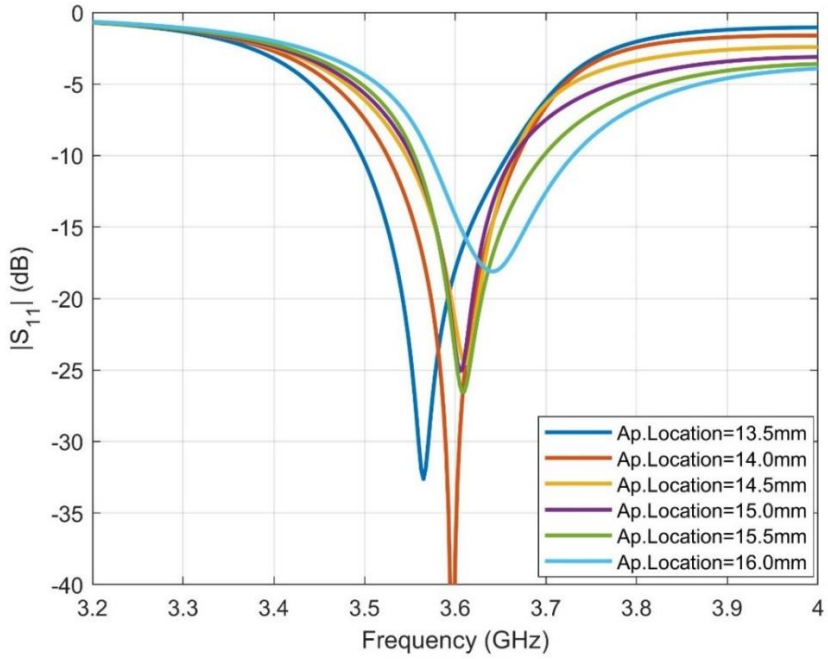

Figure 2.5: $|S_{11}|$, Aperture Center Location Sweep

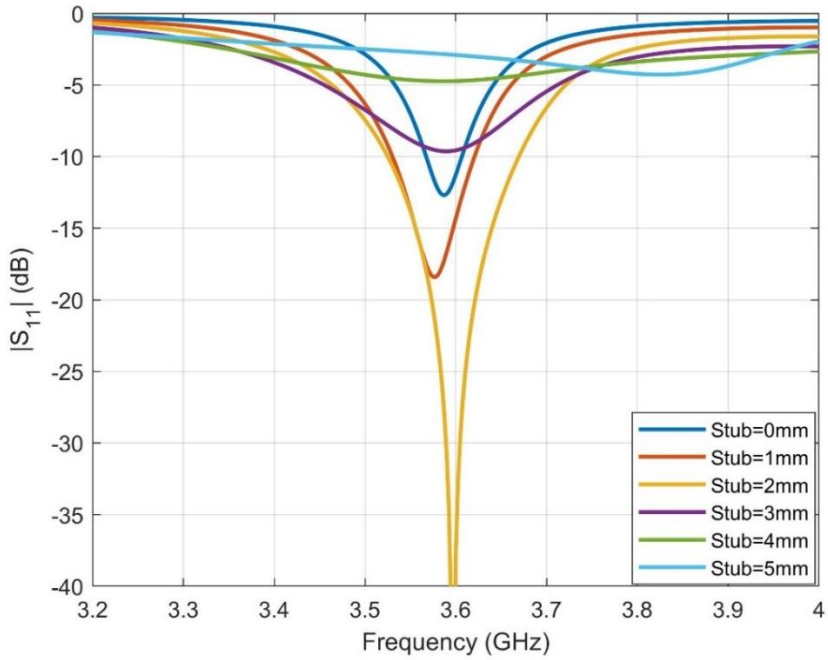

Figure 2.6: $|S_{11}|$, Length of Feed Line Stub Sweep

Table 2.2: AC RCPA Optimized Antenna Parameters

Parameter	Dimension
Aperture center location, from the origin	14 mm
Aperture width	10 mm
Aperture length	11 mm
Length of feed line stub	2 mm

S parameters of designed aperture coupled RCPA are given in Figure 2.7. Due to the symmetry, $|S_{11}|$ and $|S_{22}|$ overlap. As seen, $|S_{21}|$ at 3.6 GHz is reduced to -3.5 dB which is an improvement as compared to probe fed RCPA ($|S_{21}|$ = -0.6 dB) in [2]**.** This improvement shows itself on realized gains. In probe fed RCPA, simulated realized gains are -3.0 dB and -2.8 dB for conical beam and broadside beam, respectively. Here, in this feeding method, realized gains increase more than 6 dB and most importantly, they attain positive values. Conical beam (the phase difference between the ports is 0°) pattern is shown in Figure 2.8 and broadside beam (the phase difference between the ports is 180°) pattern is shown in Figure 2.9. Their realized gains are around 3.9 dB and 4.4 dB, respectively.

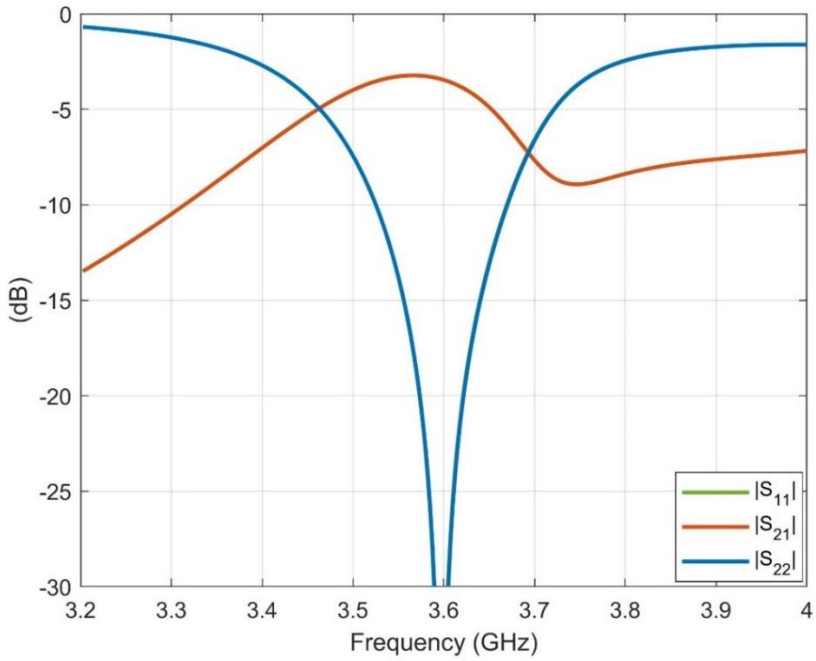

Figure 2.7: S Parameters of Optimized RCPA

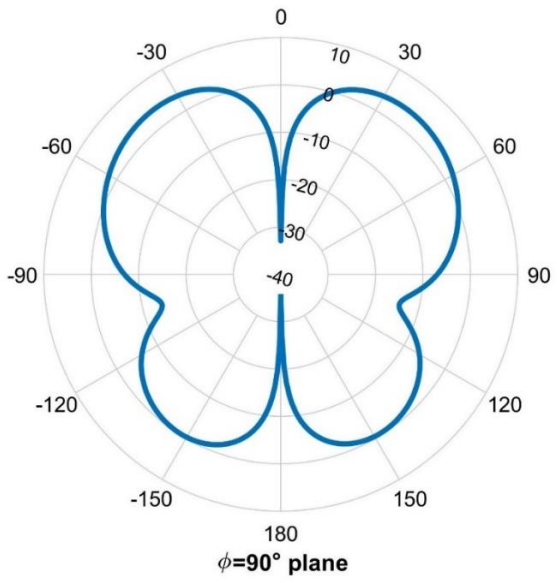

Figure 2.8: AC RCPA Realized Gain Pattern, Conical Beam (PD: 0°) at $\phi = 90°$ Plane

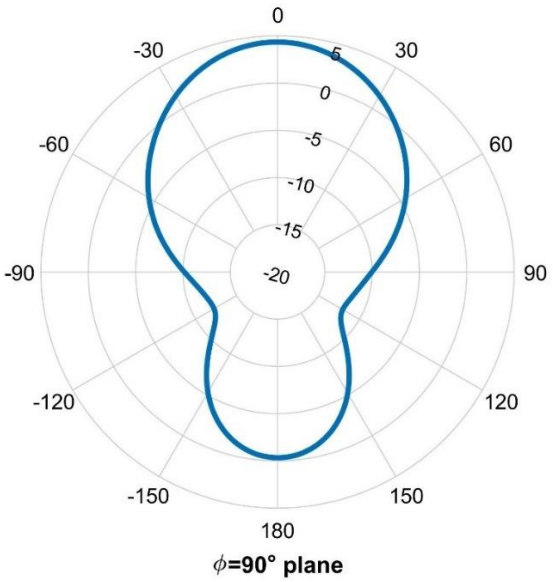

Figure 2.9: AC RCPA Realized Gain Pattern, Broadside Beam (PD: 180°) at $\phi = 90°$ Plane

As understood from the patterns, beam steering feature of RCPA is conserved with aperture coupled feeding. Conical beam has the peak at -38° with 3.9 dB while broadside beam has the peak at 0° with 4.4 dB. That is in accordance with the current distributions given in Figure 2.10 and Figure 2.11. When the phase difference is 0°, ring of the antenna is excited at TM_{21} mode which creates conical beam. In Figure 2.10, surface currents are mainly on the ring. On the other hand, 180° phase difference excites the circular patch of the antenna at TM_{11} mode which creates broadside beam. In Figure 2.11, surface currents spread around the circular patch. Thus, it can be said that RCPA is successfully redesigned at 3.6 GHz with aperture coupled feeding technique.

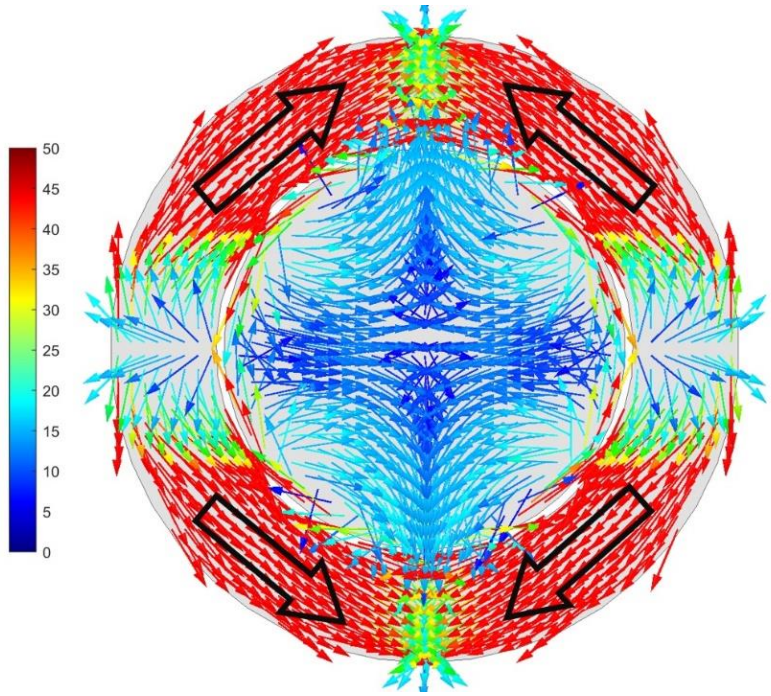

Figure 2.10: Current Distribution with 0° Phase Difference

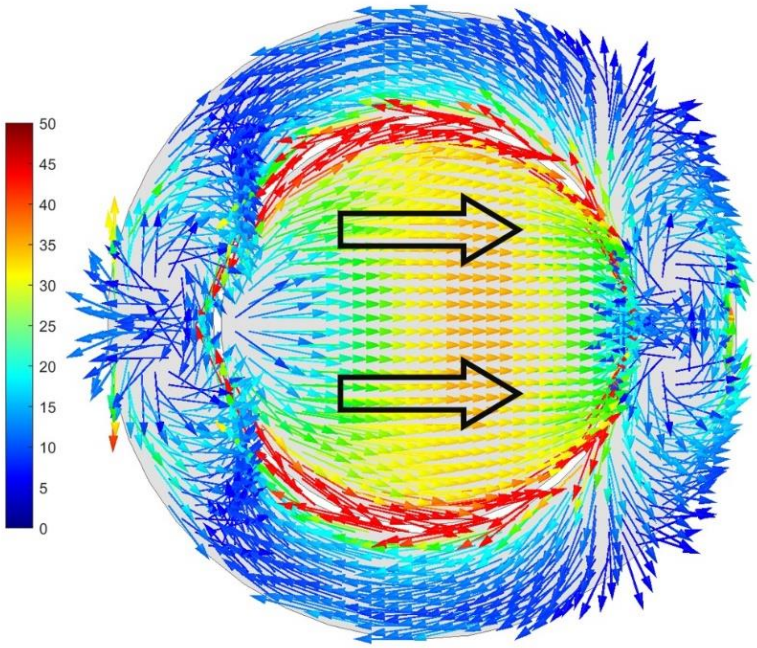

Figure 2.11: Current Distribution with 180° Phase Difference

2.1 Back Lobe Suppression

With aperture coupling, isolation between ports is increased but back radiation increases too due to radiation of the apertures. Front to back ratios are around 5 dB which is very poor. Therefore, to suppress the back lobes, a PEC (perfect electric conductor) plate is placed behind the bottom of RCPA where feed lines are located as in [15]. The new structure is illustrated in Figure 2.12. The plate distance is adjusted to be $\lambda_0/4$. At 3.6 GHz, plate distance is approximately 20.8 mm.

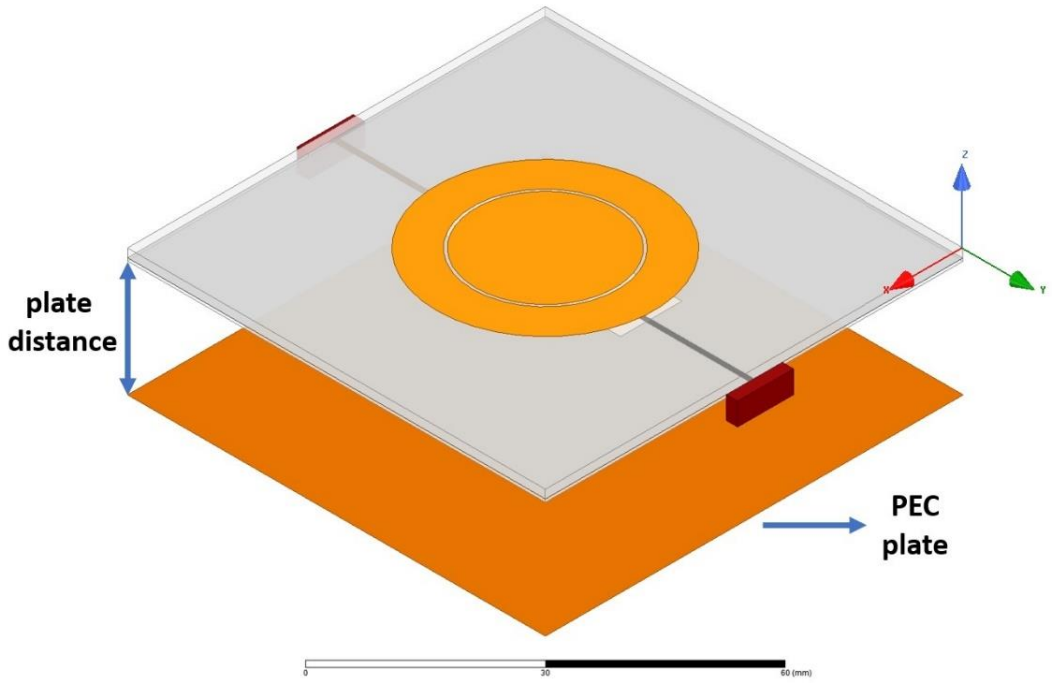

Figure 2.12: RCPA Structure with PEC Plate

First, S parameters of the new structure are compared with the one without PEC plate to make sure that only the patterns are affected by the addition of the plate. As seen in Figure 2.13, S parameters are almost the same as expected since the PEC plate is far enough from the antenna.

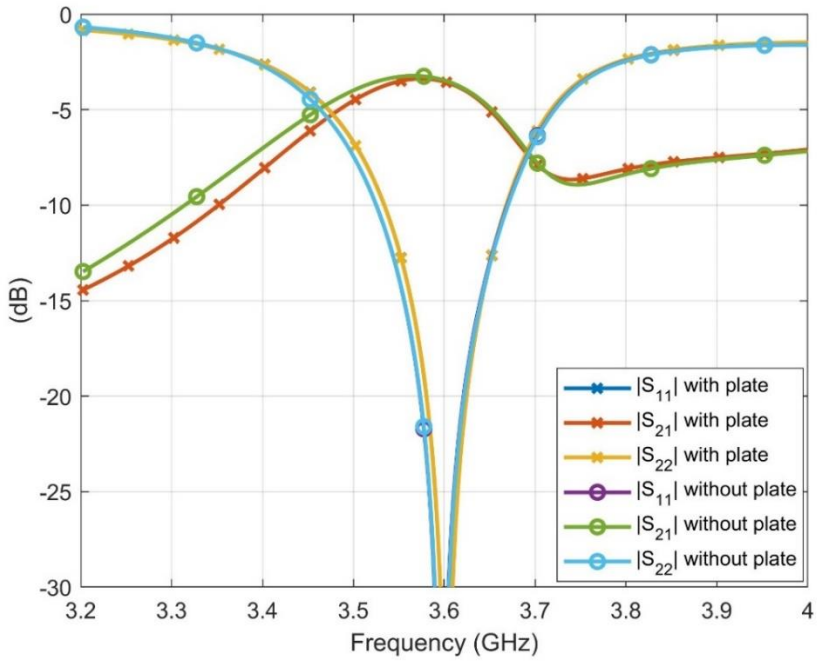

Figure 2.13: S Parameters with&without PEC Plate

Second, radiation patterns are plotted in Figure 2.14 and Figure 2.15 for conical beam and broadside beam, respectively. In front to back ration, more than 6 dB enhancement in conical beam and more than 9 dB enhancement in broadside beam are obtained by adding reflecting plate to the structure. Broadside gain is increased from 6.9 dB to 7.1 dB and conical gain is increased from 6.6 dB to 8.0 dB with the addition of PEC plate.

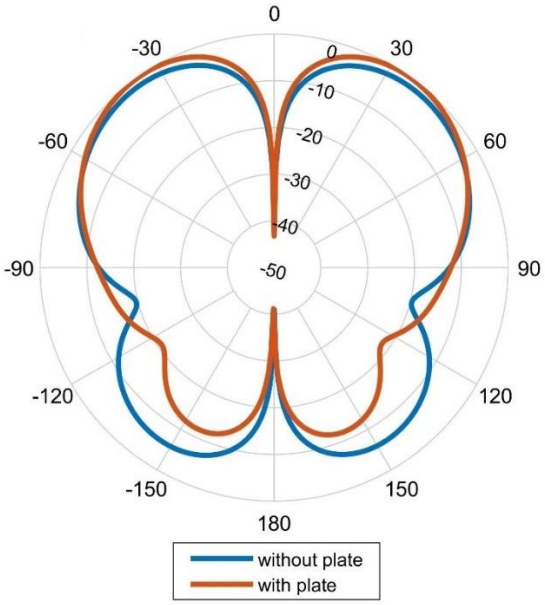

Figure 2.14: Normalized Radiation Patterns with&without PEC Plate, Conical Beam at $\phi = 90°$ Plane

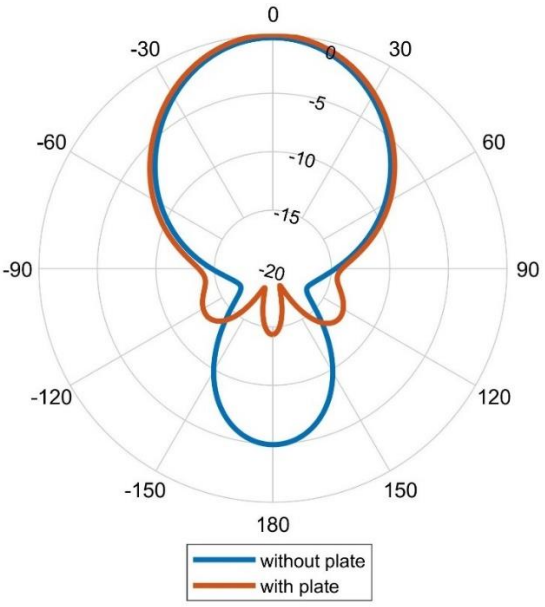

Figure 2.15: Normalized Radiation Patterns with&without PEC Plate, Broadside Beam at $\phi = 90°$ Plane

To sum up, in this chapter, pattern reconfigurable ringed circular patch antenna proposed in [2] is redesigned with aperture coupled feeding method instead of probe feeding. In this way, with the help of microstrip lines, decoupling network, which will be explained in detail in the next chapter, can be inserted between the antenna ports. Also, it is shown that realized gain is increased as compared with the probe fed RCPA. That is an extra achievement even before the implementation of decoupling network.

On the other hand, one disadvantage of the aperture coupled RCPA is complexity of the antenna. In probe-fed antenna, probes are directly soldered to the ring of RCPA, but aperture coupled RCPA requires another substrate to be allocated for feed lines. Not only production of the new substrate but also alignment of two substrates creates the complexity.

CHAPTER 3

DECOUPLING NETWORK

Different techniques to reduce antenna couplings have been investigated in many studies as reviewed in Section 1.2. Most of them are for decoupling of two different antennas. Two antennas separated in space may have different polarizations or operating frequencies. Therefore, they mainly focus on isolation of two radiating elements but in our case, there is only one antenna and isolation between its two ports is required. As mentioned earlier, pattern reconfigurable antenna, namely RCPA (ringed circular patch antenna), has two ports in which phase difference allows the pattern reconfiguration. Here, our goal is to decouple these two ports to enhance realized gain of the antenna.

Chen et al. [9] presents a decoupling technique for increasing the isolation between two antennas which is applicable to aperture coupled RCPA. It is due to appropriate structure of the antenna. That is, RCPA is fed by microstrip lines, and the decoupling network can be inserted between these lines easily. Two similar studies are carried out in [10] and [11] with low temperature cofired ceramic (LTCC) devices to isolate closely coupled two antennas. Even though both can be applied to RCPA, LTCC devices are not used in this thesis because of the manufacturing incapability. All of the above are inspired from similar idea that aims to decrease $|S_{21}|$ between the ports by making $|Y_{21}|$ zero.

3.1 Theory of Decoupling Network

In this thesis, the formulation to calculate the parameters of the decoupling network is adopted from [10] but instead of LTCC devices, a reactive lumped element is utilized as in [9].

Antenna and decoupling network can be represented as two port networks as shown in Figure 3.1. Admittance matrices depicted below are stated in Equation 3.1 and Equation 3.2 for antenna and decoupling network, respectively.

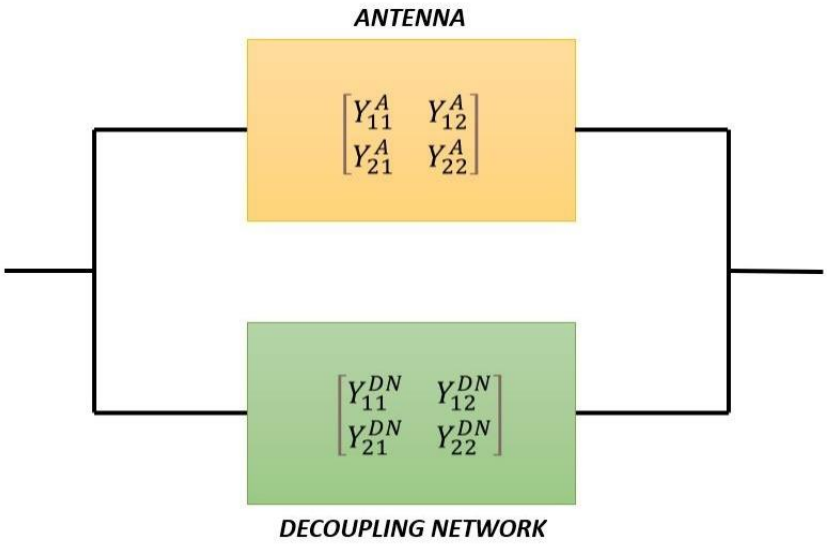

Figure 3.1: Network Representation of Parallel Connected Antenna and Decoupling Network

$$Y^{A} = \begin{bmatrix} Y_{11}^{A} & Y_{12}^{A} \\ Y_{21}^{A} & Y_{22}^{A} \end{bmatrix} \tag{3.1}$$

$$Y^{DN} = \begin{bmatrix} Y_{11}^{DN} & Y_{12}^{DN} \\ Y_{21}^{DN} & Y_{22}^{DN} \end{bmatrix} \tag{3.2}$$

In our case, Y^A represents admittance matrix formed by two ports of RCPA whereas it is the admittance matrix of coupled antennas in [10]. When they are shunt connected, their admittance matrices can be summed, and the total admittance matrix becomes as the following:

$$Y^T = \begin{bmatrix} Y_{11}^T & Y_{12}^T \\ Y_{21}^T & Y_{22}^T \end{bmatrix} = Y^A + Y^{DN} \tag{3.3}$$

$$Y^T = \begin{bmatrix} Y_{11}^{DN} + Y_{11}^A & Y_{12}^{DN} + Y_{12}^A \\ Y_{21}^{DN} + Y_{21}^A & Y_{22}^{DN} + Y_{22}^A \end{bmatrix} \tag{3.4}$$

Aiming isolation of the ports leads us to vanish Y_{21}^T around the resonant frequency of RCPA which is 3.6 GHz. That is, coupling between the ports of RCPA can be eliminated by making Y_{21}^T zero. Conversion from Y parameters to S parameters is given in Appendix A. As seen, Y_{21} is a multiplier in S_{21}. Therefore, S_{21} becomes zero along with Y_{21} around the resonant frequency.

Y_{21}^T does not necessarily have to be exactly zero. If it is around zero as in Equation 3.5, good isolation can still be ensured.

$$Y_{21}{}^T = Y_{21}{}^A + Y_{21}{}^{DN} \approx 0 \tag{3.5}$$

Now, Y_{21} parameters are separated into real and imaginary parts,

$$Y_{21}{}^T = Re\{Y_{21}{}^T\} + jIm\{Y_{21}{}^T\} \tag{3.6}$$

$$Y_{21}{}^A = Re\{Y_{21}{}^A\} + jIm\{Y_{21}{}^A\} \tag{3.7}$$

$$Y_{21}{}^{DN} = Re\{Y_{21}{}^{DN}\} + jIm\{Y_{21}{}^{DN}\} \tag{3.8}$$

Equation 3.5 can be rewritten by combining Equations 3.6 to 3.8,

$$Re\{{Y_{21}}^{T}\} + jIm\{{Y_{21}}^{T}\} = Re\{{Y_{21}}^{A}\} + jIm\{{Y_{21}}^{A}\} + Re\{{Y_{21}}^{DN}\} + jIm\{{Y_{21}}^{DN}\}$$

$$\approx 0 \tag{3.9}$$

Equating real parts of Equation 3.9,

$$Re\{{Y_{21}}^{T}\} = Re\{{Y_{21}}^{A}\} + Re\{{Y_{21}}^{DN}\} \approx 0 \tag{3.10}$$

Since the decoupling network consists of a reactive lumped element which is purely imaginary, real part of ${Y_{21}}^{A}$ should be zero. This is the first condition for decoupling.

$$Re\{{Y_{21}}^{A}\} \approx 0 \tag{3.11}$$

In order to satisfy the first condition, transmission lines with characteristic impedance Z_0 and electrical length θ are added right after the antenna ports as illustrated in Figure 3.2. Characteristic impedance Z_0 is 50 Ω in this system. To find the electrical length θ, antenna port coupling, ${S_{21}}^{A}$, is expressed as

$${S_{21}}^{A} = |S_{21}|e^{j\phi_{21}} \tag{3.12}$$

Hence, θ can be derived from Equation 3.13 [9].

$$\theta = \frac{1}{2}[\phi_{21} \pm \pi/2] \tag{3.13}$$

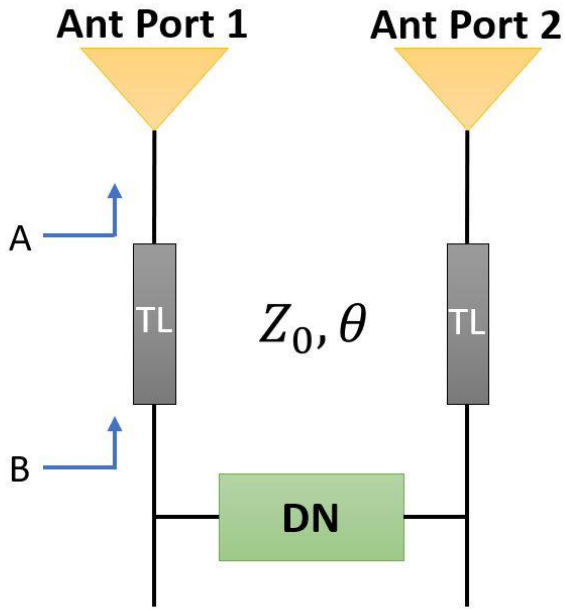

Figure 3.2: Antenna Ports Connection to Decoupling Network Via Transmission Lines

Then, consider the imaginary parts of Y_{21} parameters in Equation 3.9,

$$Im\{{Y_{21}}^{T}\} = Im\{{Y_{21}}^{A}\} + Im\{{Y_{21}}^{DN}\} \approx 0 \tag{3.14}$$

Therefore, the second condition for decoupling is to have a decoupling network which compensates the imaginary part of ${Y_{21}}^{A}$. It can be either inductive or capacitive depending on the sign of $Im\{{Y_{21}}^{A}\}$. If $Im\{{Y_{21}}^{A}\}$ at plane B, shown in Figure 3.2, is capacitive then the decoupling network is an inductor and vice versa. Second condition is simply,

$$Im\{{Y_{21}}^{A}\} + Im\{{Y_{21}}^{DN}\} \approx 0 \tag{3.15}$$

By satisfying two conditions for decoupling, $Y_{21} = 0$ so $S_{21} = 0$. However, after inserting decoupling network, antenna ports are no longer matched to 50 Ω as expected so a matching network is required to match the new configuration with decoupling network. As a matching network, among many techniques, single stub matching used in [10] and LC matching used in [9] are most preferred ones because of their effectiveness and implementation easiness. Finally, looking at input Z (or Y) parameters at plane C shown in Figure 3.3, a matching network can be designed and introduced to have matched overall structure at plane D as

$$Re\{{Y_{kk}}^{T}\} \approx Y_0 \,, \qquad \text{k=1, 2} \qquad (3.16)$$

$$Im\{{Y_{kk}}^{T}\} \approx 0 \,, \qquad \text{k=1, 2} \qquad (3.17)$$

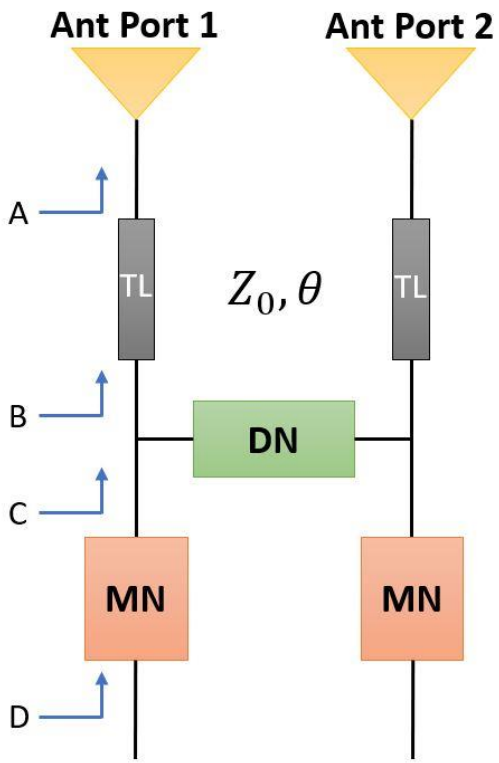

Figure 3.3: Decoupled and Matched Antenna Scheme

3.2 Modified RCPA Design to Integrate Decoupling Network

Decoupling network can be applied to aperture coupled RCPA designed in previous chapter but the structure is not convenient to put decoupling network between the ports of RCPA. That is, ports are far away from each other and a lumped element can not be soldered by inspecting Figure 2.2. To overcome this physical problem, two approaches can be followed. First one is extending feed lines from the ports to a common point in which the lumped element can be added as demonstrated in Figure 3.4. Second one is making feed lines come close to each other then adding the lumped element to the designed place as Figure 3.5 shows. Thus, latter alternative is chosen since it is simpler to implement. Extended feed lines in the first alternative should also be taken into account to satisfy the condition on real part of Y_{21} which makes the design more complicated.

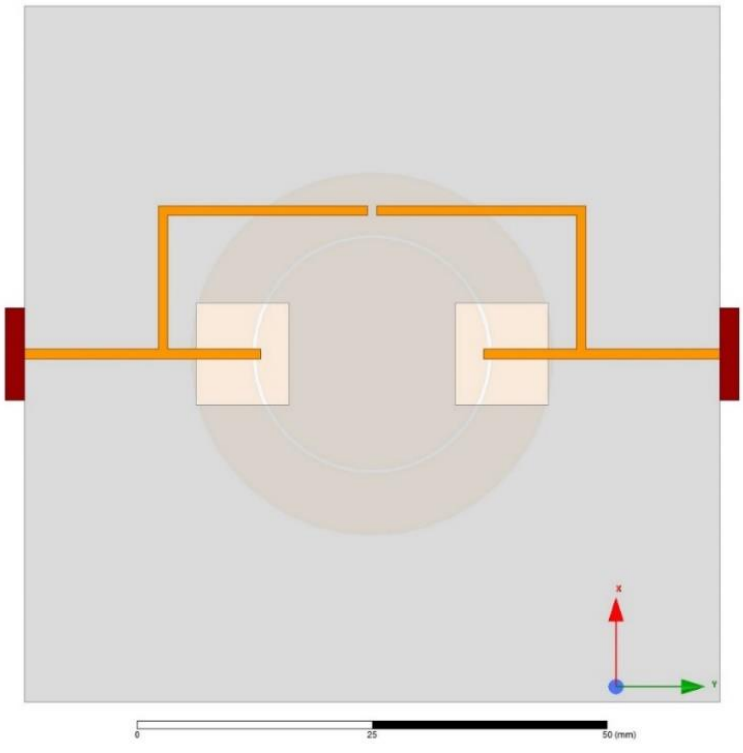

Figure 3.4: Extension of Feed Lines

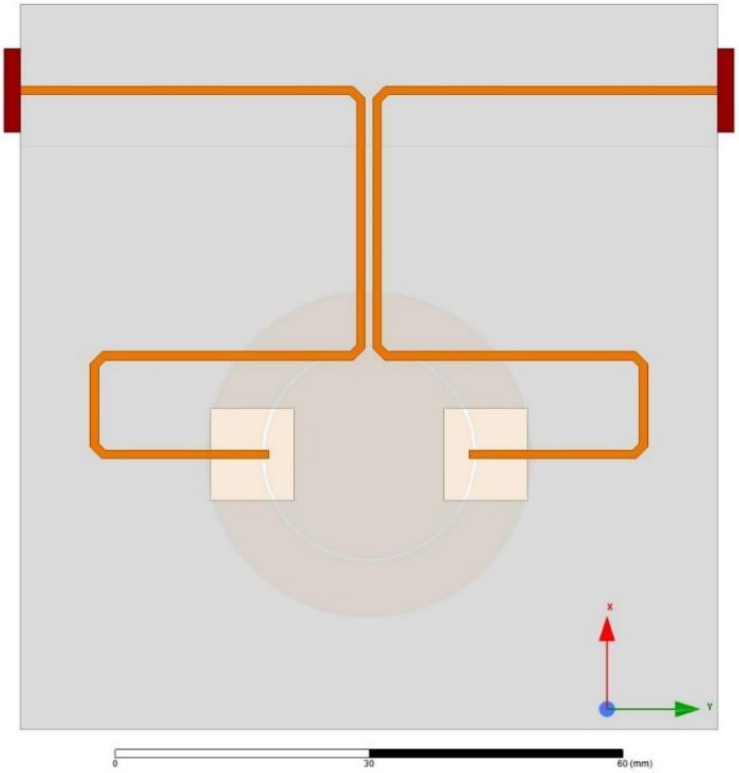

Figure 3.5: Appropriate Configuration of Feed Lines for Decoupling Network

In the new structure, the feed lines shown in Figure 3.5 are arranged to host the lumped element. The minimum distance between the lines is set as 1 mm so that 0603 SMD (surface mount device) lumped element can be easily soldered between the lines. Moreover, the length of lines where they come closer to each other is 30 mm which is longer than the quarter wavelength at 3.6 GHz. The reason for that is two locations that makes real part of Y_{21} zero are $\lambda/4$ apart. One location requires an inductive element, the other one requires a capacitive element to make imaginary part of Y_{21} zero. Thus, 30 mm is sufficient to accommodate these two solutions.

Besides changing the feed lines, port locations and antenna substrate are modified. As shown in Figure 3.6, ports are moved to the end of feed substrate in +x direction and antenna substrate is trimmed in order to mount SMA connectors because ground plane between the substrates should be exposed for the utilization of SMA

connectors. Also, substrate sizes are adjusted to suit above modifications. Updated antenna substrate and feed substrate sizes are 70 mm x 83.5 mm and 87 mm x 83.5 mm, respectively.

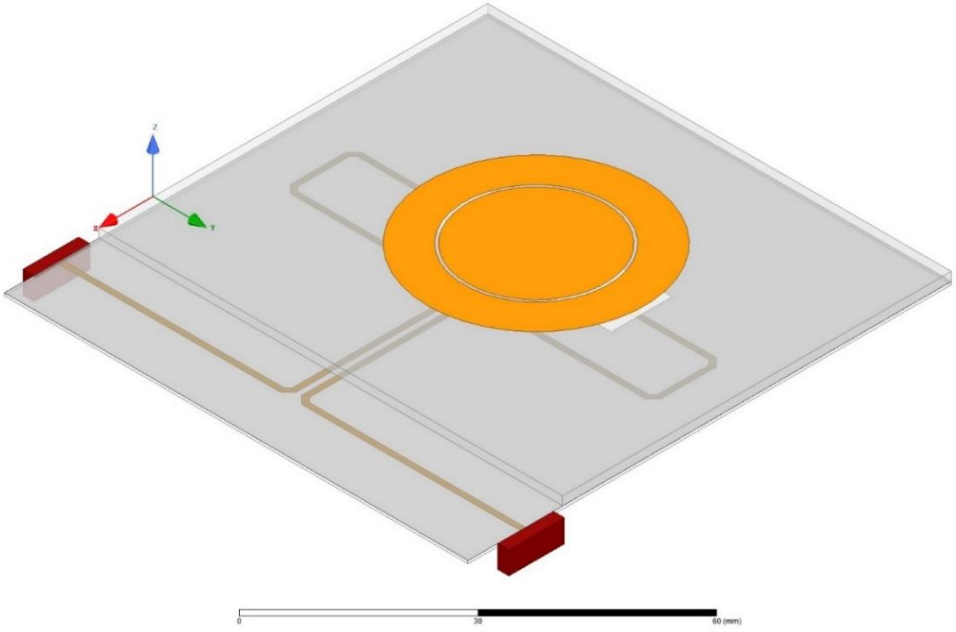

Figure 3.6: Modified AC RCPA Geometry

Modified RCPA is simulated in HFSS. S parameters and radiation patterns with gain values of RCPA without decoupling network are plotted in Figure 3.7 and Figure 3.8-3.12, respectively. A slight shift in resonance frequency is observed in Figure 3.7 but 3.6 GHz is still within 10 dB return loss bandwidth.

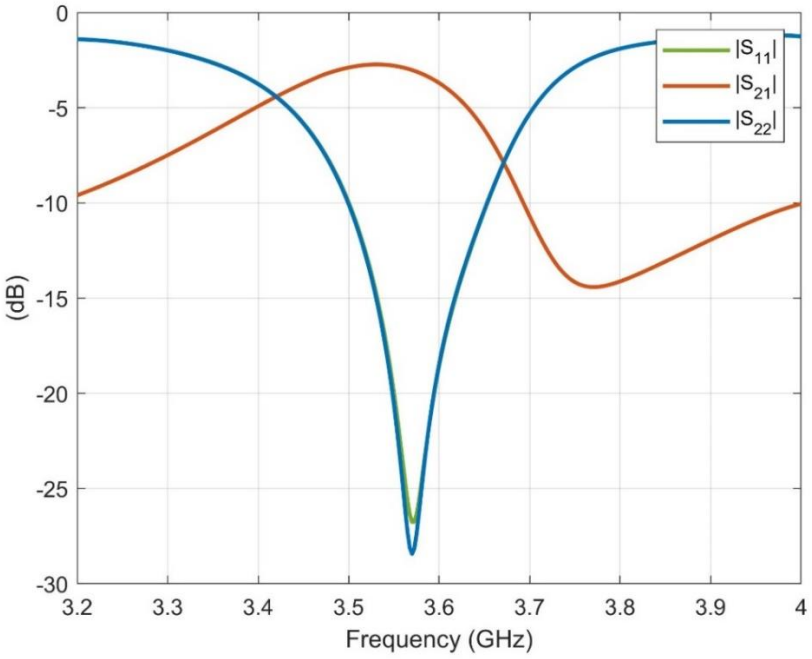

Figure 3.7: RCPA without Decoupling Network S Parameters

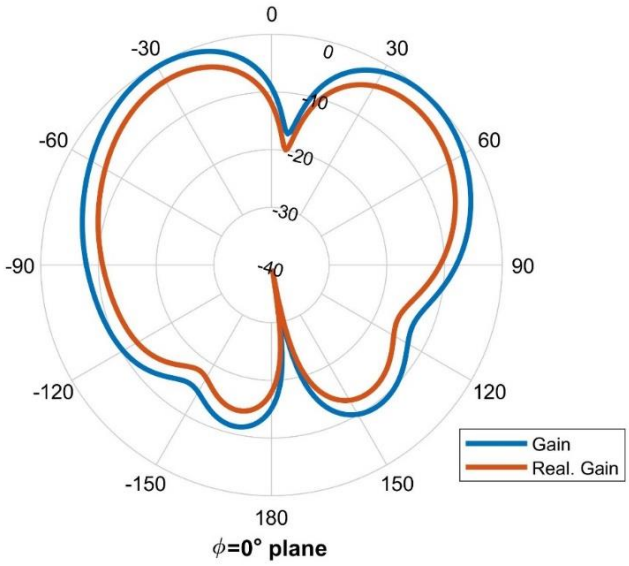

Figure 3.8: RCPA without Decoupling Network Radiation Patterns, Conical Beam (PD: 0°) at $\phi = 0°$ Plane

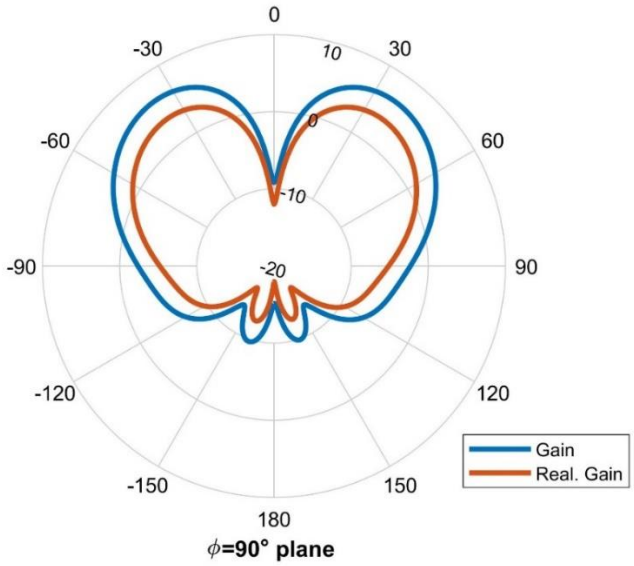

Figure 3.9: RCPA without Decoupling Network Radiation Patterns, Conical Beam (PD: 0°) $\phi = 90°$ Plane

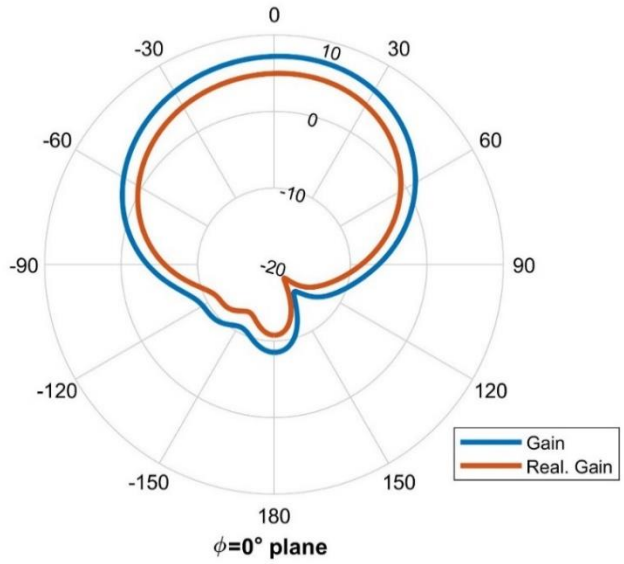

Figure 3.10: RCPA without Decoupling Network Radiation Patterns, Broadside Beam (PD: 180°) at $\phi = 0°$ Plane

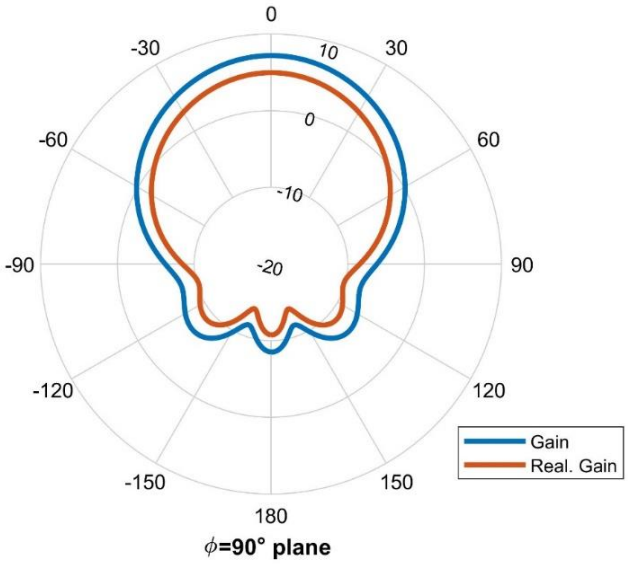

Figure 3.11: RCPA without Decoupling Network Radiation Patterns, Broadside Beam (PD: 180°) at $\phi = 90°$ Plane

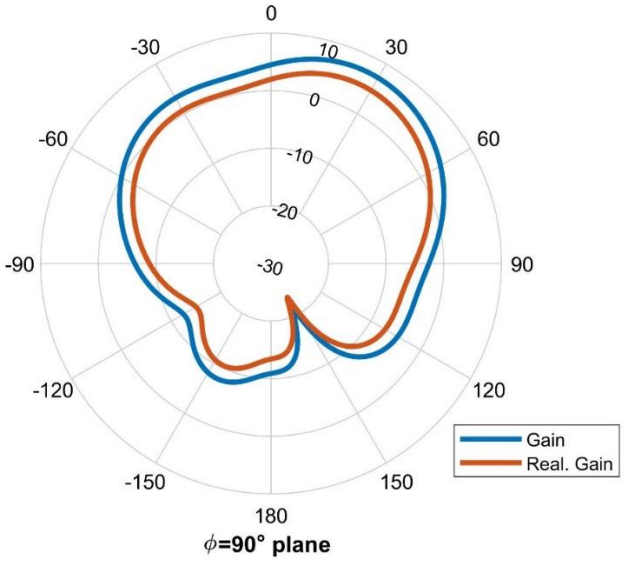

Figure 3.12: RCPA without Decoupling Network Radiation Patterns, PD: 90° at $\phi = 90°$ Plane

As seen in Figure 3.9 and Figure 3.11, conical beam has the peak at $\theta = 37°$ and broadside beam has the peak at $\theta = 0°$ as expected. Also, to verify the beam steering with changing phase difference between the ports, radiation patterns of 90° phase difference is included in this section. Its peak is at $\theta = 28°$ which is between the peaks of conical and broadside beams. Owing to asymmetry in antenna geometry seen in Figure 3.6, patterns in $\phi = 0°$ planes are not symmetrical.

The relation between realized gain -also known as absolute gain- and gain is given as, [1],

$$G_r(\theta, \phi) = (1 - |\Gamma|^2)\, G(\theta, \phi) \tag{3.18}$$

When second port is excited, coupling from second port to first port affects first port's reflection coefficient and vice versa. That is considered as active S_{11} which includes S_{11} and S_{21}. Hence, realized gain can be rewritten in terms of active S_{11} (S_{11}^A),

$$G_r(\theta, \phi) = (1 - |S_{11}^A|^2)\, G(\theta, \phi) \tag{3.19}$$

Although $|S_{11}|$ at 3.6 GHz is below -15 dB in Figure 3.7, realized gains are not as desired seen in radiation pattern plots. It arises from coupling between the ports. When active S parameters are examined in Figure 3.13, it is observed that the coupling between the ports is evident. Active $|S_{11}|$ is affected by reflection from the other port via coupling. Hence, the main goal is to lower active $|S_{11}|$ as much as possible to have better realized gain by reducing the coupling. Simulated gain and realized gain values are listed in Table 3.1.

Table 3.1: Simulated Gain and Realized Gain Values of RCPA without Decoupling Network

Parameter	**Conical Beam (PD: 0°)**	**Broadside Beam (PD: 180°)**
Gain (dB)	6.5	7.2
Realized Gain (dB)	3.7	5.0

Here, active $|S_{11}|$ values are considerably poor, around 3-4 dB for two different phase differences. That results in increase in the difference between gain and realized gain. Thus, in following sections, decoupling network will be introduced and its effect on active S parameters and realized gain will be analyzed.

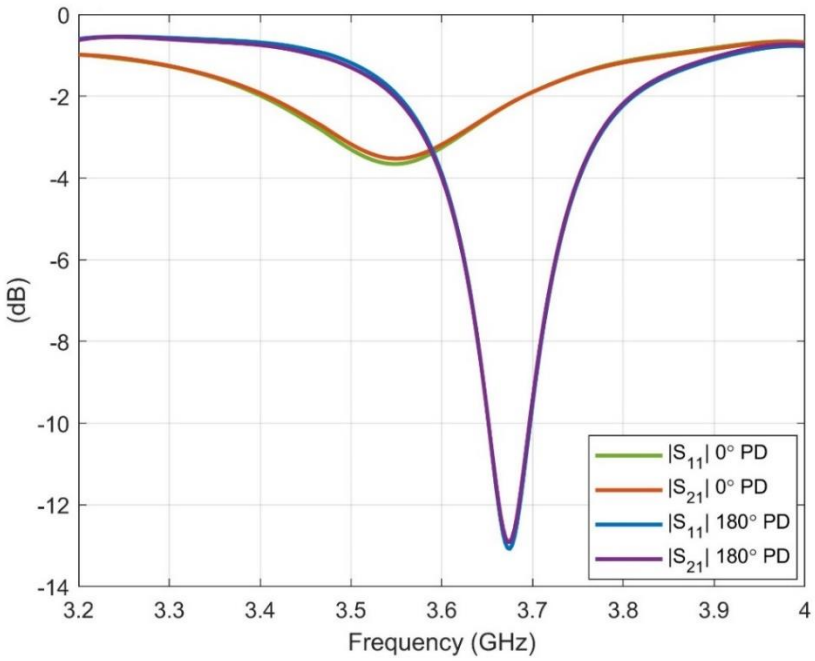

Figure 3.13: RCPA without Decoupling Network Active S Parameters

3.3 Design of RCPA with Inductive Decoupling Network

First method to decouple RCPA ports is designing and implementing inductive decoupling network. To follow the technique presented in Section 3.1, Y parameters of RCPA without decoupling network is exported from HFSS and imported to AWR for microwave circuit simulations. Utilization of AWR is critical in this phase because it reduces the simulation time compared to the full-wave simulation of antenna and decoupling network. As shown in Figure 3.14, in AWR model, transmission line sections with 50 Ω characteristic impedance are connected to the ports of the antenna. By using tune tool of AWR, the length of these transmission lines required to make real part of Y_{21}^{A} zero is found. First, real and imaginary parts of imported Y_{21}^{A} are plotted in Figure 3.15 to see the behaviour with respect to frequency.

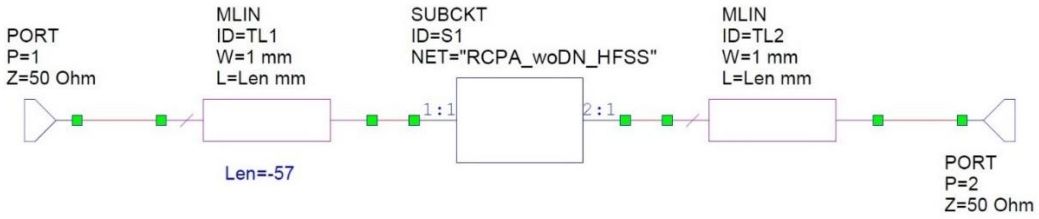

Figure 3.14: Circuit Diagram of RCPA Y Parameters with Transmission Lines

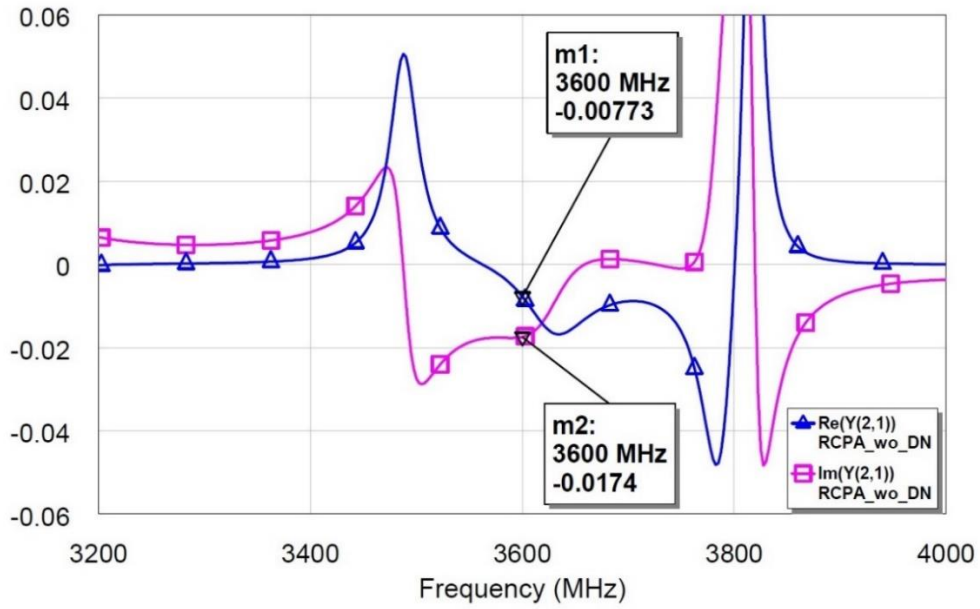

Figure 3.15: Y_{21}^{A} at the Ports of RCPA without Decoupling Network

As seen in Figure 3.15, real part of Y_{21}^{A} is not far from zero crossing. In fact, 4 mm away from the ports of RCPA, the first zero crossing is met. However, 4 mm is not sufficient to make room for the lumped element. For this reason, a larger distance for zero crossing is searched and 57 mm is found to be suitable to integrate the lumped element. Real and imaginary parts of Y_{21}^{A} 57 mm away from the ports of the antenna are presented in Figure 3.16. Note that the length of the transmission lines, 57 mm, is defined as a negative value in Figure 3.14 since its direction is from the antenna ports to apertures of the antenna.

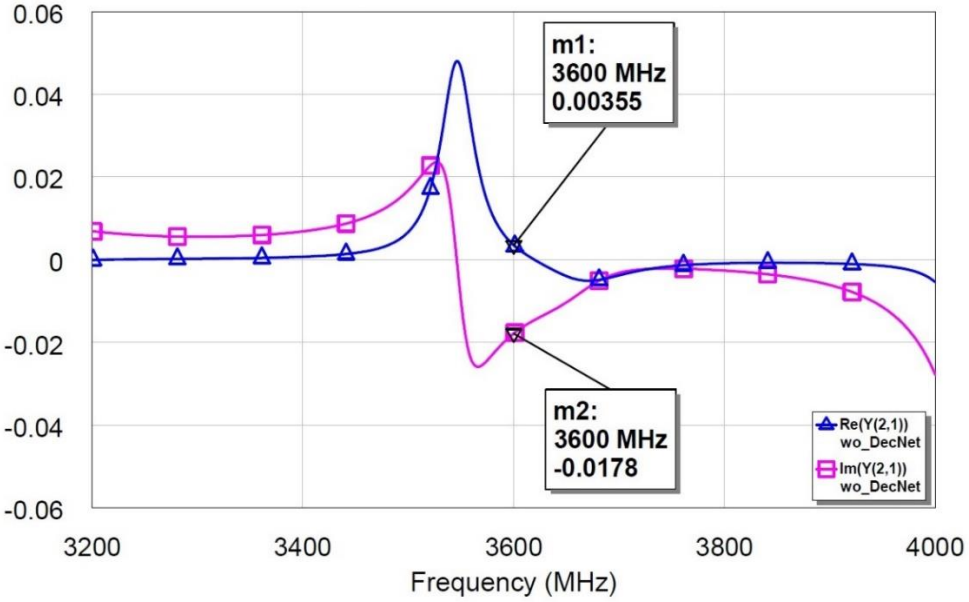

Figure 3.16: Y_{21}^{A}, 57 mm away from Ports of RCPA without Decoupling Network

Since the value of imaginary part of Y_{21}^{A} is negative, an inductor is presented to satisfy the second condition for decoupling. Before going into calculations of the inductance, admittance network of a purely imaginary lumped element illustrated in Figure 3.17 can be summarized as:

$$Y^{DN} = \begin{bmatrix} Y_{11}^{DN} & Y_{12}^{DN} \\ Y_{21}^{DN} & Y_{22}^{DN} \end{bmatrix} = \begin{bmatrix} jB & -jB \\ -jB & jB \end{bmatrix} \tag{3.20}$$

Derivation of Equation 3.20 is given in Appendix B.

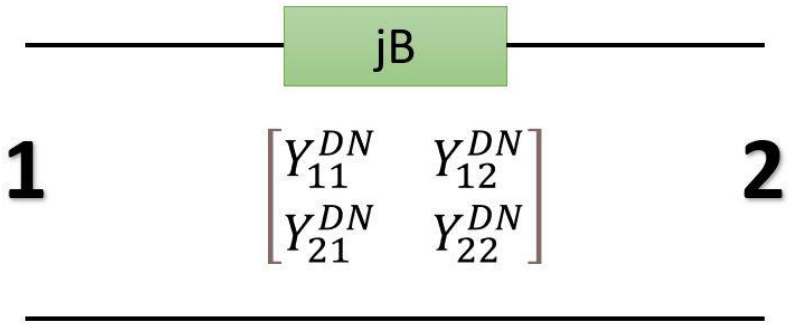

Figure 3.17: Admittance Network of a Purely Imaginary Lumped Element

Thus, Y_{21}^{DN} can be rewritten as

$$Y_{21}{}^{DN} = -jB \tag{3.21}$$

$$Im\{Y_{21}{}^{DN}\} = -B \tag{3.22}$$

To make the imaginary part of antenna and lumped element combination zero, susceptance of the lumped element can be found as

$$B = Im\{Y_{21}{}^{A}\} \tag{3.23}$$

Now considering an inductor, susceptance is calculated as

$$B = \frac{-1}{\omega L} \tag{3.24}$$

where $\omega = 2\pi f$ and L is the inductance

Hence, at 3.6 GHz, the inductance for decoupling network is

$$L = \frac{-1}{2\pi(3.6x10^{9})(-0.0178)} = 2.48\ nH \tag{3.25}$$

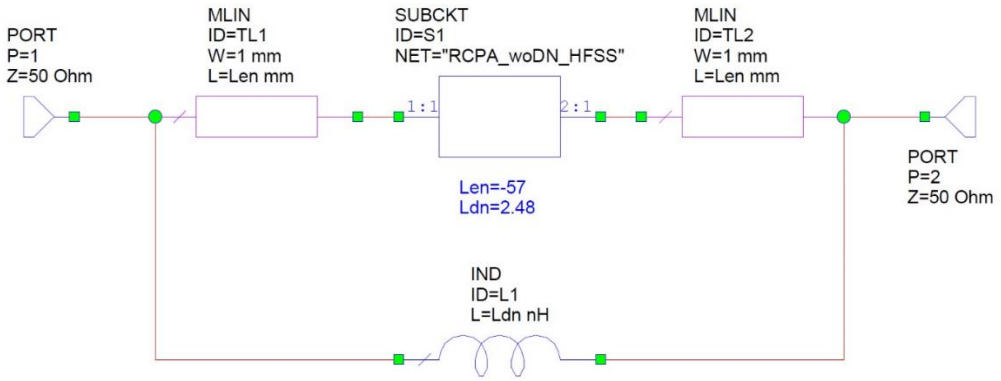

Figure 3.18: Circuit Diagram of RCPA with Inductive Decoupling Network

2.48 nH is added to the AWR model as shown in Figure 3.18 and simulation is run again. To verify the technique, it is better to check real and imaginary parts of Y_{21} first. Imaginary and real parts of Y_{21} are compared in Figure 3.19 and Figure 3.20, respectively. Pink trace belongs to RCPA without decoupling network and 57 mm away from antenna ports. Blue trace is the curve for 2.48 nH only and green trace is summation of them corresponding to RCPA with inductive decoupling network. Both conditions for decoupling are met as green traces go to zero around 3.6 GHz in Figure 3.19 and Figure 3.20. That leads to decrease in the value of $|S_{21}|$ plotted in Figure 3.21. Note that since real part of an ideal inductor is zero, blue curve in Figure 3.20 is a zero curve so pink and green traces overlap.

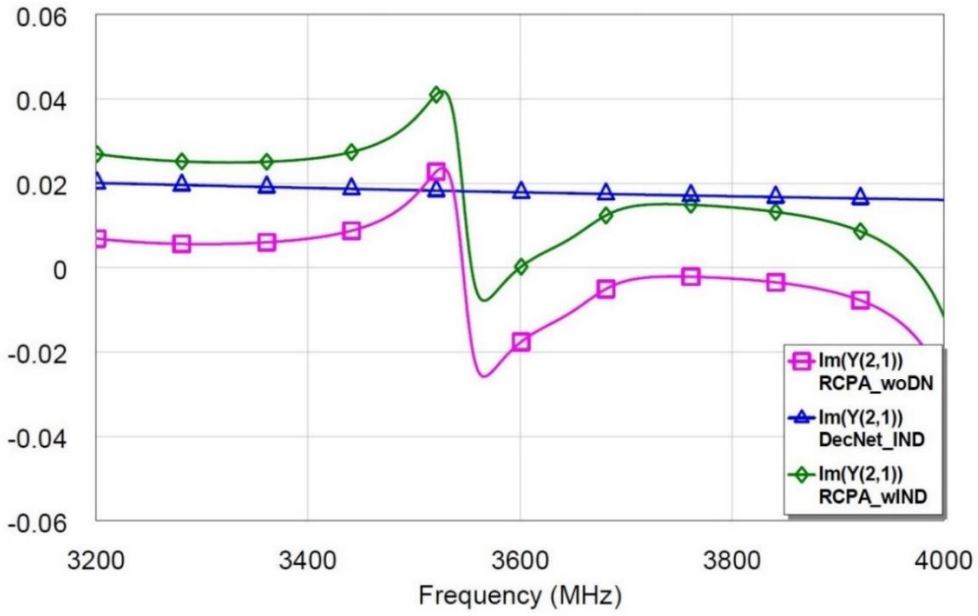

Figure 3.19: Comparison of Imaginary Parts of Y_{21} with Inductance

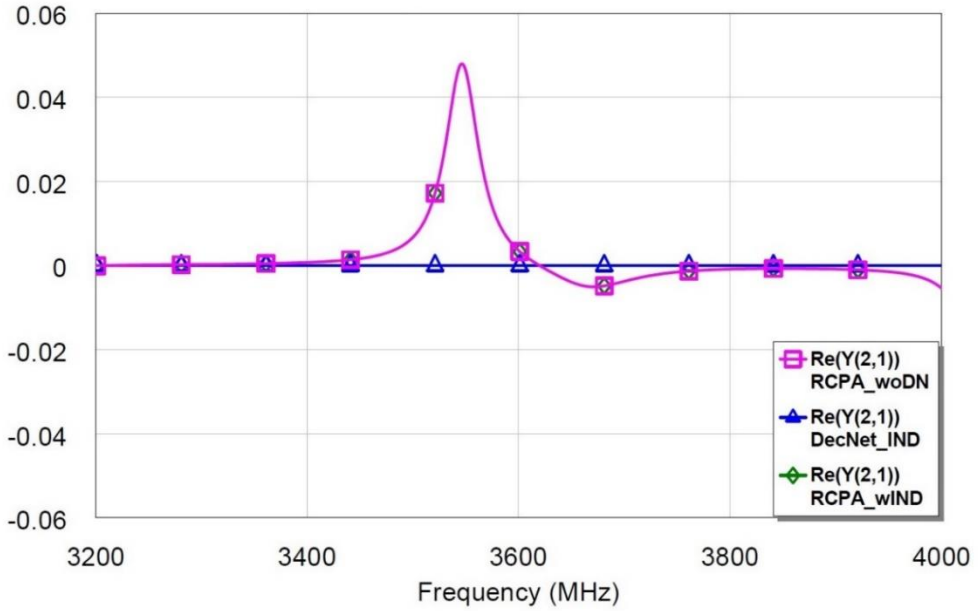

Figure 3.20: Comparison of Real Parts of $Y_{21}$with Inductance

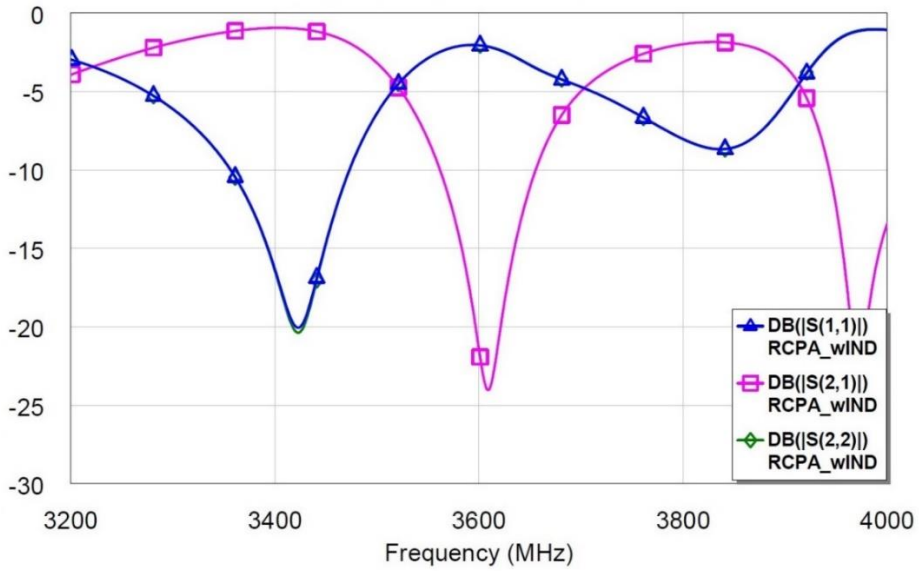

Figure 3.21: Simulated S Parameters of RCPA with 2.48 nH

Although Equation 3.25 gives us the exact value of inductance, this inductance will not be used since it is not available as a lumped component. The closest value to 2.48 nH is 2.2 nH inductor in Coilcraft 0603CS designer's kit which we own. Accordingly, simulation is rerun with 2.2 nH inductance and no major change is observed in S parameters as shown in Figure 3.23.

Moreover, one important thing to take into consideration is decoupling bandwidth. Looking back to Figure 3.19 and Figure 3.20, in the whole band, both real and imaginary parts of decoupling network are almost constant so they do not affect the overall bandwidth. On the other hand, antenna admittance varies rapidly around resonant frequency. Thus, decoupling bandwidth mainly depends on the antenna admittance characteristic. Here, 10 dB decoupling ($|S_{21}|$) bandwidth is 93 MHz for RCPA with 2.2 nH.

To sum up, inductive decoupling network is successfully designed and integrated to RCPA in circuit-based simulations in AWR. Then, HFSS simulation is performed to analyze the whole structure more rigorously. Decoupling inductor is placed between the feed lines shown with an arrow in Figure 3.22 and it is defined as lumped RLC boundary in HFSS. Its position is optimized as 57 mm away from the ports as designed in AWR. HFSS simulation results are compared to AWR results in Figure 3.23. It can be observed that for this structure, circuit simulator AWR performs as good as the full-wave simulator HFSS.

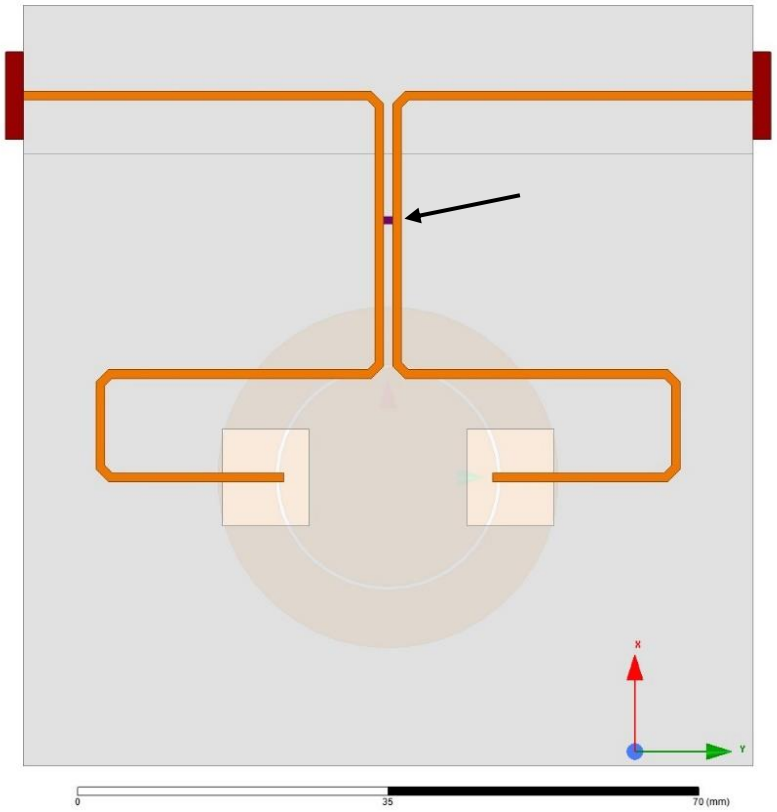

Figure 3.22: HFSS Model of RCPA with Inductor

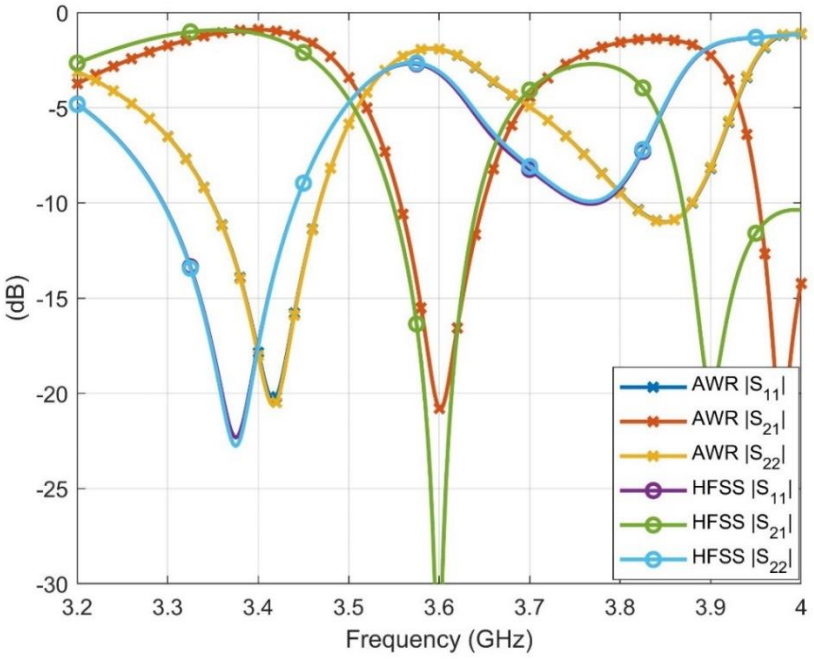

Figure 3.23: Simulated S Parameters of RCPA with 2.2 nH

Besides, effect of inductance on decoupling is analyzed with a parametric sweep in HFSS. As seen in Figure 3.24, inductance is not that much effective on decoupling since sweeping inductance from 1.9 nH to 2.5 nH does not change susceptance significantly and the imaginary part of Y_{21}^{A} is rapidly changing in the vicinity of resonant frequency as shown in Figure 3.19. This result demonstrates that inductive decoupling network is insensitive to inductance value for this Y_{21}^{A} characteristics. This is an important conclusion when considering decoupling network design with a lumped component.

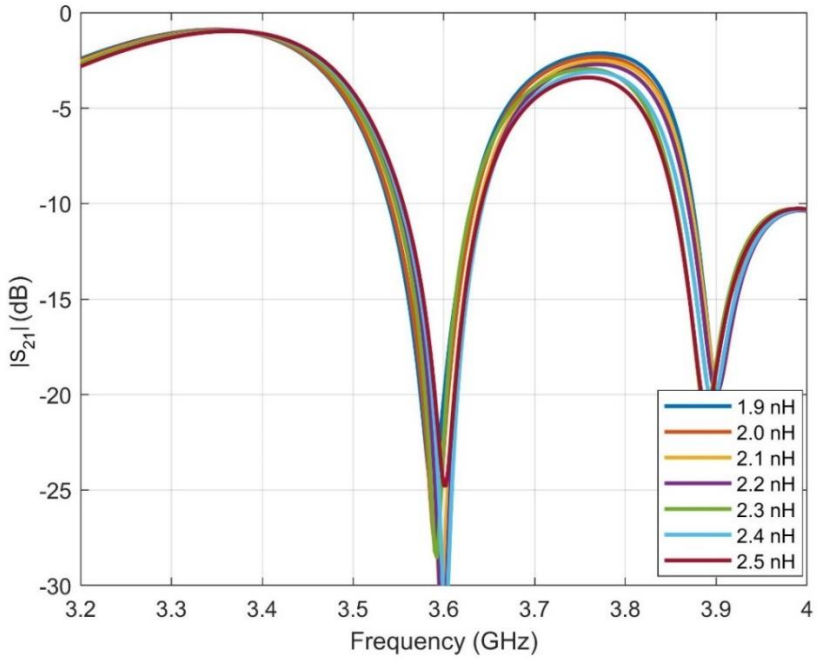

Figure 3.24: $|S_{21}|$, Inductance Sweep

After decoupling, last part of the procedure is the design of a matching network. As seen in Figure 3.23, values of $|S_{11}|$ and $|S_{22}|$ at 3.6 GHz are pretty bad so we need to reduce them to below -10 dB for a better return loss characteristic. For matching network, single stub matching approach is followed because of easier implementation. S parameters of RCPA with inductor are exported from HFSS and imported to AWR again to find stub length and stub distance. Matching circuitry constructed in Figure 3.25 is optimized with optimization tool of AWR. Stub length and stub distance away from the inductor are found as 8.4 mm and 24.6 mm, respectively. S parameters of matched and decoupled RCPA with inductor are given in Figure 3.27.

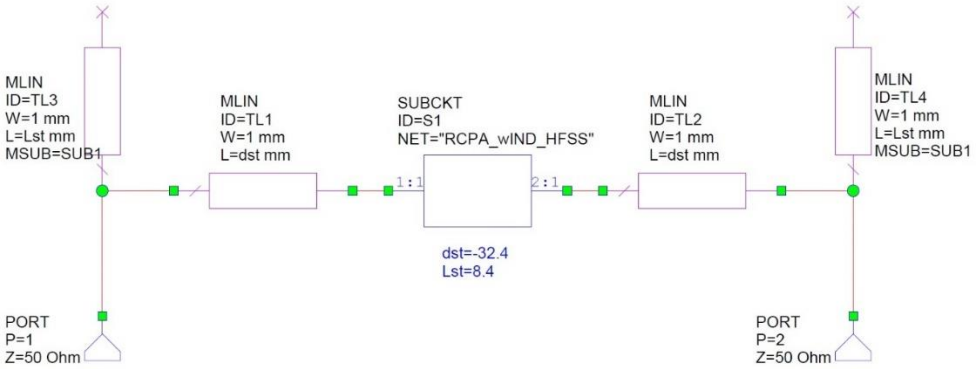

Figure 3.25: Circuit Diagram of Matched and Decoupled RCPA with 2.2 nH

Finally, the results are also verified through HFSS simulation with the structure shown in Figure 3.26. Stub length and stub distance are optimized with parametric sweep and optimized values are marked on the figure. As seen in Figure 3.27, S parameters by HFSS are in accord with S parameters by AWR.

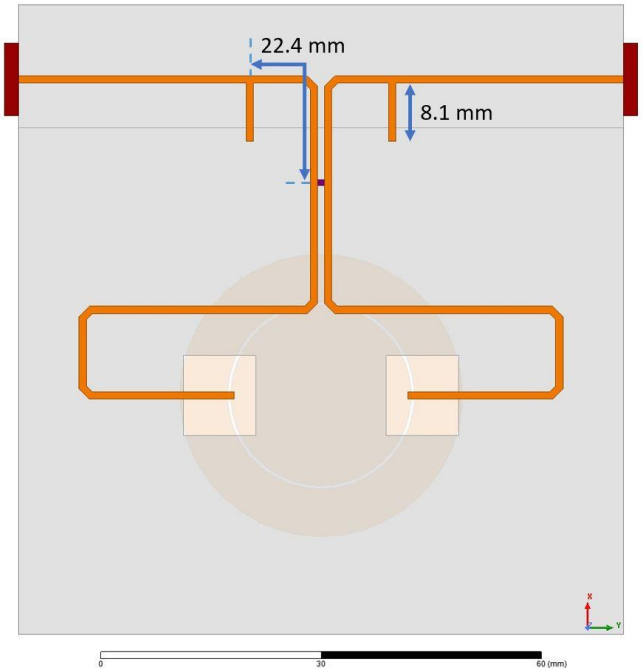

Figure 3.26: HFSS Model of RCPA with Inductor and Stubs

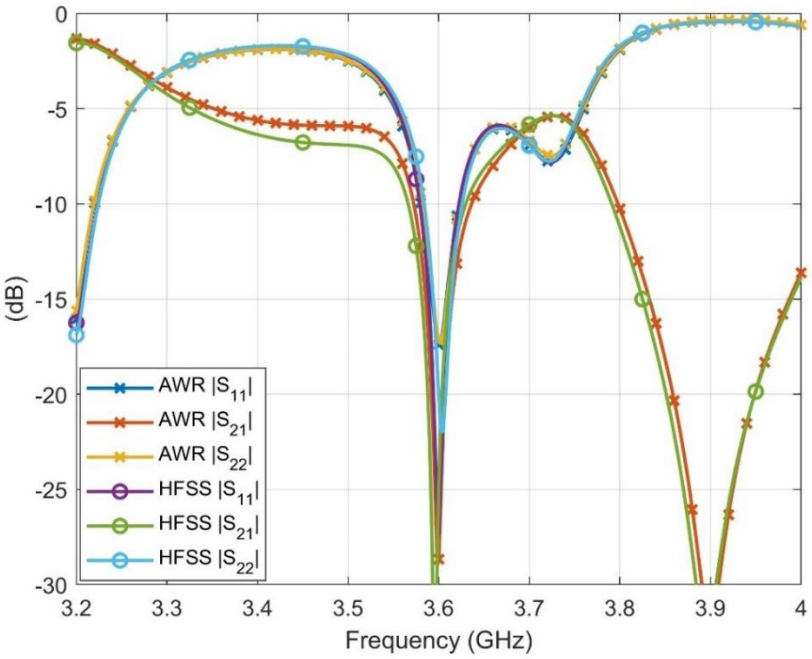

Figure 3.27: Simulated S Parameters of Matched and Decoupled RCPA with 2.2 nH

Before going into details of far field results, we should also examine the bandwidths. 10 dB decoupling ($|S_{21}|$) and matching ($|S_{11}|$) bandwidths are listed in Table 3.2. In the table, overall bandwidth corresponds to the bandwidth where both together $|S_{11}|$ and $|S_{21}|$ are below -10 dB. It is clear that all bandwidths are quite narrow around 3.6 GHz. The reason for narrowband decoupling is rapidly varying antenna admittance as defined earlier. Not only decoupling but also matching bandwidth is dominated by the antenna characteristics. $|S_{11}|$ of decoupled, but not matched, RCPA is shown on Smith Chart in Figure 3.28. The values at the close frequencies are far away from each other. As an example, three close frequencies (3500 MHz, 3600 MHz and 3700 MHz) are marked on the figure. As it is well known, small loops in Smith Chart can be matched but this structure constructs a large loop. Consequently, with those values, it is not possible to match this structure in a wide band.

Table 3.2: Simulated Bandwidths of Matched and Decoupled (IND) RCPA

Bandwidth	AWR	HFSS
10 dB Decoupling (MHz)	64	60
10 dB Matching (MHz)	42	40
10 dB Overall (MHz)	42	40

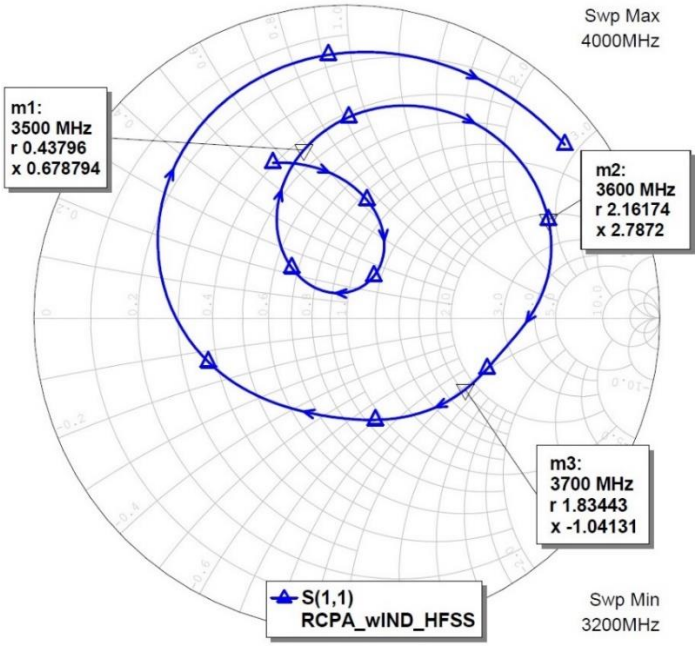

Figure 3.28: $|S_{11}|$ of Inductive Decoupled RCPA Before Matching on Smith Chart

Gain and realized gain values of decoupled RCPA with 2.2 nH are plotted in Figure 3.29 to 3.32. The first thing to notice is that gain and realized gain patterns almost overlap in each plot whereas they were different without decoupling network. Yet, shapes of the patterns are retained so it can be concluded that the addition of inductive decoupling network does not affect the radiation pattern. The enhancement can be seen in decoupled gain and realized gain values listed in Table 3.3. Accordingly, the difference between gain and realized gain is reduced to 0.1 dB for

both beams. Comparing Table 3.1 and Table 3.3, realized gains are enhanced 2.9 dB in conical beam and 1.8 dB in broadside beam.

As explained before, the improvement in realized gains is originated from the improvement in active $|S_{11}|$ as illustrated in Figure 3.33.

Table 3.3: Simulated Gain and Realized Gain Values of RCPA with Inductive Decoupling Network

Parameter	**Conical Beam (PD: 0°)**	**Broadside Beam (PD: 180°)**
Gain (dB)	6.7	6.9
Realized Gain (dB)	6.6	6.8

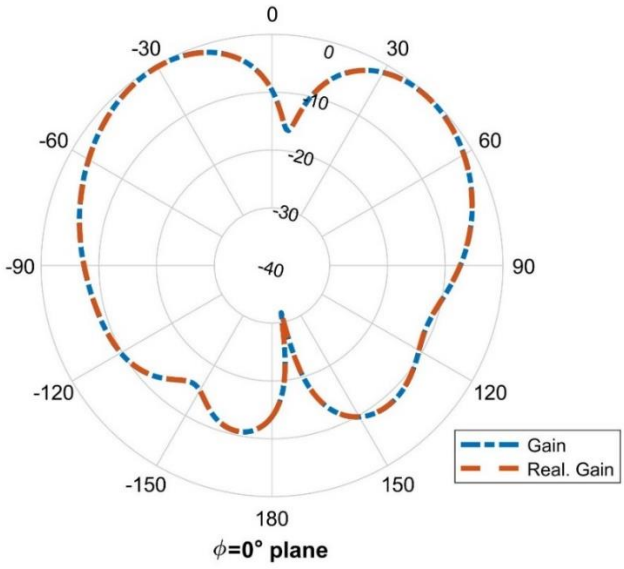

Figure 3.29: Matched and Inductive Decoupled RCPA Radiation Patterns, Conical Beam (PD: 0°) at $\phi = 0°$ Plane

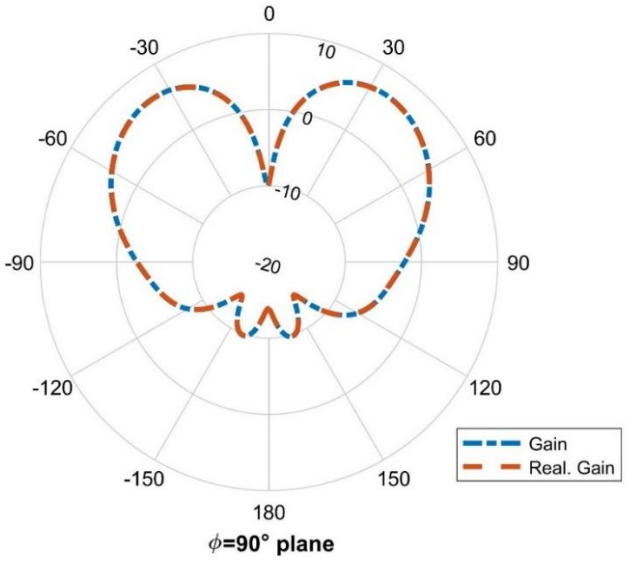

Figure 3.30: Matched and Inductive Decoupled RCPA Radiation Patterns, Conical Beam (PD: 0°) at $\phi = 90°$ Plane

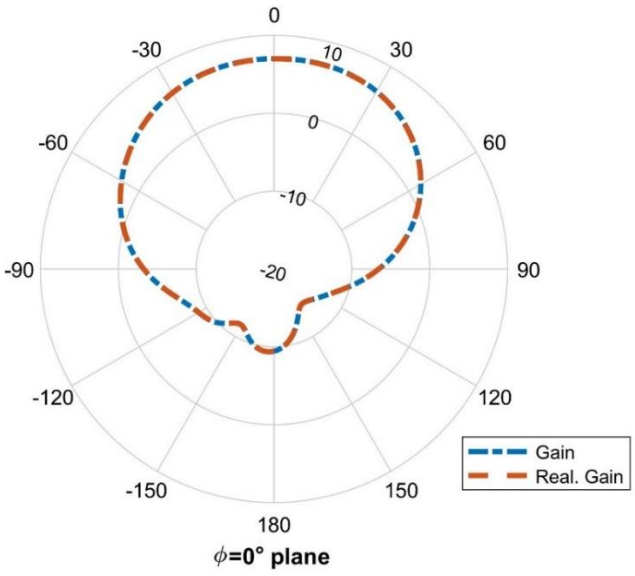

Figure 3.31: Matched and Inductive Decoupled RCPA Radiation Patterns, Broadside Beam (PD: 180°) at $\phi = 0°$ Plane

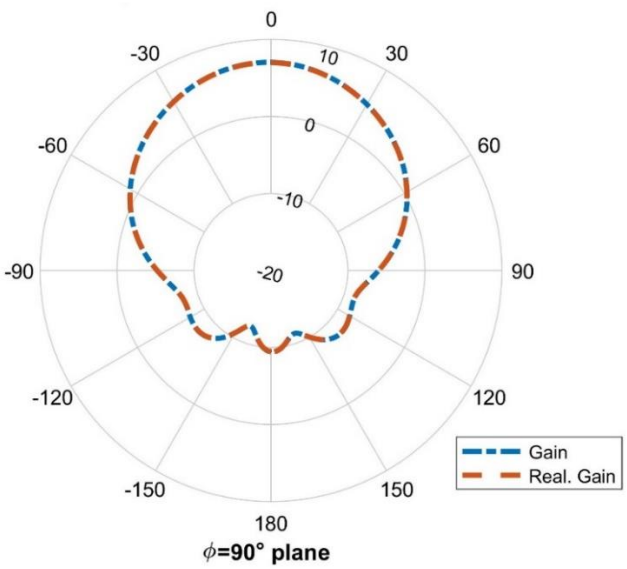

Figure 3.32: Matched and Inductive Decoupled RCPA Radiation Patterns, Broadside Beam (PD: 180°) at $\phi = 90°$ Plane

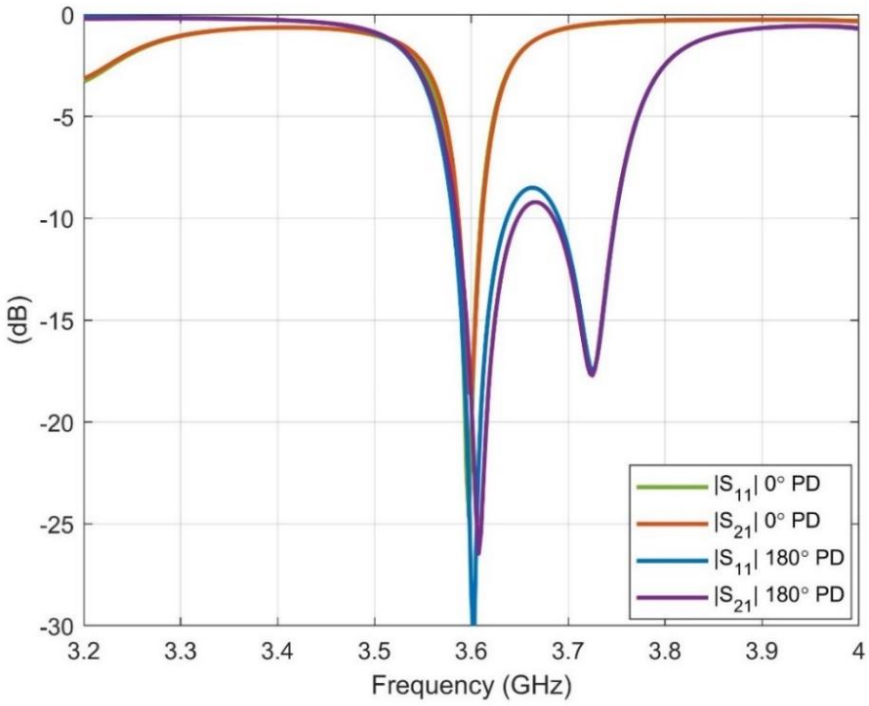

Figure 3.33: Simulated Active S Parameters of Matched and Inductive Decoupled RCPA

3.4 Design of RCPA with Capacitive Decoupling Network

Second method to decouple RCPA ports is designing and implementing capacitive decoupling network. By adopting the technique in Section 3.1, Y parameters of RCPA without decoupling network is exported from HFSS and imported to AWR for microwave circuit simulations. In this section, same procedures in Section 3.3 are followed with a capacitor instead of an inductor.

The distance away from the ports is set to 66 mm so that real part of Y_{21}^{A} goes to zero as shown in Figure 3.34.

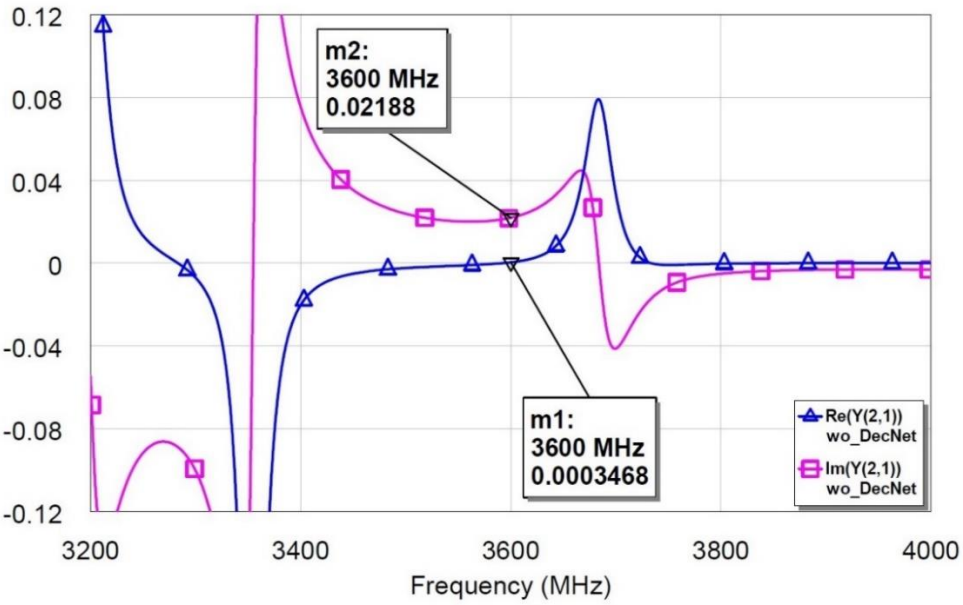

Figure 3.34: Y_{21}^{A}, 66 mm away from Ports of RCPA without Decoupling Network

Susceptance of a capacitor is calculated as

$$B = \omega C \tag{3.26}$$

where $\omega = 2\pi f$ and C is the capacitance

Hence, the capacitance for decoupling network can be calculated as follows to eliminate the imaginary part of Y_{21}^{A} at 3.6 GHz,

$$C = \frac{0.0219}{2\pi(3.6x10^{9})} = 0.97\ pF \tag{3.27}$$

As a realizable value, 1 pF is added to the circuitry as shown in Figure 3.18 instead of inductor and simulation is run again. To verify the technique, it is better to check real and imaginary parts of Y_{21} first. Imaginary and real parts of Y_{21} are compared in Figure 3.35 and Figure 3.36, respectively. Pink trace belongs to RCPA without decoupling network and 66 mm away from the ports. Blue trace is the curve of 1 pF and green trace is summation of them corresponding to RCPA with capacitive decoupling network. Both conditions for decoupling are met as green traces go to zero around 3.6 GHz in Figure 3.35 and Figure 3.36. That leads to reduction in the value of $|S_{21}|$ plotted in Figure 3.37.

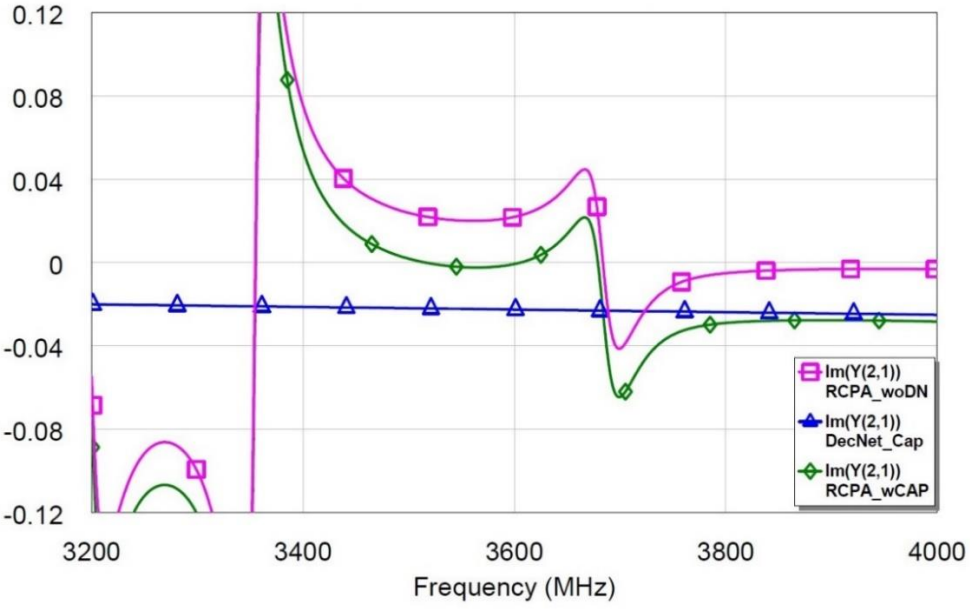

Figure 3.35: Comparison of Imaginary Parts of Y_{21} with Capacitance

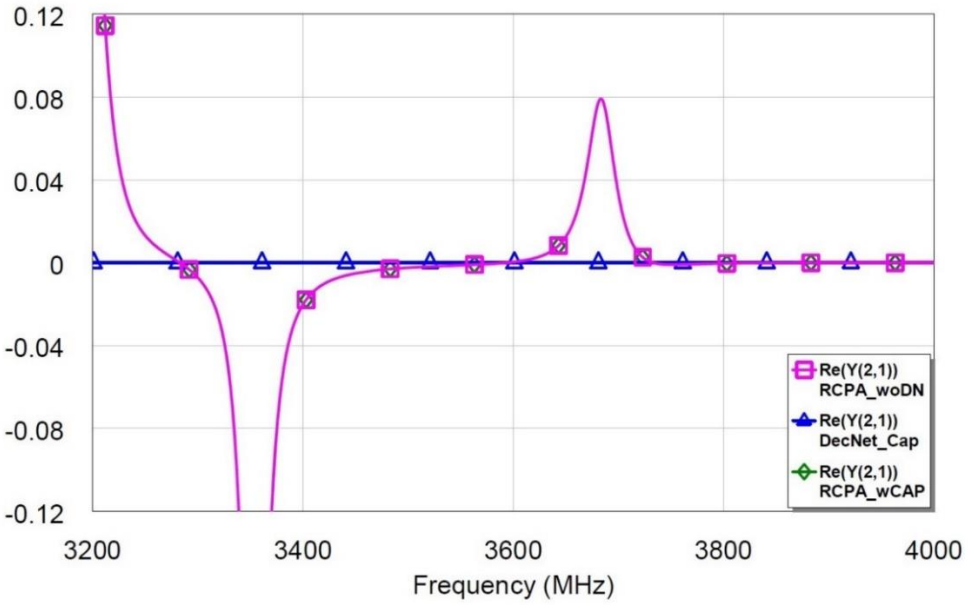

Figure 3.36: Comparison of Real Parts of Y_{21} with Capacitance

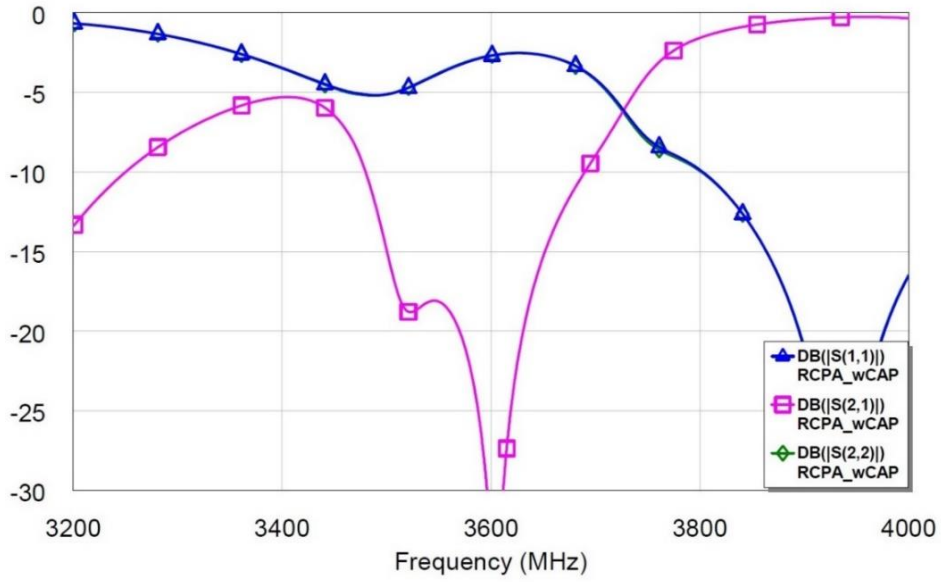

Figure 3.37: Simulated S Parameters of RCPA with 1 pF

Capacitive decoupling network is successfully designed and integrated to RCPA in circuit-based simulations in AWR and then, HFSS simulation is run for more realistic results. A parametric sweep over capacitance value is carried out and corresponding $|S_{21}|$ results are shown in Figure 3.38. It is realized that 0.8 pF provides wider decoupling bandwidth then 1.0 pF so the capacitance of decoupling network is updated as 0.8 pF at this stage. Besides, it is worth pointing out that capacitive decoupling network has wider decoupling bandwidth then inductive decoupling network since imaginary part of Y_{21}^{A} is constant in a wider frequency range around the resonant frequency in capacitive case.

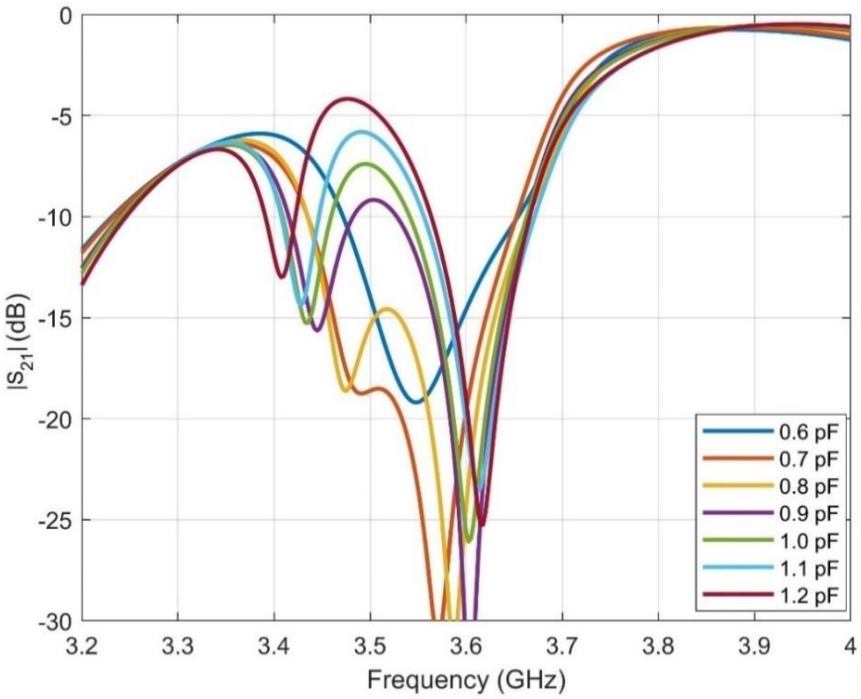

Figure 3.38: $|S_{21}|$, Capacitance Sweep

S parameter results with 0.8 pF are given in Figure 3.39 clearly. As stated above, this configuration has a wider decoupling bandwidth due to almost constant Y_{21}^{A} values around 3.6 GHz and also, effect of a lumped element on Y_{21} is minimal. Here, 10 dB decoupling($|S_{21}|$) bandwidth is 194 MHz for RCPA with 0.8 pF.

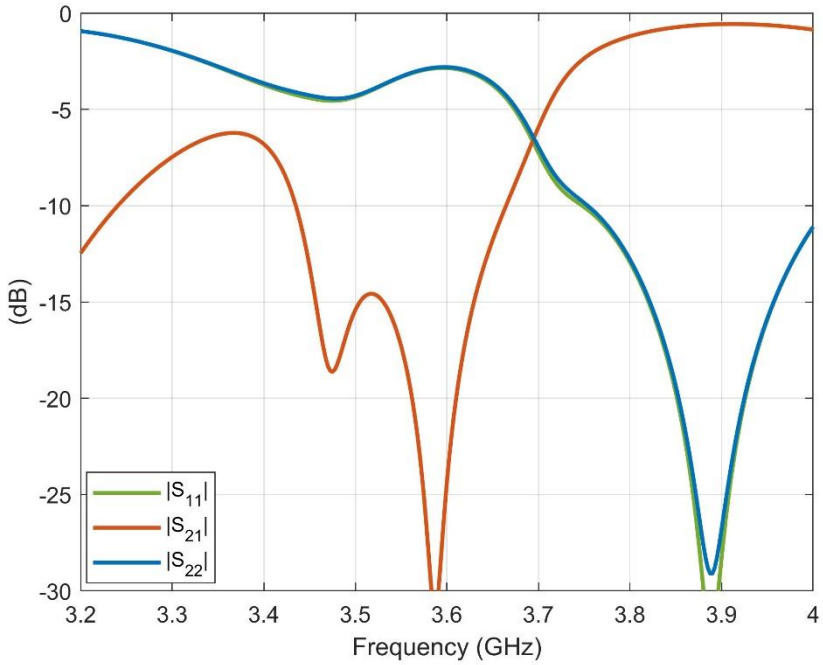

Figure 3.39: Simulated S Parameters of RCPA with 0.8 pF in HFSS

After decoupling, last part of the procedure is the design of a matching network. For matching network, single stub matching approach is followed. S parameters of RCPA with capacitor are exported from HFSS and they are imported to AWR again to find stub length and stub distance easily. Matching circuitry constructed in Figure 3.25 is optimized with optimization tool of AWR. Stub length and stub distance are found as 9.1 mm and 33.1 mm away from the capacitor, respectively. S parameters of matched and decoupled with capacitor RCPA are given in Figure 3.41.

Finally, it is also verified with HFSS simulation. The model is modified by adding open ended stubs as shown in Figure 3.40. Stub length and stub distance are optimized with parametric sweep and optimized values are marked on the figure. As seen in Figure 3.41, S parameters obtained by HFSS agree with S parameters obtained by AWR.

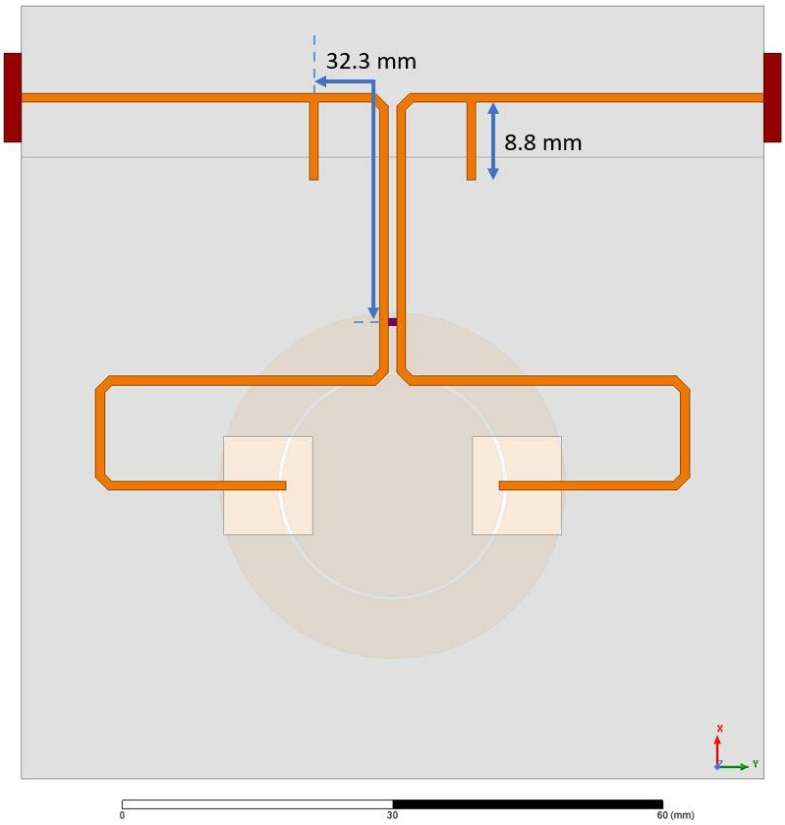

Figure 3.40: HFSS Model of RCPA with Capacitor and Stubs

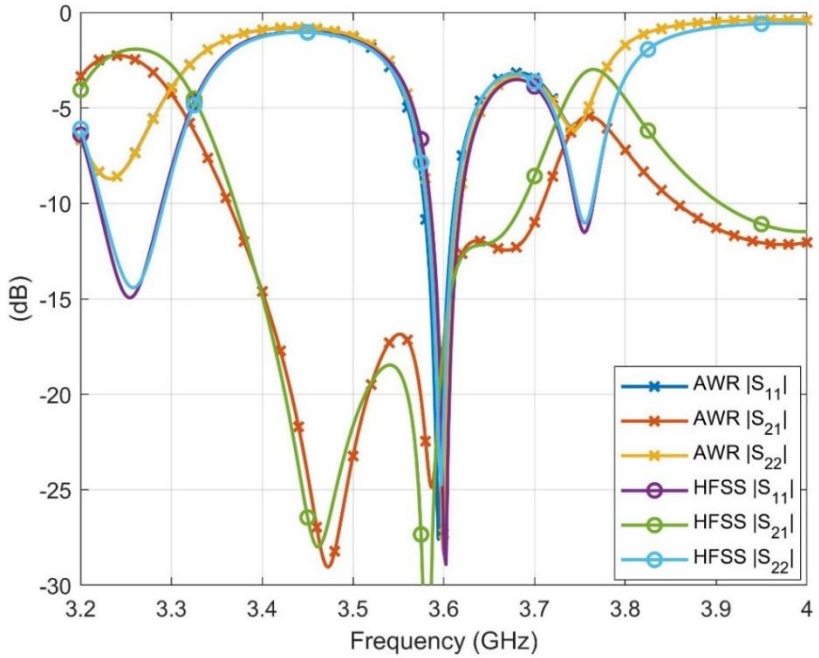

Figure 3.41: Simulated S Parameters of Matched and Decoupled RCPA with 0.8 pF

10 dB decoupling ($|S_{21}|$) and matching ($|S_{11}|$) bandwidths are listed in Table 3.4. Even though decoupling bandwidth is wider, matching bandwidth limits the overall bandwidth. The reason for narrow matching bandwidth can be deduced by checking $|S_{11}|$ of decoupled, but not matched, RCPA shown on Smith Chart in Figure 3.42. Same narrowband matching situation is valid with capacitive decoupling network as well. Hence, it is not possible to match this structure in a wide band. Also, it is noticed that matching bandwidth in HFSS simulation is wider which might be due to better modeling in HFSS. Some parasitic effects that are not considered in equivalent circuit based AWR simulator may be the cause of larger bandwidth observed in full-wave simulator HFSS.

Table 3.4: Simulated Bandwidths of Matched and Decoupled (CAP) RCPA

Bandwidth	AWR	HFSS
10 dB Decoupling (MHz)	346	317
10 dB Matching (MHz)	34	70
10 dB Overall (MHz)	34	70

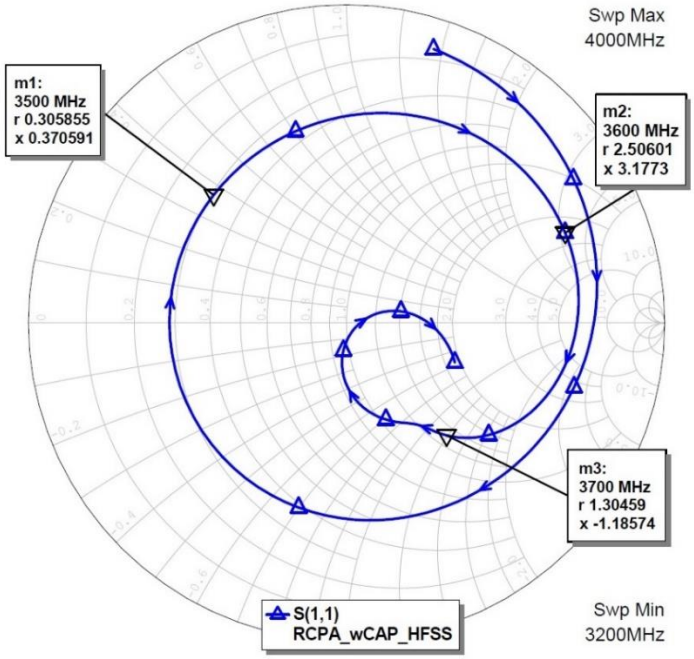

Figure 3.42: $|S_{11}|$ of Capacitive Decoupled RCPA Before Matching on Smith Chart

Gain and realized gain values of decoupled RCPA with 0.8 pF are plotted in Figure 3.43 to 3.46. As in far field results with inductive decoupling, gain and realized gain patterns almost overlap in each plot whereas they were different without decoupling network. Yet, shapes of the patterns are retained so it can be concluded that addition of capacitive decoupling network does not distort the radiation pattern. The improvement can be seen in decoupled gain and realized gain values listed in Table 3.5. Accordingly, the difference between gain and realized gain is reduced to 0.1 dB

for both beams. Comparing Table 3.1 and Table 3.5, realized gains are enhanced as 3.1 dB in conical beam and 2.7 dB in broadside beam.

As stated before, the improvement in realized gains is originated from the improvement in active $|S_{11}|$ as illustrated in Figure 3.47.

Table 3.5: Simulated Gain and Realized Gain Values of RCPA with Capacitive Decoupling Network

Parameter	**Conical Beam (PD: 0°)**	**Broadside Beam (PD: 180°)**
Gain (dB)	6.9	7.8
Realized Gain (dB)	6.8	7.7

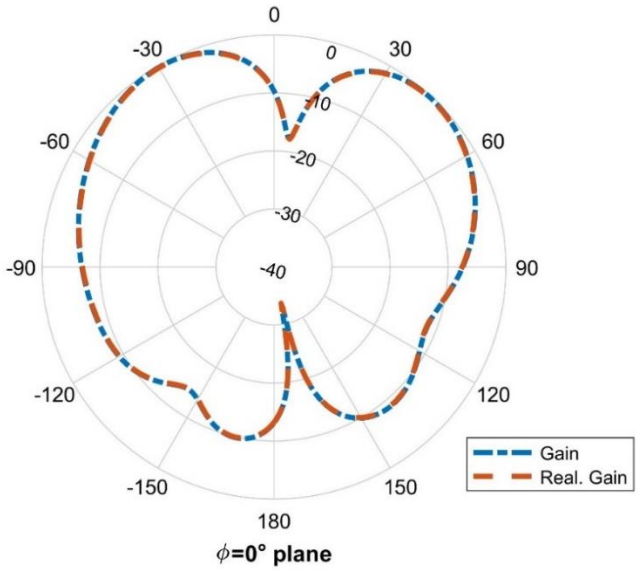

Figure 3.43: Matched and Capacitive Decoupled RCPA Radiation Patterns, Conical Beam (PD: 0°) at $\phi = 0°$ Plane

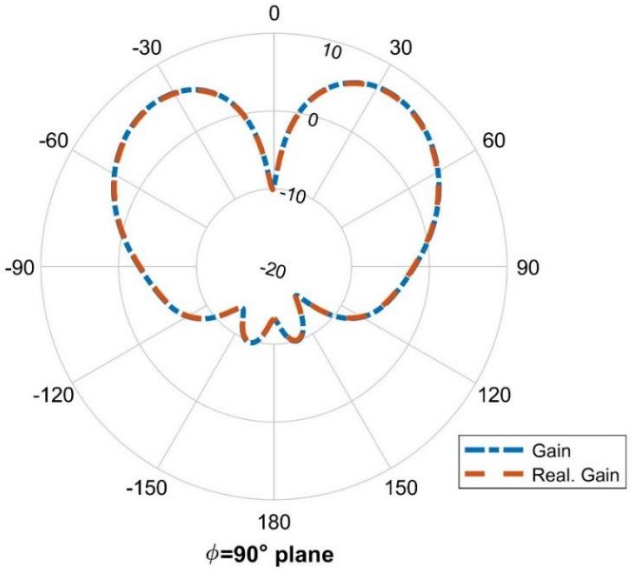

Figure 3.44: Matched and Capacitive Decoupled RCPA Radiation Patterns, Conical Beam (PD: 0°) at $\phi = 90°$ Plane

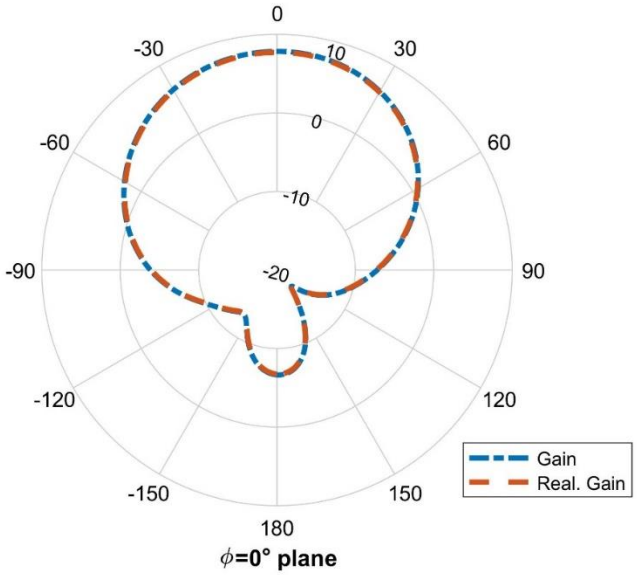

Figure 3.45: Matched and Capacitive Decoupled RCPA Radiation Patterns, Broadside Beam (PD: 180°) at $\phi = 0°$ Plane

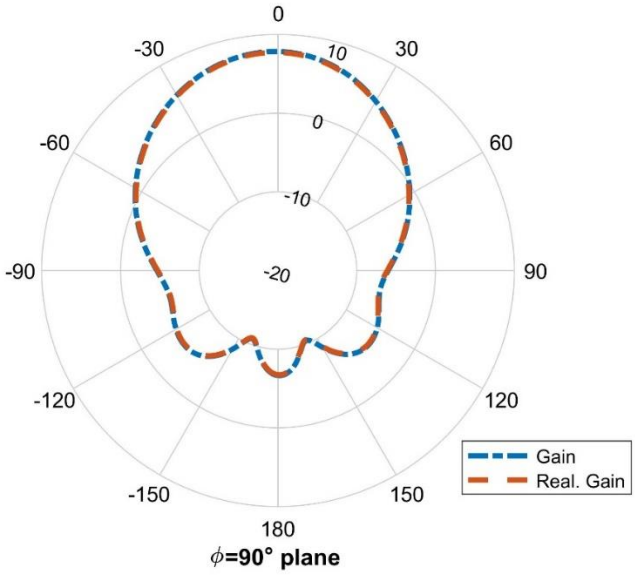

Figure 3.46: Matched and Capacitive Decoupled RCPA Radiation Patterns, Broadside Beam (PD: 180°) at $\phi = 90°$ Plane

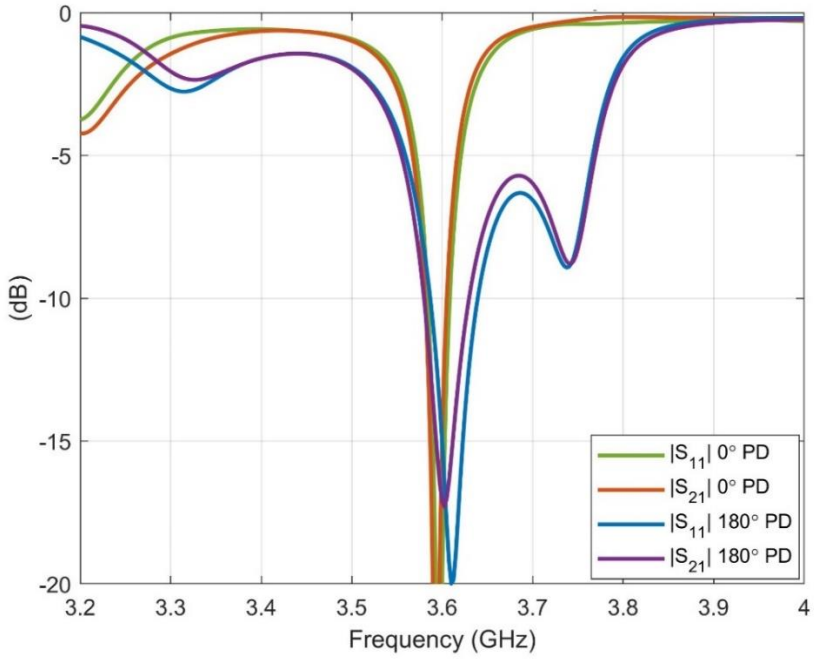

Figure 3.47: Simulated Active S Parameters of Matched and Capacitive Decoupled RCPA

CHAPTER 4

FABRICATION AND MEASUREMENTS OF RCPA WITH&WITHOUT DECOUPLING NETWORK

In this chapter, first, fabrication procedures and fabrication related issues are explained in detail. Then, inductive and capacitive decoupling networks are implemented to manufactured RCPA. Before and after decoupling network, S parameters and radiation patterns of RCPA are measured. Measurement results are compared and the enhancements in the gain values are discussed.

4.1 First Version RCPA

4.1.1 Fabrication

As is known, aperture coupled RCPA consists of two substrates: first one contains the antenna (ring and circular patch) and second one contains the feed lines and the ground plane. To construct the whole structure, two boards are needed to be fabricated. Therefore, drawings of aperture coupled RCPA with the parameters listed in Table 2.1 and Table 2.2 are imported to media of LPKF ProtoMat H100 and two different boards are fabricated. Rear and front sides of produced boards are exhibited in Figure 4.1. In the figure, upper boards are antenna boards and lower boards are feed boards.

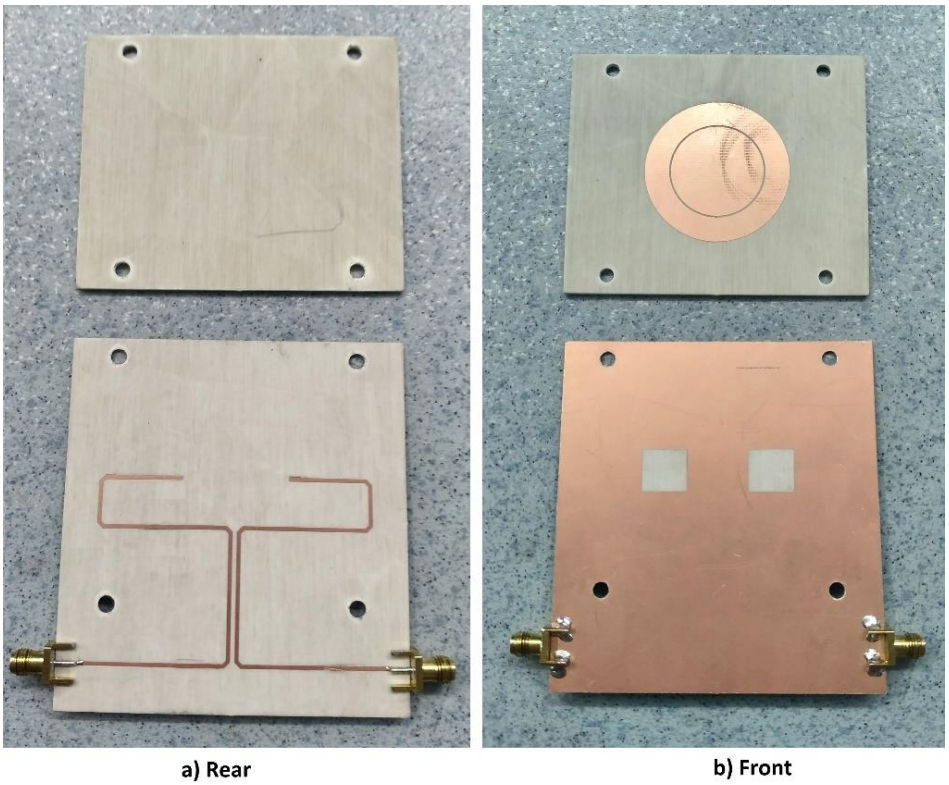

Figure 4.1: Rear and Front Views of Fabricated Boards

Fabrication process is comprised of mainly two procedures: etching by LPKF and peeling by hand. Following places are etched by LPKF:

- the gap between ring and circular patch
- around the circular patch
- around the feed lines
- edges of the apertures

Following places are peeled by hand:

- outside the ring
- whole bottom of the antenna board
- outside the feed lines
- inside the apertures

Apart from etching and peeling, holes are drilled for screws. The next step is to attach the boards to form overall antenna structure. To do so, aperture side (front side) of the feed board and blank side (rear side) of the antenna board are stuck to each other with plastic screws as can be seen in Figure 4.2. Material of the screws is chosen as plastic deliberately not to affect radiation characteristics of the antenna. Moreover, edge mount SMA connectors are soldered to feed lines as shown in Figure 4.1 and Figure 4.2. Feeds are located on y axis which is shown in Figure 4.2. For the last step, two copper sided substrate, as a ground plate, which has the same dimensions with the feed substrate is placed 25 mm away from the feed substrate as given in Figure 4.3 in order to suppress back lobe radiation. 25 mm is feasible distance which can be satisfied by plastic spacers in the laboratory.

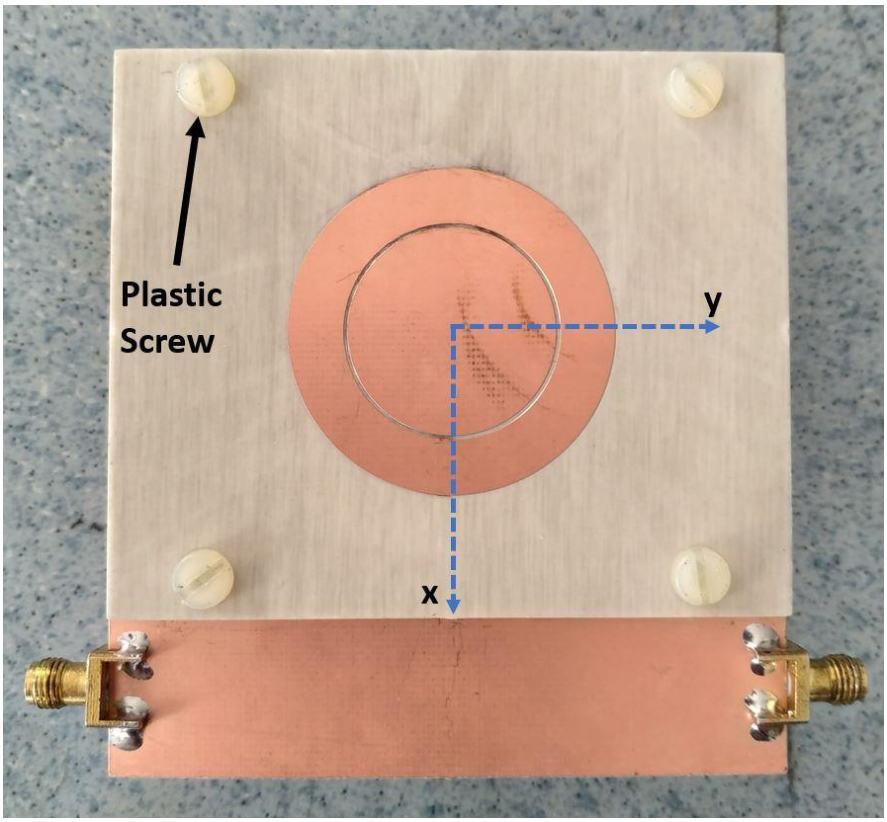

Figure 4.2: Bonding Boards with Screws

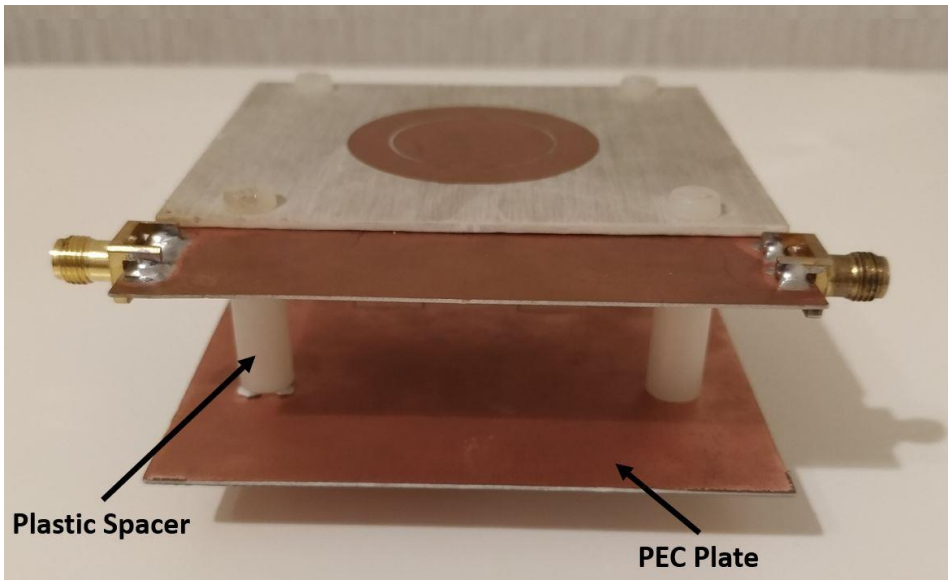

Figure 4.3: Addition of PEC Plate to RCPA Boards

4.1.2 Measurement

Constructed aperture coupled RCPA is connected to the ports of HP Agilent Keysight 8720D Network Analyzer to measure S parameters. In the first measurement, it is realized that resonant frequency is shifted to higher frequencies, to around 3.85 GHz. For debugging, the screws are controlled and it is observed that by squeezing the screws, resonant frequency shifts to lower frequencies, to around 3.73 GHz shown in Figure 4.4. More squeezing does not help us to achieve the resonance at 3.6 GHz.

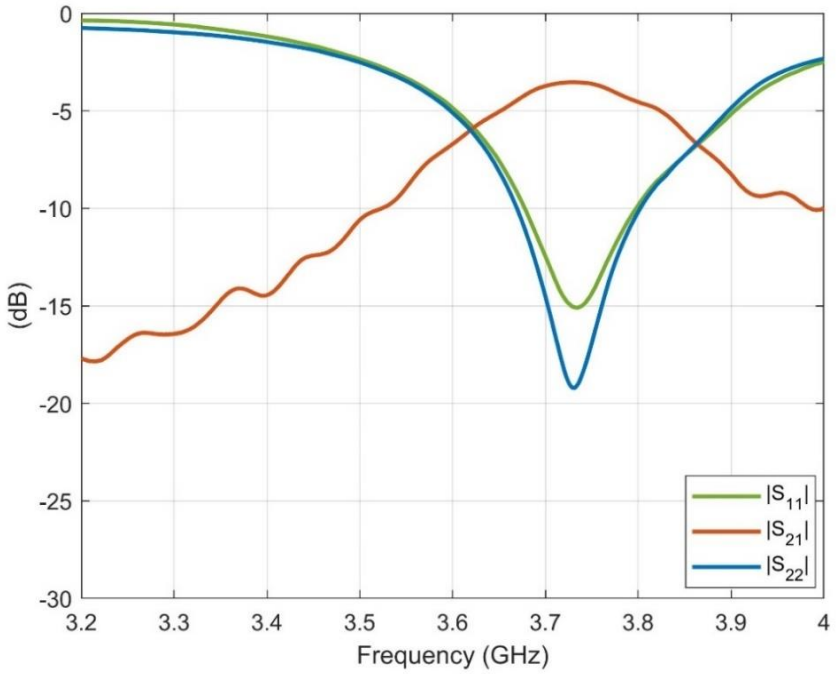

Figure 4.4: Measured S Parameters of First Version RCPA

One can deduce that air gap between two substrates can be changed by squeezing the screws and this change directly affects the resonant frequency. No matter how good substrates are stuck to each other by hand, there is always an air gap in between because it is not possible to bond them perfectly (zero air gap) by hand. To inspect the effect of air gap, a new HFSS simulation is run. As understood from Figure 4.5, increasing air gap between the substrates shifts the resonant frequency to the right (higher frequencies). Thus, S parameters of first version RCPA shown in Figure 4.4 can be considered as normal.

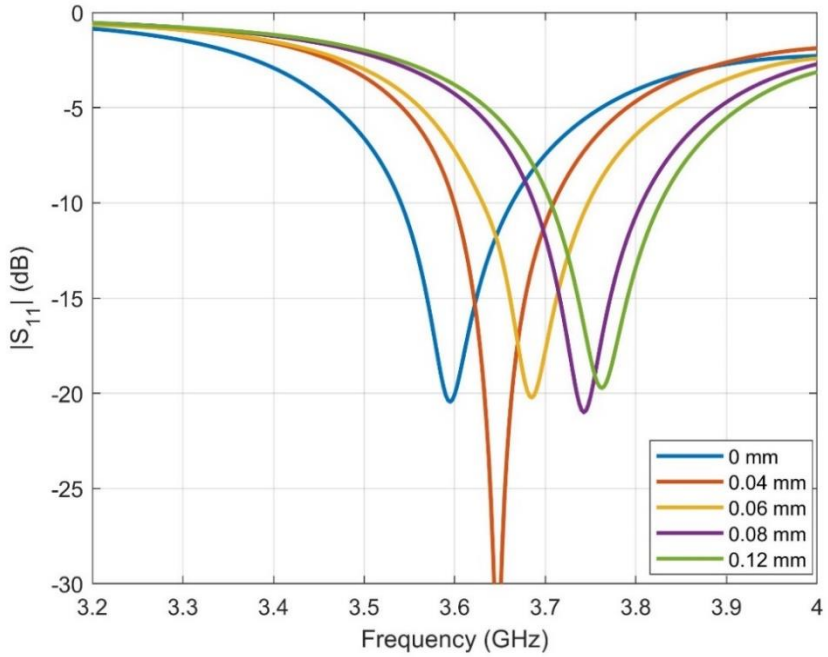

Figure 4.5: $|S_{11}|$, Air Gap Sweep

4.2 Second Version RCPA

4.2.1 Redesign and Fabrication

As explained above, effect of air gap during manufacturing is inevitable so it is better to update the antenna parameters to have the resonance at desired frequency which is 3.6 GHz. It is assumed that air gap is 0.08 mm due to resonance around 3.74 GHz seen in Figure 4.5. Therefore, RCPA is redesigned by considering 0.08 mm air gap. In this part of the study, separation between ring and circular patch, and the ratio of outer ring radius to inner ring radius are preserved.

The aim is to lower resonant frequency when 0.08 mm air gap is present. The first thing to do is enlarging the antenna element dimensions since operating frequency and antenna dimensions are inversely proportional. Therefore, larger circular patch radius gives us lower resonant frequency. That is studied in Figure 4.6 by sweeping circular patch radius.

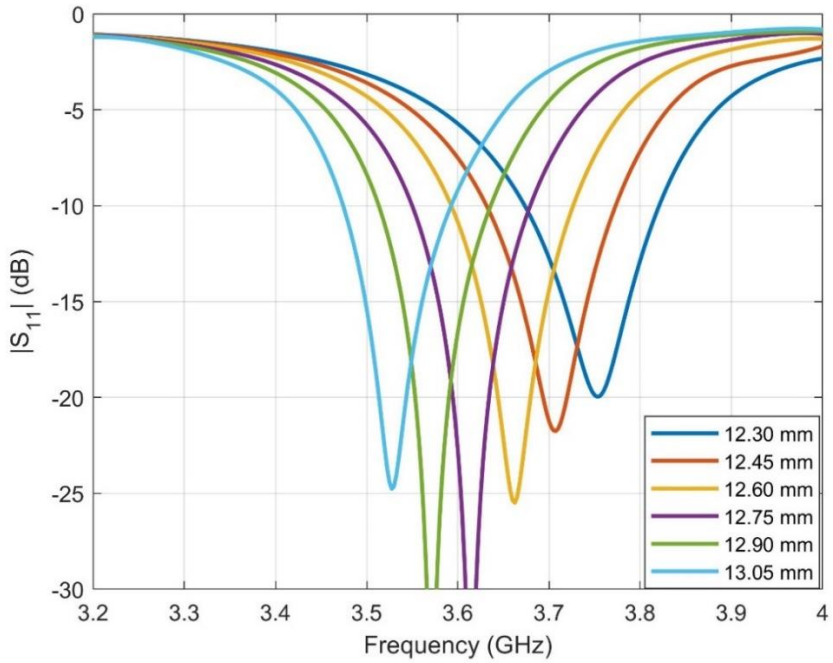

Figure 4.6: $|S_{11}|$, Circular Patch Radius Sweep

12.90 mm is a good candidate for 3.6 GHz but it is not sufficient to center 3.6 GHz so aperture width and length of feed line stub are needed to be optimized since enlarging circular patch and ring dislocates the position of aperture with respect to the antenna element. According to Figure 4.7, aperture width and length of feed line stub can be updated as 12 mm and 1 mm, respectively to have good matching.

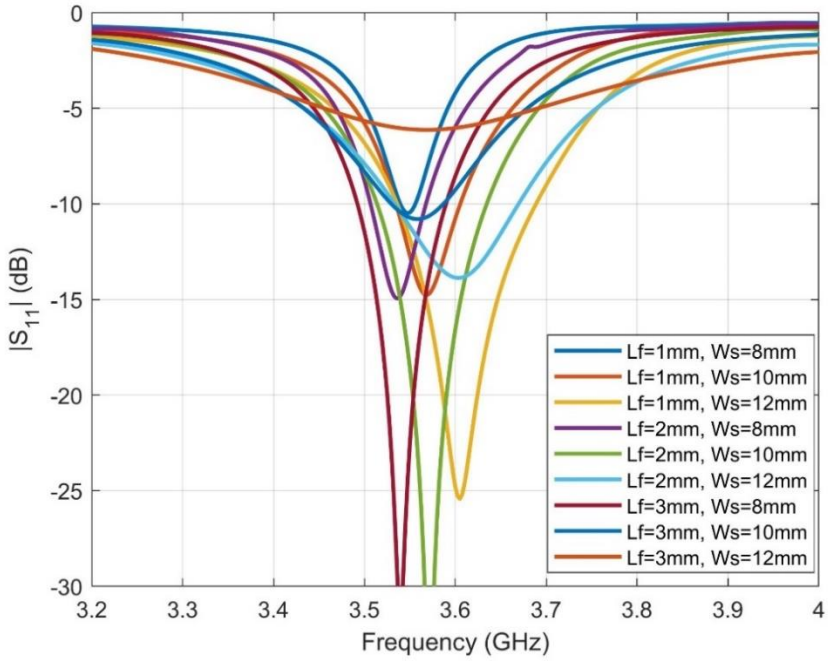

Figure 4.7: $|S_{11}|$, Sweeps of Aperture Width (Ws) and Length of Feed Line Stub (Lf)

Thus, aperture coupled RCPA is redesigned with the final parameters given in Table 4.1. In this table, circular patch is updated as 12.90 mm and because of that inner radius and outer radius of ring are updated to 13.40 mm and 20.17 mm, respectively to keep the separation between ring and circular patch, and outer to inner ratio constant. Aperture center location and aperture length are retained as in Table 2.2. Before fabrication, RCPA of Table 4.1 is simulated in HFSS and Figure 4.8 shows its S parameters. As can be seen, the antenna resonates at 3.6 GHz.

Also, active S parameters are given in Figure 4.9 with two phase differences. Poor active $|S_{11}|$ is still valid with around -4 dB for 0° phase difference and around -2 dB for 180° phase difference.

Table 4.1: Redesigned (Second Version) RCPA Antenna Parameters

Parameter	Dimension
Circular patch radius	12.90 mm
Ring inner radius	13.40 mm
Ring outer radius	20.17 mm
Aperture center location, from the origin	14.0 mm
Aperture width	12 mm
Aperture length	11 mm
Length of feed line stub, from aperture center	1 mm
Antenna substrate size	70 mm x 83.5 mm
Antenna substrate thickness	1.524 mm
Feed substrate size	87 mm x 83.5 mm
Feed substrate thickness	0.508 mm
Feed microstrip line width	1 mm

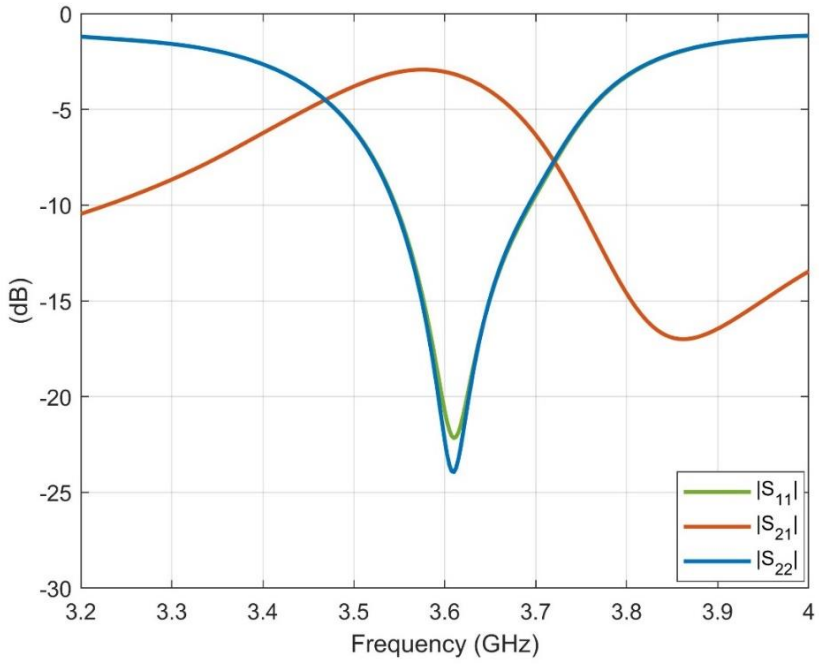

Figure 4.8: Simulated S Parameters of Second Version RCPA

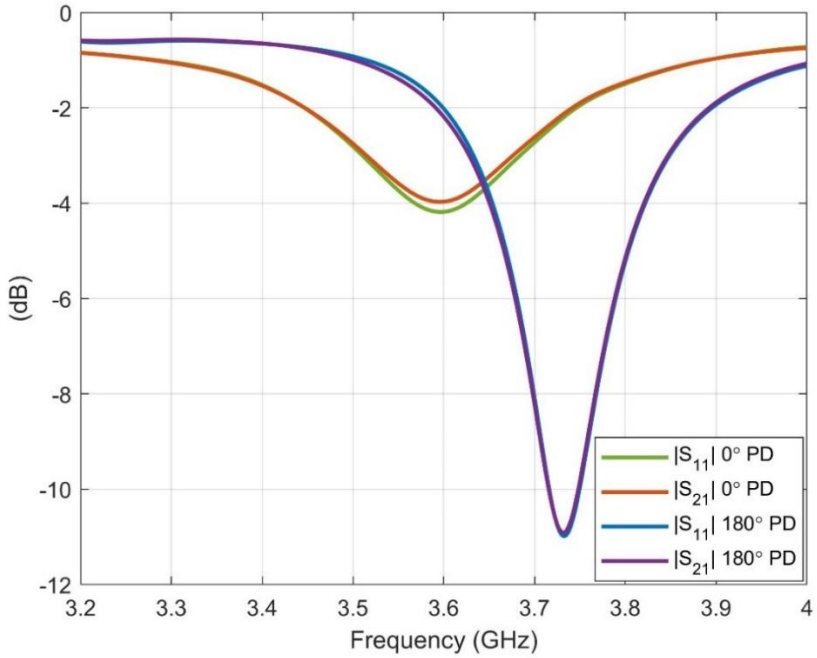

Figure 4.9: Simulated Active S Parameters of Second Version RCPA

4.2.2 Measurement Results

S parameters of the second version RCPA are measured by Network Analyzer (HP Agilent Keysight 8720D) and they are compared with simulation results in Figure 4.10. Simulation and measurement S parameters agree well with each other as seen. $|S_{21}|$ is around -4.6 dB at the resonant frequency.

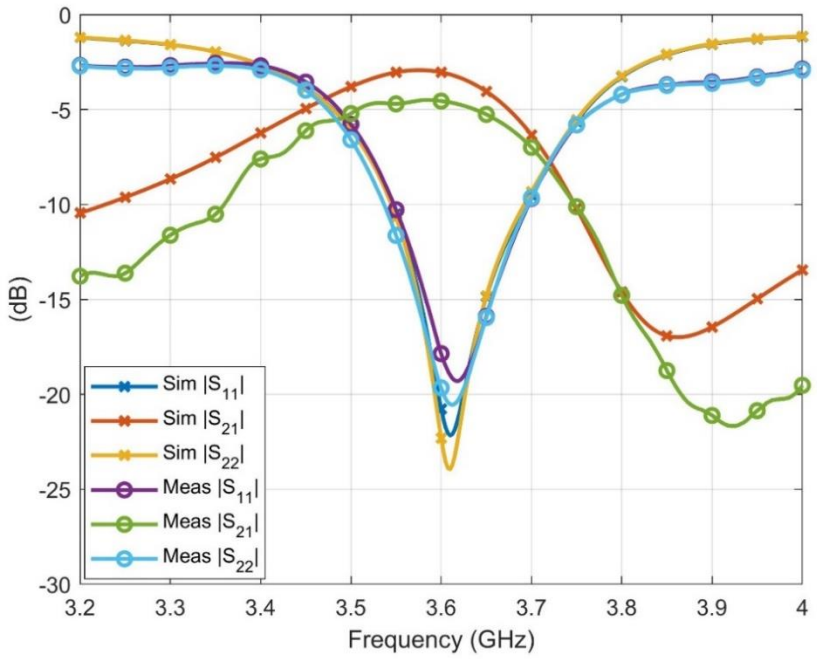

Figure 4.10: S Parameters of RCPA, Simulation Measurement Comparison

For the radiation pattern measurements, RCPA without decoupling network is mounted on the setup in anechoic chamber located in Ayaslı Research Center at Middle East Technical University. Anechoic chamber setup with RCPA is illustrated in Figure 4.11. Also, to give different phase differences to the ports of the antenna, a power divider (NARDA 4456-2) with two coaxial cables is utilized as shown in Figure 4.12. Phase differences are adjusted by considering the phase differences between the cables with respect to each other. Therefore, two different cable sets (with 0° and 180° phase differences) are exploited for the measurements.

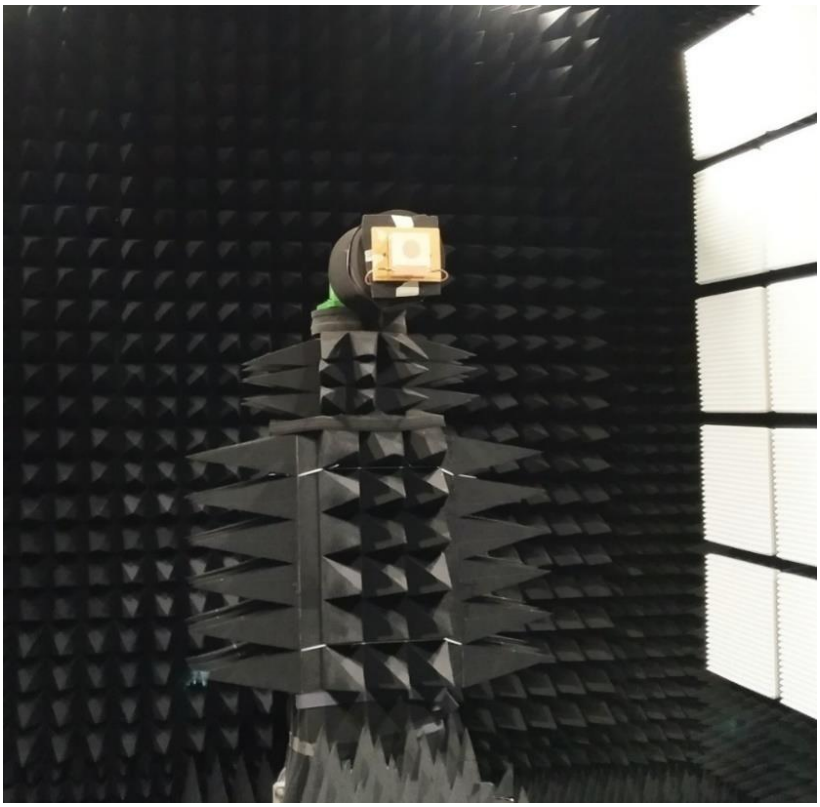

Figure 4.11: Anechoic Chamber Setup with RCPA

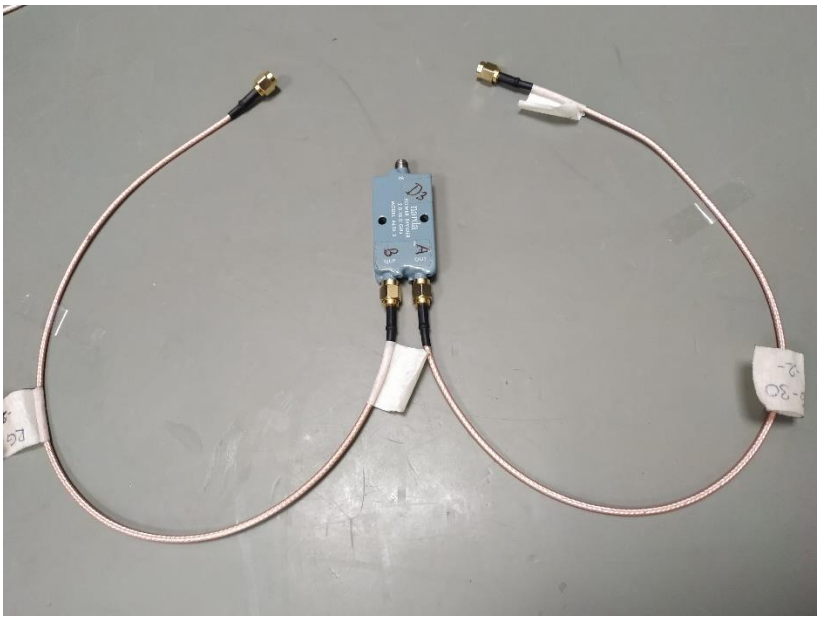

Figure 4.12: Power Divider and Coaxial Cables

In following four figures, from Figure 4.13 to 4.16, measured and simulated normalized patterns are compared. Radiation patterns for two phase differences (0° and 180°) in two planes ($\phi = 0°$ and $\phi = 90°$) are shown. All four of the measurements are in agreement with simulated results. The main distinction between measurement and simulation is levels of back lobes. Measured back lobe levels are lower than the simulated ones because absorbers covering metal flange of the setup may lead to reduction in back lobe levels in measured patterns. In addition, the patterns are not symmetrical in $\phi = 0°$ plane since the symmetry of RCPA with respect to y axis is distorted by the edge mount SMA connectors as can be seen in Figure 4.2.

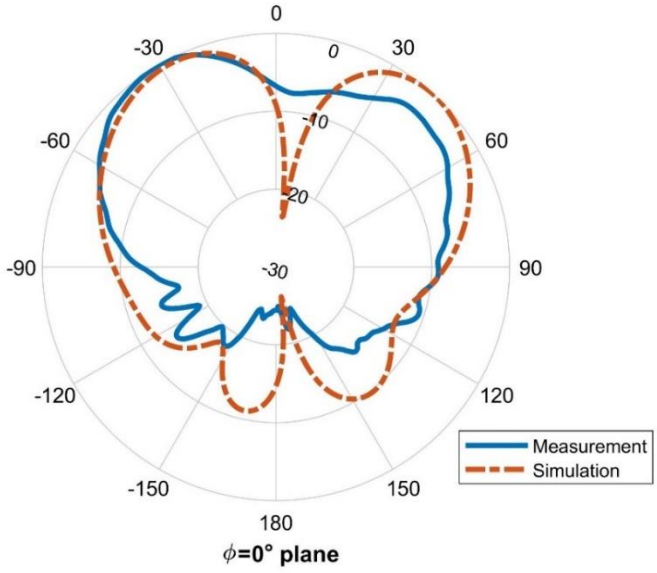

Figure 4.13: Measured and Simulated Normalized Radiation Patterns of RCPA without DN, PD:0° at $\phi = 0°$ Plane

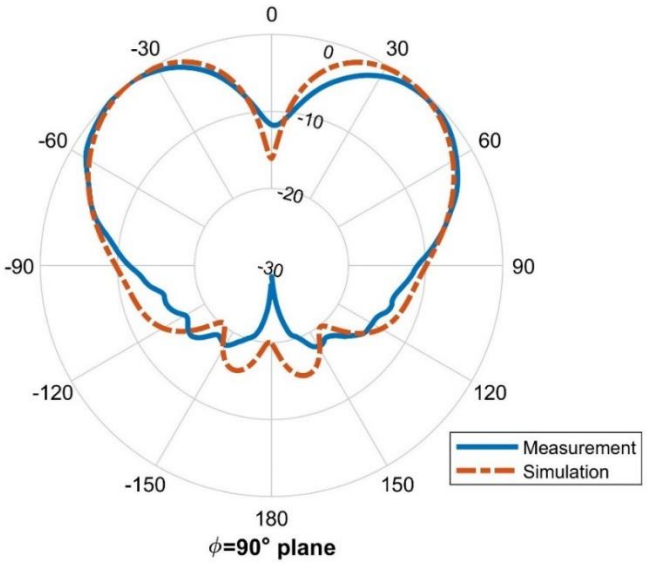

Figure 4.14: Measured and Simulated Normalized Radiation Patterns of RCPA without DN, PD:0° at $\phi = 90°$ Plane

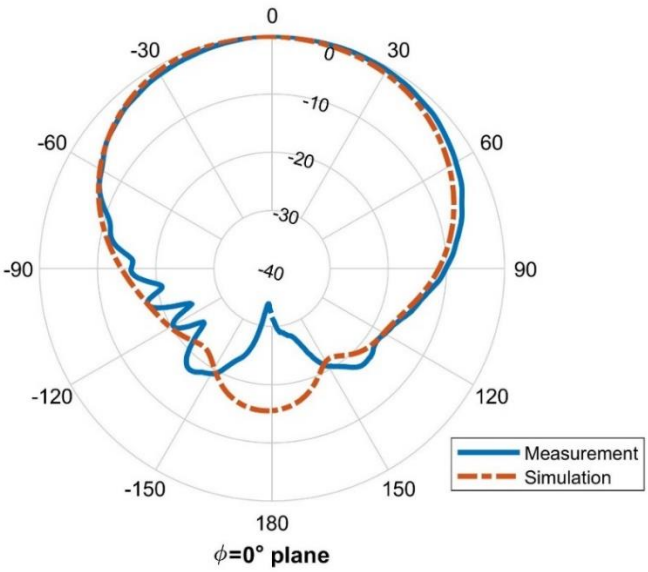

Figure 4.15: Measured and Simulated Normalized Radiation Patterns of RCPA without DN, PD:180° at $\phi = 0°$ Plane

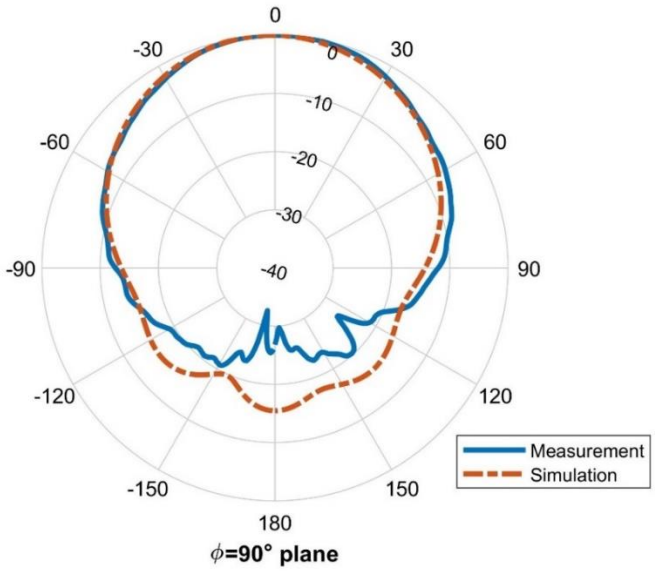

Figure 4.16: Measured and Simulated Normalized Radiation Patterns of RCPA without DN, PD:180° at $\phi = 90°$ Plane

Table 4.2: Simulated Realized Gain and Measured Gain of RCPA without Decoupling Network

Parameter	**Conical Beam (PD: 0°)**	**Broadside Beam (PD: 180°)**
Simulated Gain (dB)	6.6	6.4
Simulated Realized Gain (dB)	4.4	2.2
Measured Gain (dB)	3.0	2.6

In order to obtain exact values of measured gains, insertion losses of the power divider (0.2 dB) and the coaxial cables (0.9 dB for cable set with 0° phase difference and 1.8 dB for cable set with 180° phase difference) are added to the measured values. As seen in Table 4.2, measured gain values are close to simulated ones. The difference may arise from inadequate modeling of fabricated RCPA in simulations since as stated earlier in this chapter, designed RCPA could not be fabricated as it is

and it is remodeled in HFSS assuming 0.08 mm air gap exists between the boards. Moreover, the use of absorbers to cover the flange during the measurements may be a factor for lower measured gain.

4.3 Implementation of Inductive Decoupling Network to RCPA

Designed decoupling network is implemented to second version of fabricated RCPA as shown in Figure 4.17. Due to change in the design of RCPA, location of the inductor away from the ports and location of the stubs away from the inductor are optimized as 50 mm and 22 mm, respectively. S parameters are measured and compared with simulated parameters in Figure 4.18. Measurement results are in accordance with the simulation when stub length and stub locations in simulation are updated to 8.0 mm and 22.4 mm, respectively. These differences can be considered as normal due to handmade production. Measured $|S_{11}|$ and $|S_{22}|$ slightly differ because of imperfect alignment of the stubs. $|S_{21}|$ is decreased to -20 dB at the resonant frequency with the addition of inductive decoupling network.

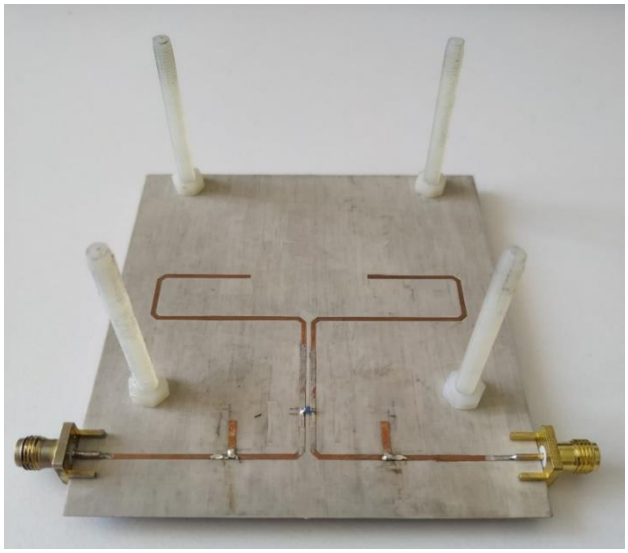

Figure 4.17: Fabricated RCPA with Inductive Decoupling Network

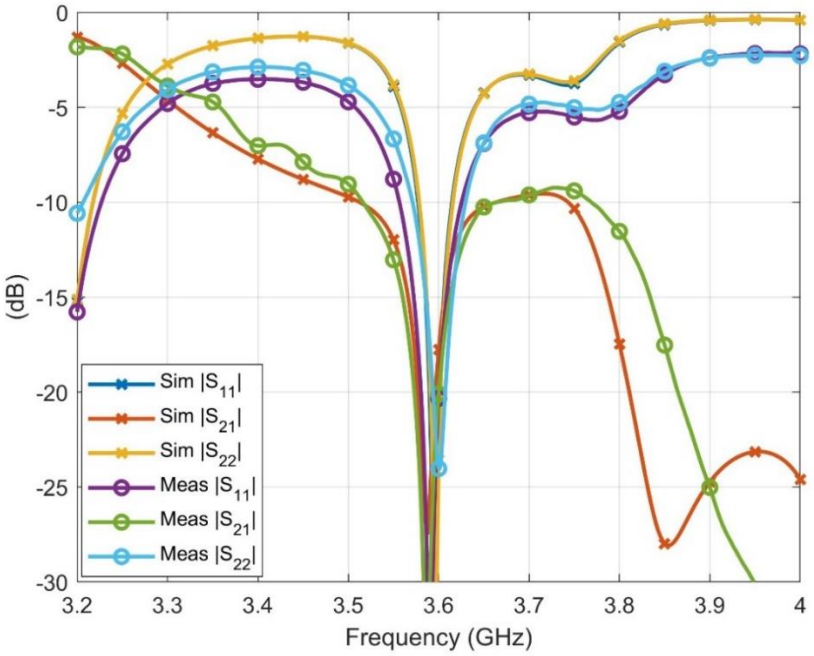

Figure 4.18: S Parameters of RCPA with Inductive Decoupling Network, Simulation Measurement Comparison

Decoupling and matching bandwidths are tabulated in Table 4.3. As seen, wider matching bandwidth is achieved in measurement results. Overall bandwidth is still narrow considering resonance frequency at 3.6 GHz. Overall bandwidth is around 1.67 % although decoupling bandwidth is around 4.17 %.

Table 4.3: Bandwidths of RCPA with Inductor

Bandwidth	**Measurement**	**Simulation (HFSS)**
10 dB Decoupling (MHz)	150	150
10 dB Matching (MHz)	60	40
10 dB Overall (MHz)	60	40

Radiation pattern measurements of RCPA with inductor are carried in the setup of Figure 4.11. In Figure 4.19 to 4.22, measured radiation patterns are compared with simulated patterns. In simulations, RCPA with inductor is remodeled with the assumption of air gap between the substrates as realistic as possible. Therefore, HFSS model may differ from the fabricated antenna. In the figures, back lobe differences arise from the absorbers used in anechoic chamber setup which reduce the back lobes more than expected. Also, the null at $\theta = 0°$ is not observed in the measurement results in Figure 4.19 which may be caused by the unbalance between two ports of the antenna. Since the stubs are constructed by hand, their lengths and locations may not be exactly same that may result in the unbalance between the ports. It can be interpreted as radiation patterns are not affected by the implementation of inductive decoupling network, which is a desired outcome. Decoupling network successfully improves the isolation between the ports while preserving far field characteristics.

The enhancement in measured gain values can be observed in Table 4.4. Gain of RCPA is increased 2.7 dB in conical beam and 2.6 dB in broadside beam with inductive decoupling network. Also, improper soldering losses and the effect of absorbers in the measurement may be the reasons for the difference between the measured and the simulated values. Thus, aperture coupled RCPA with inductive decoupling network is successfully designed and verified.

Table 4.4: Gain Values of RCPA with&without Inductive Decoupling Network

Parameter	**Conical Beam (PD: 0°)**	**Broadside Beam (PD: 180°)**
Simulated Gain with Inductive DN (dB)	6.6	6.6
Simulated Realized Gain with Inductive DN (dB)	6.2	6.0
Measured Gain with Inductive DN (dB)	5.7	5.2
Measured Gain without DN (dB)	3.0	2.6

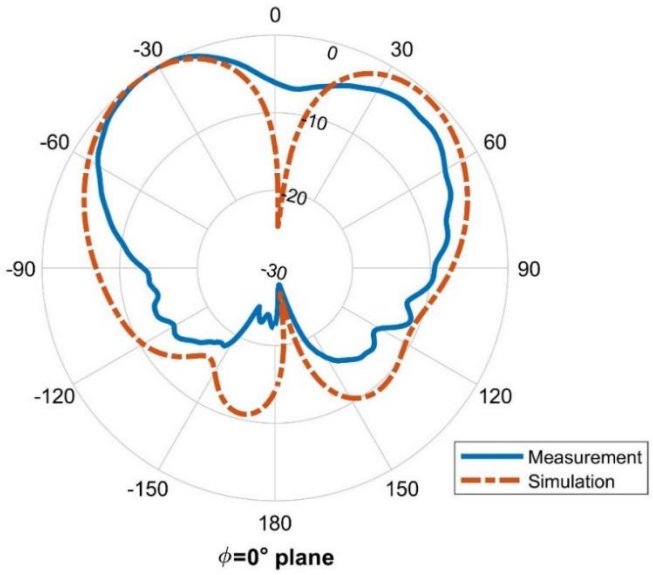

Figure 4.19: Measured and Simulated Normalized Radiation Patterns of RCPA with Inductor, PD:0° at $\phi = 0°$ Plane

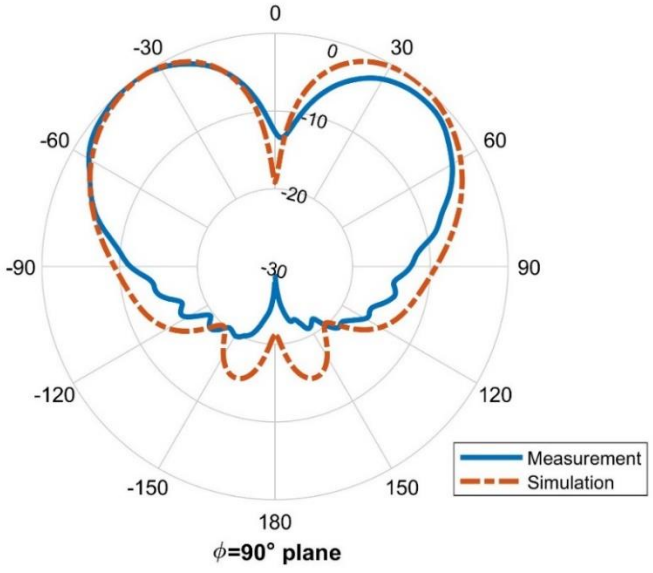

Figure 4.20: Measured and Simulated Normalized Radiation Patterns of RCPA with Inductor, PD:0° at $\phi = 90°$ Plane

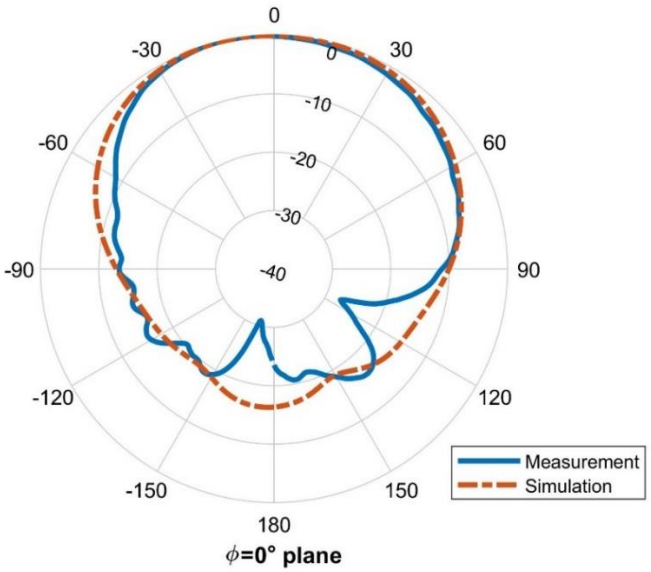

Figure 4.21: Measured and Simulated Normalized Radiation Patterns of RCPA with Inductor, PD:180° at $\phi = 0°$ Plane

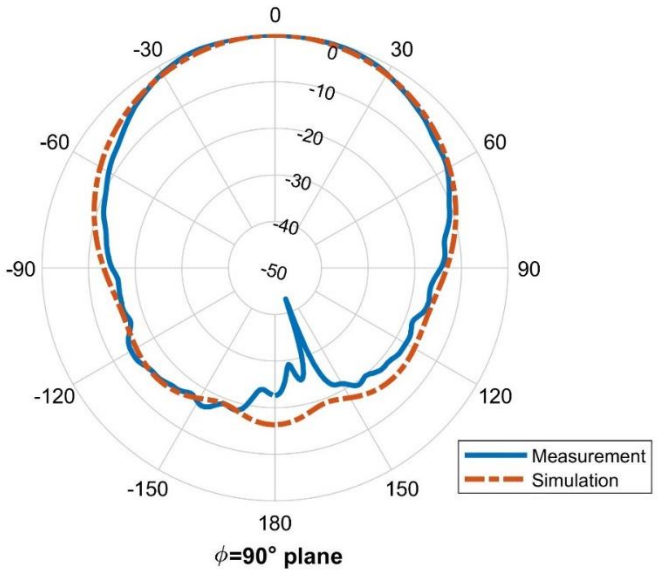

Figure 4.22: Measured and Simulated Normalized Radiation Patterns of RCPA with Inductor, PD:180° at $\phi = 90°$ Plane

4.4 Implementation of Capacitive Decoupling Network to RCPA

As in inductive case, capacitive decoupling network is implemented to second version of fabricated RCPA as illustrated in Figure 4.23. To conform with second version RCPA, value of capacitance is updated to 0.7 pF. Accordingly, location of the capacitor away from the ports and location of the stubs away from the capacitor are optimized as 64 mm and 27 mm, respectively and stub length is determined as 18 mm, experimentally. In simulation, stub length and stub locations are updated to 17 mm and 28.3 mm, respectively. These differences may arise from imperfect handmade production. S parameters of measurement and simulation are given in Figure 4.24. $|S_{21}|$ is lower than -20 dB at the resonant frequency with the addition of capacitive decoupling network.

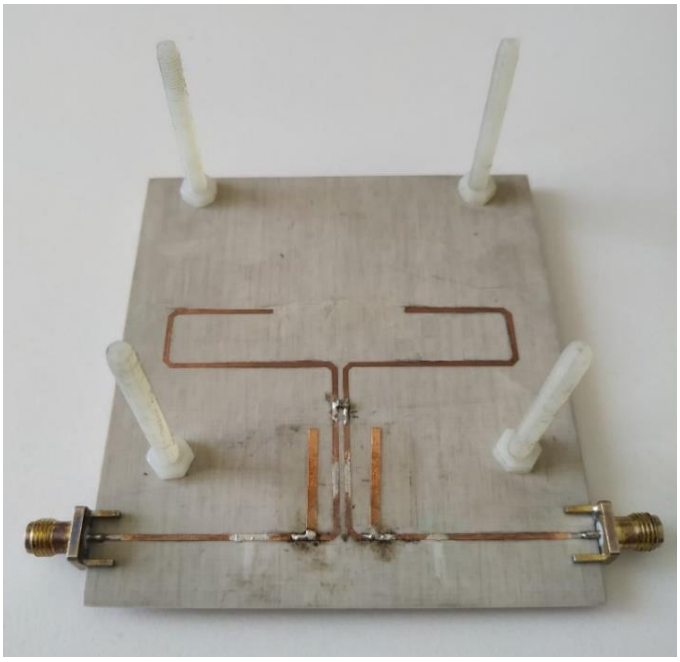

Figure 4.23: Fabricated RCPA with Capacitive Decoupling Network

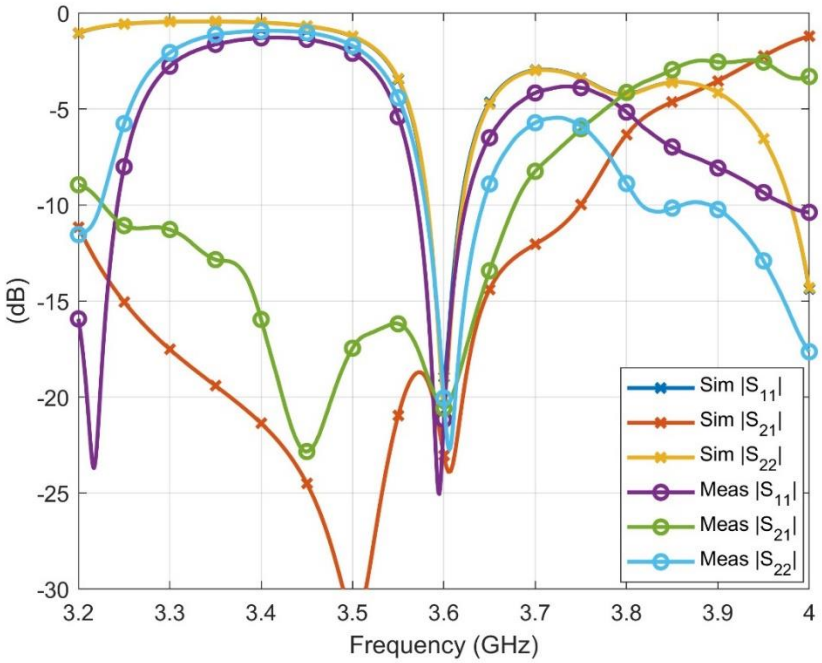

Figure 4.24: S Parameters of RCPA with Capacitive Decoupling Network, Simulation Measurement Comparison

Decoupling and matching bandwidths are given in Table 4.5. Decoupling bandwidth is wider as compared to inductive case due to flatter Im{Y_{21}} characteristics as explained in Section 3.4. However, matching bandwidth limits the overall bandwidth and it is around 1.25 % even though decoupling bandwidth is around 12.5 %.

Table 4.5: Bandwidths of RCPA with Capacitor

Bandwidth	**Measurement**	**Simulation (HFSS)**
10 dB Decoupling (MHz)	450	>550
10 dB Matching (MHz)	45	40
10 dB Overall (MHz)	45	40

Measured radiation patterns of RCPA with capacitor are given in Figure 4.25 to 4.28 along with simulated patterns. Similar pattern characteristics are observed with inductive one. Comparative gain values are presented in Table 4.6. It is shown that gain of RCPA is improved 2.3 dB in conical beam and 3.0 dB in broadside beam with capacitive decoupling network. Gain values for inductive decoupling network are repeated in Table 4.6 for easier comparison. The bandwidth and gain results are close to each other so any one of the reactive elements can be chosen for decoupling. Hence, RCPA with capacitive decoupling network is well designed and verified as well as RCPA with inductive decoupling network.

Table 4.6: Gain Values of RCPA with&without Capacitive Decoupling Network

Parameter	**Conical Beam (PD: 0°)**	**Broadside Beam (PD: 180°)**
Simulated Gain with Capacitive DN (dB)	6.7	6.8
Simulated Realized Gain with Capacitive DN (dB)	6.6	6.4
Measured Gain with Capacitive DN (dB)	5.3	5.6
Measured Gain with Inductive DN (dB)	5.7	5.2
Measured Gain without DN (dB)	3.0	2.6

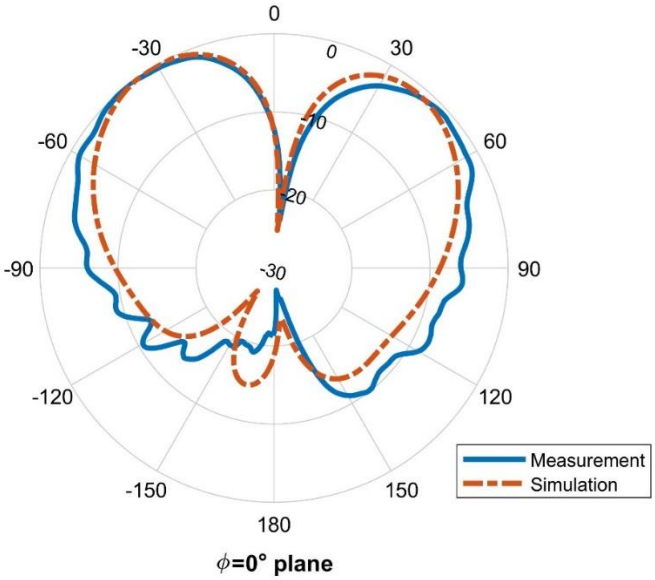

Figure 4.25: Measured and Simulated Normalized Radiation Patterns of RCPA with Capacitor, PD:0° at $\phi = 0°$ Plane

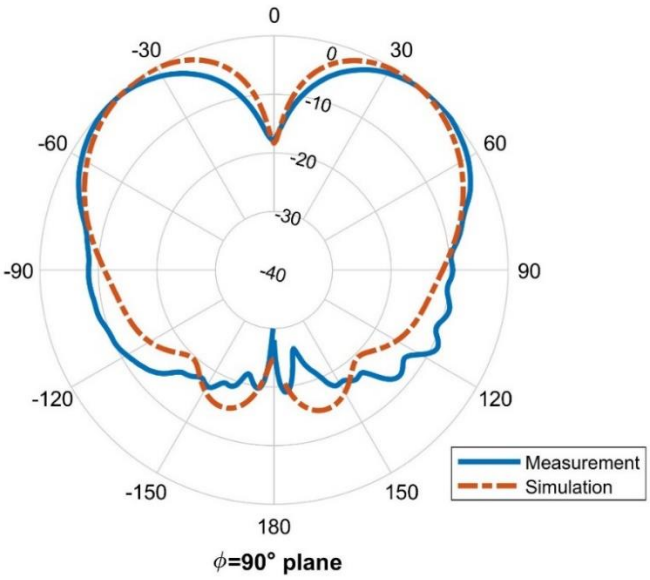

Figure 4.26: Measured and Simulated Normalized Radiation Patterns of RCPA with Capacitor, PD:0° at $\phi = 90°$ Plane

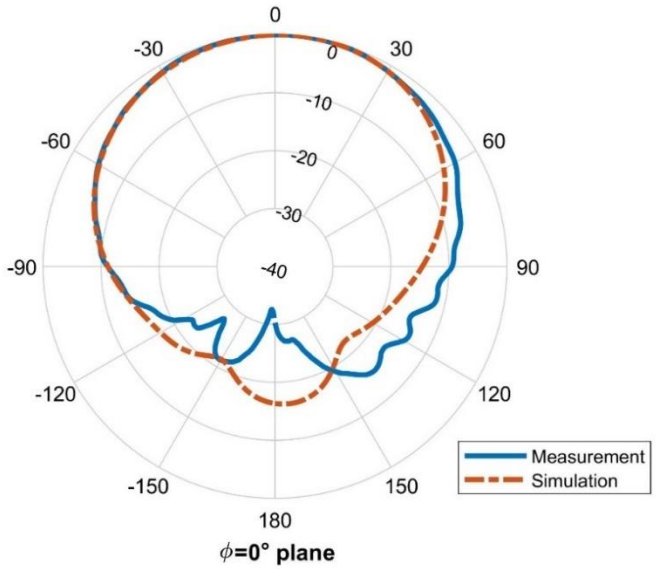

Figure 4.27: Measured and Simulated Normalized Radiation Patterns of RCPA with Capacitor, PD:180° at $\phi = 0°$ Plane

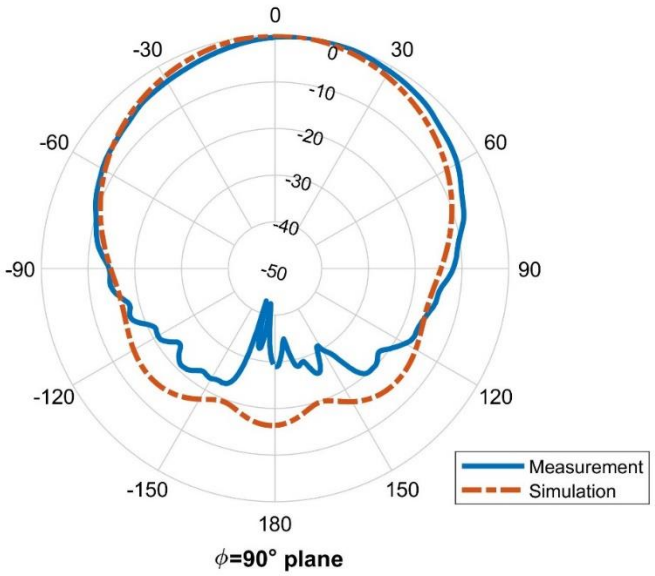

Figure 4.28: Measured and Simulated Normalized Radiation Patterns of RCPA with Capacitor, PD:180° at $\phi = 90°$ Plane

CHAPTER 5

CONCLUSION

In this thesis, isolation between the ports of a multi-functional antenna is enhanced by introducing a decoupling network. As the isolation increases, realized gain of the antenna also increases.

First of all, ringed circular patch antenna is presented with its beam steering and pattern reconfigurability features. Radiating modes of RCPA is examined by explaining radiating elements of the antenna: the circular patch and the ring. By changing the phase difference between the antenna ports, different beam directions and patterns can be obtained. And yet, RCPA suffers from coupling between the ports. The coupling causes relatively low and negative gain value which is not desired. Hence, the aim of the thesis is defined as to increase isolation between the ports so that we can achieve a better gain value. Decoupling network technique available in literature is applied to improve isolation between the ports of RCPA. Required decoupling network parameters are derived from the admittance matrix of RCPA. Inductive and capacitive decoupling networks are inserted to RCPA along with the matching stubs. Antenna with decoupling network is designed, fabricated and measured. It is shown by measurements that $|S_{21}|$ of RCPA reduces to -20 dB with an inductor and lower than -20 dB with a capacitor. The inductive decoupling network raises measured gain values of RCPA 2.7 dB and 2.6 dB in conical and broadside beams, respectively. Similary, gain values of RCPA are increased by 2.3 dB and 3.0 dB by capacitive decoupling network. In inductive case, even though decoupling bandwidth is 150 MHz, overall bandwidth is 60 MHz because of 60 MHz matching bandwidth. In capacitive case, larger decoupling bandwidth, 450 MHz, is limited by 45 MHz matching bandwidth. In both cases, overall bandwidth is

dominated by the matching bandwidth since the input parameters of the antenna ports are not suitable for wideband matching. Thus, with proper decoupling network addition, RCPA gain values approach to a value of conventional patch antenna gain as given in Chapter 4.

To sum up, the decoupling network technique is capable to increase the isolation between the ports of multi-functional antenna, RCPA and its realized gain as well.

As a future work, based on this thesis, two main approaches can be followed and studied. One is applying different isolation techniques which are mentioned in Section 1.2. In particular, decoupling line, decoupling network with LTCC element and decoupling network with coupled resonator techniques can be a good candidate for the isolation of RCPA ports. Other approach is implementing the decoupling network to a different antenna with similar features, especially having two feed lines. If that antenna has convenient input parameters for wideband matching with flat imaginary part of antenna Y_{21}, then larger overall bandwidth can be achieved as compared to this study. It is worth noting that RCPA with decoupling network is sensitive to manufacturing process since it is narrow band. Therefore, better results can be obtained if the antenna is fabricated more professionally.

REFERENCES

[1] C. A. Balanis, *Antenna theory: Analysis and Design*. 3rd ed. New Jersey: Wiley-Interscience, 2005.

[2] F. T. Çelik, “Pattern Reconfigurable Antenna Designs in Sub-6 GHz Band for 5G Applications,” M.S. - Master of Science, Middle East Technical University, 2021.

[3] L. Liu, S. W. Cheung and T. I. Yuk, "Compact MIMO Antenna for Portable Devices in UWB Applications," in IEEE Transactions on Antennas and Propagation, vol. 61, no. 8, pp. 4257-4264, Aug. 2013.

[4] J. Ghosh, S. Ghosal, D. Mitra, and S. R. B. Chaudhuri, "Mutual Coupling Reduction Between Closely Placed Microstrip Patch Antenna Using Meander Line Resonator," Progress In Electromagnetics Research Letters, Vol. 59, 115-122, 2016.

[5] M. M. Bait-Suwailam, O. F. Siddiqui and O. M. Ramahi, "Mutual Coupling Reduction Between Microstrip Patch Antennas Using Slotted-Complementary Split-Ring Resonators," in IEEE Antennas and Wireless Propagation Letters, vol. 9, pp. 876-878, 2010.

[6] Y. Zhou, X. He, D. Shen and H. Yuan, "Metasurface for high isolation in MIMO antenna," 2018 IEEE MTT-S International Wireless Symposium (IWS), 2018, pp. 1-4.

[7] Z. Wang, C. Li, Q. Wu and Y. Yin, "A Metasurface-Based Low-Profile Array Decoupling Technology to Enhance Isolation in MIMO Antenna Systems," in IEEE Access, vol. 8, pp. 125565-125575, 2020.

[8] M. A. Moharram and A. A. Kishk, "General Decoupling Network Design Between Two Coupled Antennas for MIMO Applications," Progress In Electromagnetics Research Letters, Vol. 37, 133-142, 2013.

[9] S. Chen, Y. Wang and S. Chung, "A Decoupling Technique for Increasing the Port Isolation Between Two Strongly Coupled Antennas," in IEEE Transactions on Antennas and Propagation, vol. 56, no. 12, pp. 3650-3658, Dec. 2008.

[10] K. Qian, L. Zhao and K. -L. Wu, "An LTCC Coupled Resonator Decoupling Network for Two Antennas," in IEEE Transactions on Microwave Theory and Techniques, vol. 63, no. 10, pp. 3199-3207, Oct. 2015.

[11] K. Qian, G. Huang, J. Liang, B. Qian and T. Yuan, "An LTCC Interference Cancellation Device for Closely Spaced Antennas Decoupling," in IEEE Access, vol. 6, pp. 68255-68262, 2018.

[12] L. Zhao, L. K. Yeung and K. Wu, "A Coupled Resonator Decoupling Network for Two-Element Compact Antenna Arrays in Mobile Terminals," in IEEE Transactions on Antennas and Propagation, vol. 62, no. 5, pp. 2767-2776, May 2014.

[13] L. Zhao, L. K. Yeung and K. Wu, "A novel second-order decoupling network for two-element compact antenna arrays," 2012 Asia Pacific Microwave Conference Proceedings, 2012, pp. 1172-1174.

[14] D. M. Pozar, "A Review of Aperture Coupled Microstrip Antennas: History, Operation, Development, and Application", 1996. Available Online: https://www.ecs.umass.edu/ece/pozar/PozarPublications.pdf. [Accessed: Jun. 05, 2022].

[15] S. D. Targonski, D. M. Pozar and R. B. Waterhouse, "Aperture-coupled microstrip antennas using reflector elements for wireless communications," In Proc. IEEE-APS Conference on Antennas and Propagation for Wireless Communications, 1998, pp. 163-166.

[16] D. M. Pozar, *Microwave Engineering*. 4th ed. New Jersey: Wiley-Interscience, 2012.

APPENDICES

A. S Parameters in Terms of Y Parameters

Conversion from Y parameters to S parameters [16]:

$$S_{11} = \frac{(Y_0 - Y_{11})(Y_0 + Y_{22}) + Y_{12}Y_{21}}{\Delta Y} \quad (A.1)$$

$$S_{12} = \frac{-2Y_{12}Y_0}{\Delta Y} \quad (A.2)$$

$$S_{21} = \frac{-2Y_{21}Y_0}{\Delta Y} \quad (A.3)$$

$$S_{22} = \frac{(Y_0 + Y_{11})(Y_0 - Y_{22}) + Y_{12}Y_{21}}{\Delta Y} \quad (A.4)$$

where $\Delta Y = (Y_{11} + Y_0)(Y_{22} + Y_0) - Y_{12}Y_{21}$ and Y_0 is characteristic admittance

B. Derivation of Admittance Matrix of Two-Port Network with Purely Imaginary Component

Consider a two-port network which consists of a purely imaginary element shown in Figure B,

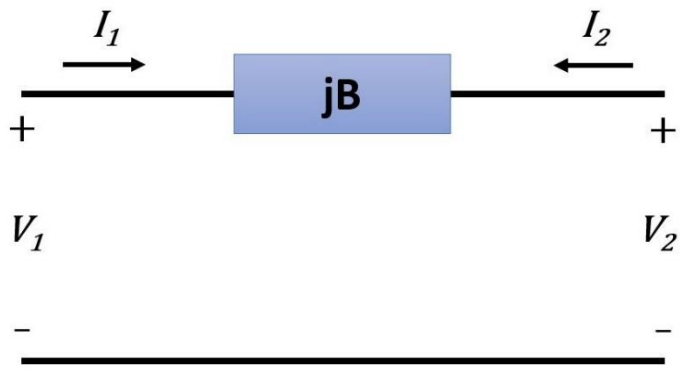

Figure B: Two-Port Network Representation of a Purely Imaginary Element

$$\begin{bmatrix} I_1 \\ I_2 \end{bmatrix} = \begin{bmatrix} Y_{11} & Y_{12} \\ Y_{21} & Y_{22} \end{bmatrix} \begin{bmatrix} V_1 \\ V_2 \end{bmatrix} \tag{B.1}$$

For Y_{11}, second port is shorted, $V_2 = 0$ so $I_1 = V_1(jB)$,

$$Y_{11} = \frac{I_1}{V_1}\Big|_{V_2=0} = \frac{V_1(jB)}{V_1} = jB \tag{B.2}$$

For Y_{12}, first port is shorted, $V_1 = 0$ so $I_1 = -I_2 = -V_2(jB)$,

$$Y_{12} = \frac{I_1}{V_2}\Big|_{V_1=0} = \frac{-V_2(jB)}{V_2} = -jB \tag{B.3}$$

For Y_{21}, second port is shorted, $V_2 = 0$ so $I_2 = -I_1 = -V_1(jB)$,

$$Y_{21} = \frac{I_2}{V_1}\Big|_{V_2=0} = \frac{-V_1(jB)}{V_1} = -jB \tag{B.4}$$

For Y_{22}, first port is shorted, $V_1 = 0$ so $I_2 = V_2(jB)$,

$$Y_{22} = \frac{I_2}{V_2}\Big|_{V_1=0} = \frac{V_2(jB)}{V_2} = jB \tag{B.5}$$

Hence,

$$\begin{bmatrix} Y_{11} & Y_{12} \\ Y_{21} & Y_{22} \end{bmatrix} = \begin{bmatrix} jB & -jB \\ -jB & jB \end{bmatrix} \tag{B.6}$$